Processing and imaging of seismic diffraction using multiparameter stacking attributes

Dissertation with the aim of achieving a doctoral degree
at the Faculty of Mathematics, Informatics and Natural Sciences
Department of Earth Sciences

submitted by
Parsa Bakhtiari Rad

2016
Hamburg, Germany

Day of oral defense: June 21, 2016
The following evaluators recommend the admission of the dissertation:
Supervisor: Professor Dr. Dirk Gajewski
Co-supervisor: PD Dr. Claudia Vanelle

to Masoud, Azar, Parissa, Pouria and Shadan

Abstract

Hydrocarbon reservoirs are usually located in geological structures that are difficult to image with the conventional seismic methods, particularly if a high resolution is desired. One common characteristic of seismic recorded wavefields are scattered waves. At abrupt discontinuities in interfaces, or small-scale structures whose radius of curvature is shorter than the wavelength of incident waves, Snell's law of reflections no longer applies. Such phenomena scatter the incident energy in all directions, leading to better illumination, which is known as diffraction. Nevertheless, standard seismic data processing methods have been tuned to enhance reflections, implying that other recorded wavefields are considered to be noise in processing. However, the importance of diffractions has been recognized in recent years since they carry useful information about the subsurface.

In this thesis, I present a new method for prestack diffraction separation and imaging using the common-reflection-surface (CRS) wavefield attributes. Diffraction separation in the full prestack data volume is of great importance in diffraction imaging since it provides enhanced resolution, especially in sparsely illuminated regions such as subsalt areas. However, prestack diffraction processing is a challenge due to the fact that diffractions in the full prestack data volume are heavily masked by reflections and noise because of their weak amplitudes. While diffractions in the zero-offset (ZO) domain are far easier to characterize and distinguish, the proposed method benefits from the the stability of zero-offset processing combined with the improved illumination of finite-offset (FO) processing to improve diffraction separation and subsequent imaging. To establish a direct connection between zero-offset and finite-offset processing, I change the kernel of an existing CRS-based extrapolation method to generate a full prestack diffraction-only data volume. The diffraction extrapolation from ZO to FO using the proposed method comprises a prestack data summation within a small surface around each finite-offset sample, leading to a significant increase in the signal-to-noise ratio of diffraction-only data.

If diffraction-only data are available, the resulting stacking velocities are dip-independent and thus do not need updates to remove the effect of the dip. Therefore, after prestack diffraction separation, time migration velocity analysis can directly use stacking velocities. Accordingly, I present a method for diffraction-based prestack time migration velocity model building. The data examples demonstrate the good potential of diffractions for time imaging using the proposed method. I also extend the proposed workflow to the 3D in order to overcome the problem of out-of-plane scatterers and discuss the challenges of 3D diffraction imaging. Finally, to further enhance diffraction imaging, I present a new diffraction weight function based on the combination of the width of the projected Fresnel zone (PFZ) with an existing weight. Several data example, including simple and complex synthetic and field data support the applicability of the proposed methods.

Zusammenfassung

Kohlenwasserstoff Reservoire befinden sich in der Regel in komplexen geologischen Strukturen, die schwierig mit konventionellen seismischen Methoden darzustellen sind, insbesondere wenn eine hohe Auflösung erforderlich ist. Eine häufige Charakteristik von aufgezeichneten seismischen Wellenfeldern sind gestreute Wellen. Sie treten an abrupten auftretenden Diskontinuitäten und kleinskaligen Strukturen deren Radius kleiner ist als die vorherrschende Wellenlänge auf. In diesen Fällen gilt nicht mehr Snellius Gesetz der Reflektion und Refraktion. Diese Phänomene streuen die einfallende Energie in alle Richtungen. Man nennt sie Diffraktionen. Dieses Ereignis ist sehr wichtig für die Entwicklung von Methoden, die in der Lage sind, mithilfe von seismischer Prozessierung, komplexe Strukturen darzustellen. Herkömmliche seismische Methoden allerdings sind darauf ausgelegt reflektierte Wellenfelder abzubilden. Das bedeutet andere aufgezeichnete Wellenfelder werden als unerwünschtes Rauschen in der Prozessierung unterdrückt.

In den letzten Jahren wird die Bedeutung von Diffraktionen immer mehr beachtet. Die Separation von Diffraktionen und ihre Abbildung is eine herausfordernde Aufgabe, da Diffraktionen meist von stärkeren Reflektionen maskiert werden und auf Grund ihres schwachen Signals als Rauschen wahrgenommen werden. In dieser Arbeit präsentiere ich eine neue Methode um Diffraktionen von Reflektionen vor der Stapelung zu separieren. Die vorgeschlagene Methode basiert auf den sogenannten common-reflection-surface (CRS) Wellenfeldattributen, die es erlauben Diffraktions- und Reflektionslaufzeiten genau zu bestimmen. Die Summation vor der Stapelung entlang einer Diffraktionslaufzeitkurve unterdrückt Rauschen, was zu einer verbesserten Diffraktionsseparation führt. Es erlaubt zudem sogenannte gather, die nur Diffraktionen enthalten, die einige spannende Anwendungsmöglichkeiten bieten, wie zum Beispiel Migrationsgeschwindigkeitsbestimmung. Die Separation vor der Stapelung wird mit Hilfe der partial CRS Stapelungsmethode umgesetzt. Es ist eine robuste Technik in der seismischen Datenbearbeitung, die es ermöglicht die Qualität der Daten zu verbessern und Spuren zu interpolieren.

In Datensätzen die nur Diffraktionen enthalten hängen die Stapelgeschwindigkeiten nicht länger von der Neigung ab. Daher können sie direkt als root-mean-square (RMS) Geschwindigkeiten angesehen werden, die für eine Zeitmigration benutzt werden können. In dieser Arbeit wende ich eine Zeitmigration mit diesen bestimmten Geschwindigkeiten auf den kompletten Datensatz und die separierten Diffraktionen an. Weiterhin erweitere ich die Methodik auf den dreidimensionalen Fall. Weiterhin diskutiere ich auftretende Probleme in 3D Medien. Am Ende führe ich ein neues Gewicht für die Diffraktionsseparation ein, das die Qualität der Separation verbessert. Es basiert auf der projizierten ersten Fresnelzone, die mit einem bereits existierendem Gewicht kombiniert wird. Dadurch werden mehr Diffraktionen erkannt. Verschiedene Datenbeispiele, einfache und komplexe synthetische

und Felddaten, verifizieren die Anwendbarkeit der vorgestellten Methoden in zwei und drei Dimensionen.

List of Figures

List of Tables

Contents

Chapter 1

Introduction

1.1 Overview of diffraction imaging

Reflection seismology is a powerful method in oil and gas exploration which uses the principles of seismology to estimate the properties of the Earth's subsurface from reflected seismic waves. The method requires a source of energy, such as dynamite or a vibrator in land data acquisition, or an airgun in marine acquisition. The seismic source sends seismic waves in all directions. They propagate in the subsurface and hit different geological features in the earth. The geological structures reflect the down-going wave to the measurement surface. Processing and imaging techniques are then applied to the recorded data in order to create an image of the subsurface. This image is used for interpretation to estimate and evaluate characteristics of the hydrocarbon reservoir.

Over decades, standard processing methods have been tuned to reflected waves. The diffracted component of the wavefield is not widely used. Nevertheless, the importance of diffractions has been recognized in recent years since the medium to small-scale structural details and heterogeneities, e.g., faults, pinch-outs, tin lenses, fracturing etc. are of crucial importance for prospecting and development of fractured reservoirs (see, e.g. Khaidukov et al., 2004; Sava et al., 2005; Fomel et al., 2007; Landa et al., 2008; Dell and Gajewski, 2011). Such structures that scatter an income wave to all directions, are a source of non-Snell scattering or seismic diffraction. Diffracted signals travel to all direction, leading to better illumination compared to reflections. Diffractions are also linked to the high-resolution imaging of elements with sub-wavelength scale or Rayleigh limit (Khaidukov et al., 2004). However, diffraction imaging is a difficult task since diffractions are usually masked by reflections and noise in the data because of their weak amplitudes.

In this thesis, a method for prestack diffraction separation based on the common-reflection-surface (CRS) stack (Müller et al., 1998; Jäger et al., 2001; Mann, 2002) is presented. The CRS is a multi-parameter stacking method that belongs to the class of macro model

independent imaging techniques. It makes use of the neighboring common midpoint (CMP) gathers during stacking to sum up the data coherently in both midpoint and offset directions. The CRS method provides not only a stacked section but also additional stacking attributes (known as kinematic wavefield attributes) that can be utilized for various applications, including the calculation of geometrical spreading (Hubral, 1983), the determination of the approximated projected Fresnel zone (Mann, 2002), depth velocity model building (Duveneck, 2004), limited aperture depth migration (Jäger, 2004), CRS-based time migration (Spinner, 2007), prestack data regularization and enhancement (Baykulov and Gajewski, 2009), multiple suppression (Dümmong, 2010) or post- and prestack diffraction imaging suggested by Dell and Gajewski (2011).

Diffraction separation can be carried out in either zero-offset (ZO) or finite-offset (FO) domain. ZO diffraction processing is fast, but less reliable since for instance, the stacking by itself is harmful to weak diffractions. Moreover, the diffractions interfered with continuous reflections, e.g., edge diffractions, are suppressed during the stacking (see, e.g. Sun, 1994; Khaidukov et al., 2004). In addition, in poststack processing of a seismic image, discontinuities in the seismic images can appear for a variety of reasons other than diffractions, e.g., errors in the velocity model that is used to obtain the image. Finite-offset processing in contrast may provide improved resolution, especially in sparsely illuminated regions such as subsalt areas (Spinner, 2007). However, due to the larger number of parameters the problem is of higher dimensionality, which makes processing less stable and computationally more expensive than in the ZO setting (Bauer et al., 2015).

In order to combine the stability of ZO CRS with the improved illumination of FO processing, I present a CRS-based extrapolation method to effectively separate diffraction from reflections. The new method is mainly based on the partial CRS stack method (Baykulov and Gajewski, 2009) combined with a ZO threshold diffraction function introduced by Dell and Gajewski (2011). In the presented workflow, the partial CRS stacking technique, which is a robust technique in seismic data processing for prestack data enhancement and trace interpolation, is modified in order to isolate diffractions in the full volume of the prestack data. By partially stacking amplitudes only along the diffraction traveltimes, random noise is heavily attenuated, signal-to-noise ratio (SNR) of the prestack data is thus increased and the diffraction-only gathers are generated accordingly.

The diffraction gathers have exciting applications in data processing. In recent years, migration velocity analysis tuned to diffraction velocities has gained interest (see, e.g. Sava et al., 2005; Fomel et al., 2007; Landa et al., 2008; Dell and Gajewski, 2011) since it provides the proper velocity attribute for time migration. Prestack diffraction separation is also advantageous in this respect. The velocity spectra determined after prestack diffraction separation show clearer and better focused picks (Bakhtiari Rad et al., 2014; Bakhtiari Rad and Gajewski, 2015). In addition, the subtraction of diffracted noise in the shallow water environments from the whole data can significantly improve velocity analysis (Necati et al., 2005).

Prestack diffraction separation can be extended to the 3D case. However, diffraction processing in 3D media is a challenge since a diffraction by itself is a 3D phenomenon. Three

dimensional diffraction processing techniques must deal with the problem of the traveltime variations along different azimuths (Moser, 2011). The fact that diffraction behavior changes in different azimuths poses another challenge to separate them (Keller, 1962; Klem-Musatov et al., 2008). To overcome this issue, all separation methods should consider all possible azimuths for calculation of a diffraction response, which is computationally expensive. The 3D prestack diffraction separation method suggested in this thesis assumes some limitations, e.g., limited azimuth search to ease the process of the determination of the 3D CRS attributes.

In 2D, the i-CRS operator (Vanelle et al., 2010; Schwarz et al., 2012) which is a double-square-root (DSR) expression is used in the workflow to sum up the data along diffraction traveltimes. However, in 3D, the classical CRS operator (Müller, 2003; Bergler, 2004) is used for stacking. The 3D DSR CRS-type stacking operator is under construction at the time of writing this thesis.

Another aspect of diffraction separation is which type of diffraction characteristics are considered in order to distinguish them in the data. Different solutions based on the kinematic or dynamic features of diffractions were suggested (see, e.g. Sava et al., 2005; Moser and Howard, 2008; Klokov and Fomel, 2012). In the context of the CRS attributes, the absolute equality of two principle curvatures allows to identify diffractions in the data. However, in reality a threshold should be chosen to control the separation progress. Dell and Gajewski (2011) suggested an exponential function to evaluate the threshold. The function takes values between 0 and 1. The value of the function is close to one in case of diffractions. The robustness of the function by Dell and Gajewski (2011) is decreased in higher times (see, e.g. Schwarz, 2015). It is vulnerable to the presence of noise as well. I therefore suggest an extended function based on the combination of the existing function by Dell and Gajewski (2011) with the width of projected first Fresnel zone (see Mann, 2002). Although in theory a Fresnel zone is not defined (respectively infinite) for point diffractors, however in practice, such diffractors are the highly-curved reflectors with radius much smaller than the dominant wavelength ($R \ll \lambda$). In consequence, the width of the projected Fresnel zone for a diffraction is much larger than for a reflection, the difference can be used as a consistent attribute to better identify diffractions in the data and enhance the separation.

1.2 Structure of this thesis

Chapter 2 gives an overview about the theory of the CRS stacking method as a framework of prestack diffraction separation. Physical interpretation of CRS attributes and the CRS implementation are reviewed afterward. Some general remarks about different aspect of the CRS which influence diffraction separation follow at the end of that chapter.

In **Chapter** 3, I review the main properties of diffractions and the role of diffractions in seismic imaging. After a brief discussion about different diffraction traveltime approximations, I develop a workflow for prestack diffraction separation and imaging.

The velocity model building uses a semblance based analysis of diffraction traveltime in diffraction gathers. Application to two complex synthetic and field data sets in order to evaluate the performance of the proposed approach is shown as well.

Afterwards in **Chapter** 4, I extend the proposed approach to three dimension. Some challenges and limitations about diffraction processing in 3D are discussed beforehand. Afterward, the application to a simple model as well as a complex data set is shown. The results are compared to the existing method of diffraction separation. Finally, I propose an automated workflow for applying prestack time migration tuned to diffraction velocities.

To further improve diffraction imaging, in **Chapter** 5, I focus on the diffraction weight function. After a brief review of the projected Fresnel zone, I present an extended diffraction weight based on the combination of the width of the projected Fresnel zone and the existing function by Dell and Gajewski (2011). To evaluate the potential of the new function, I will incorporate it in the pre- and poststack diffraction separation workflows. Application to a gradient model as well as a complex data set are shown in the chapter.

Finally in **Chapter** 6, I summarize the results of the thesis and present some outlooks.

Chapter 2

Data-driven seismic imaging

In this chapter, I briefly discuss a number of important seismic concepts mostly related to the data-driven common-reflection-surface (CRS) stacking technique that forms the framework of the proposed methods in this thesis. I start with the CRS concept, the difference between the CRS and the conventional stacking methods, the CRS traveltime and the physical meaning of the CRS wavefield attributes. Finally, the conventional CRS attribute-search strategy and some important issues regarding the CRS implementation are addressed.

2.1 Exploration seismology

Seismology is the study of seismic waves, caused by rock suddenly breaking apart within the earth or the slipping of tectonic plates on the oceanic or continental scale. We know these as events as earthquakes. They can also be caused by explosions from volcanic eruptions and testing of nuclear bombs. Seismologists study earthquakes and their results, like tsunamis, and landslides. They may also monitor active volcanoes for tremors and signs of an impending eruption. They use seismographs and computer equipment to collect and analyze data on seismic events. In general, all seismic events contain the valuable information about the Earth's interior and processes going on inside. Therefore, the object of modern seismology is to extract as much information as possible from these surface records about the nature of the seismic wave propagation and seismic parameter distribution in the Earth and the source which generated the waves to analyze different parts of the Earth's interior, e.g., the crust, mantle and core (Figure 2.1).

However, some seismologists study the earth on the local scale, e.g., the near-surface regime, by deliberately induced by controlled explosions to search for underground sources of petroleum and natural gas. This method which is known as exploration seismology is a major tool to search for hydrocarbon resources and seems to have no strong rival. It

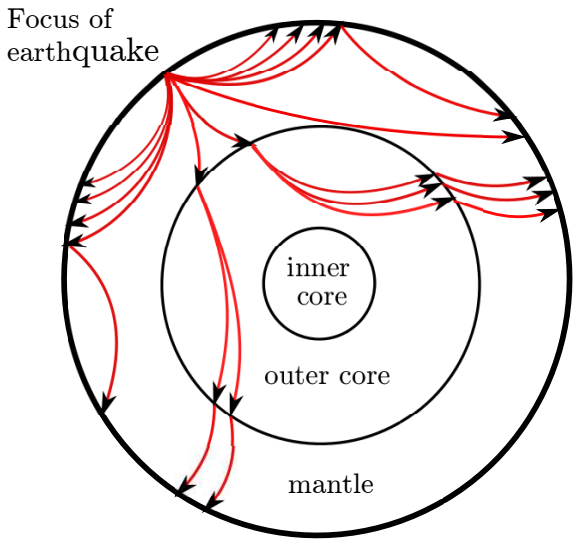

Figure 2.1: A typical global-scale (earthquake) seismology: a cross-section of the Earth showing the propagation of seismic waves (red lines) after an earthquake.

can give the best image of the subsurface and very detailed information about types of the rocks and geological setting which are of great importance for reservoir characterization. A seismic experiment consists of different stages from data acquisition to data processing and interpretation. Seismic data acquisition involves applying a seismic energy source, such as a vibroseis truck or shot-hole dynamite at a discrete surface location. The resulting energy is reflected back from interfaces where rock properties change (see Figure 2.2). After data is recorded, processing techniques including denoising, stacking and migration techniques are applied using different computer facilities to obtain a reliable subsurface image for geological interpretation.

2.2 Data redundancy

Stacking has been one of the most important seismic technique that still plays a key role in data processing. A stacked section is the first reliable image from the subsurface. Moreover, stacking allows a considerable redundancy of data and results in an improved signal-to-noise ratio. In principle, stacking means to sum up data over a line or a surface of reflection (or diffraction) impulse responses. Stacking operators represent an approximation of traveltime move-out and can be parameterized with one or several parameters. A multi-parameter stacking operator performs the summation in two directions (i.e., midpoint and offset), whereas a single-parameter stacking operator performs the summation only in one direction (i.e., offset). The well-known CMP stacking method (see, e.g. Mayne, 1962) uses a single-parameter operator which relies only on stacking velocities. In contrast, the CRS stack method employs a multi-parameter operator which uses kinematic wavefield attributes to approximate the summation surface.

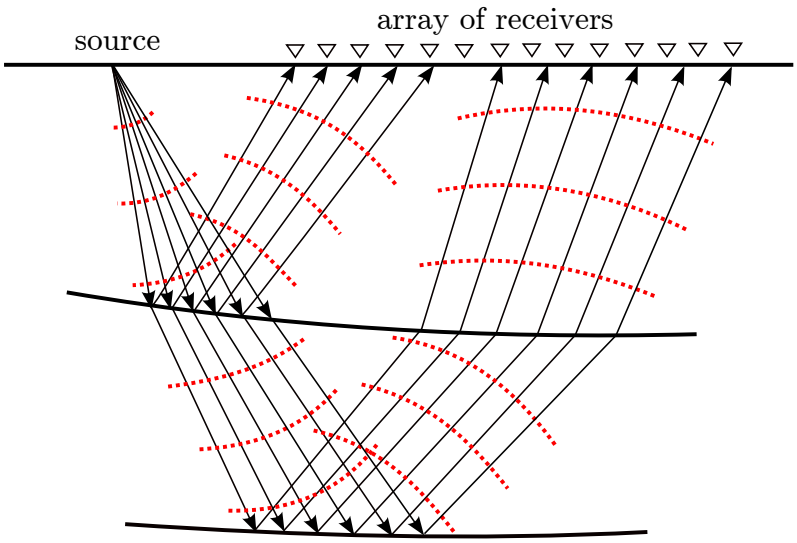

Figure 2.2: A typical local-scale seismic data acquisition: once a seismic source is excited, the seismic wavefields are generated and propagated to the subsurface. The reflected wavefields are recorded at the measurement surface by receivers. If the wavefields characteristics, e.g., rays (black) and wavefronts (red dotted) are included and modeled appropriately in processing, it leads to obtaining useful information about the subsurface.

2.3 The common-reflection-surface (CRS) stack

The CRS stacking operator (Jäger et al., 2001; Müller, 2003) considers the reflection response that stems from a reflector element in the subsurface while the CMP stacking operator only considers an individual reflection point. Therefore, the CMP operator is a special case of the CRS stacking operator. The both stacking methods yield a simulated zero-offset (ZO) section without any ray tracing or explicit velocity model. The CRS operator usually sums up the prestack data in midpoint and half-offset coordinates. Using an entire stacking surface rather than a trajectory in the time-midpoint-offset space implies that the considered reflection events are continuous over several neighboring midpoint gathers. This does not only lead to a stabilization in the determination of the stacking parameters but also overcomes the problem that a CMP gather may contain information from more than one reflection point in depth. In conventional processing, an additional dip-move-out (DMO) correction is therefore required to transform the common midpoint positions to the true common reflection points (CRP) which provide dip-corrected stacking velocities (Deregowski and Rocca, 1981). The CRS technique, however, does not require an additional DMO correction.

Figure 2.3 illustrates the CRS stacking operator and CMP stacking trajectory in the time-midpoint-offset volume for a 2D model (the gray plane). The black curves represent the

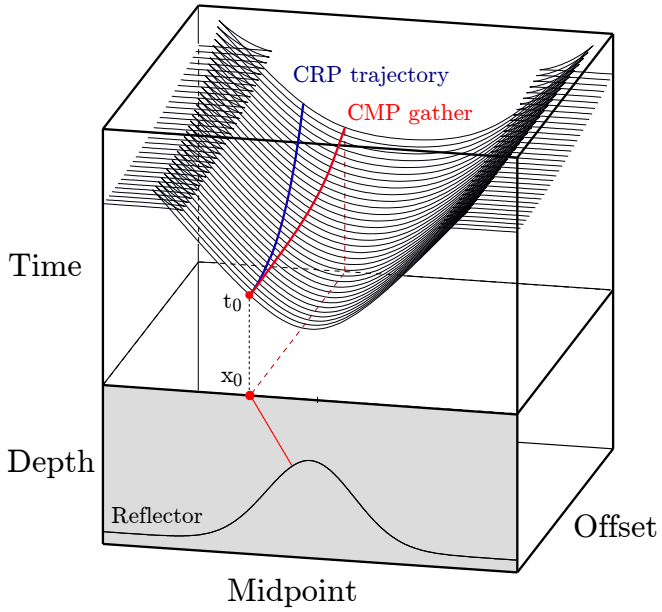

(a)

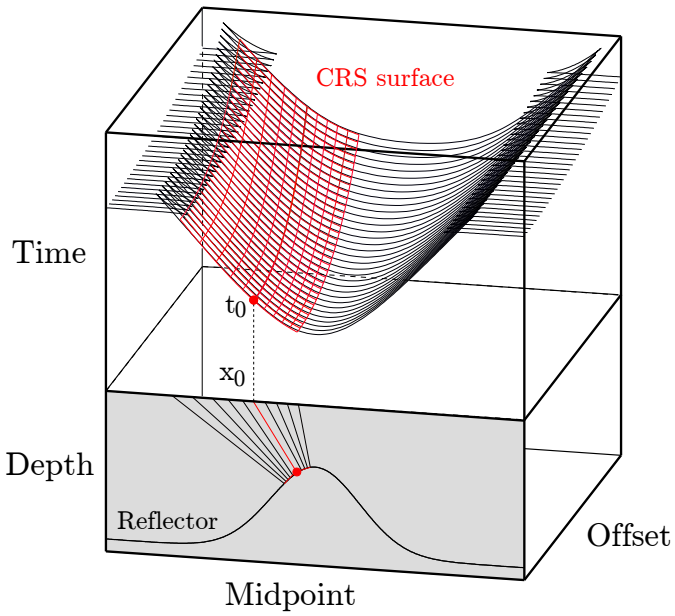

(b)

Figure 2.3: CRS stacking operator and CMP trajectory in the time-midpoint-offset volume in 2D case (modified after Müller, 2003). The black curves in both figures represent the traveltime impulse response of the reflector in depth. (a) The red line in the upper part of the pictures represents the CMP stacking path for fixed source-receiver offsets. The blue line indicates the CRP stacking trajectory for the ZO sample x_0. (b) The red surface indicates the CRS summation surface.

traveltime impulse response of the reflector in depth. The red line represents the CMP stacking path for fixed source-receiver offsets. The blue line indicates the CRP stacking trajectory for the ZO sample x_0. The red surface indicates the CRS summation surface. Summation not only takes place in offset but also in midpoint direction. Extension in midpoint direction allows to take reflector dip and curvature into account. In addition, it leads to a higher signal-to-noise ratio. Through different applications on real data sets, Mann (2002) showed that the CRS stack offers an exciting approach to construct a high quality stacked section.

2.3.1 Approximation of the CRS traveltime

The traveltime approximation which defines the stacking surface for the CRS method is derived from the paraxial ray theory (e.g. Ĉervený, 2001). In this theory, the concepts of rays and wavefront are equally important and they both provide a combined view on the propagation of wavefields. Rays and wavefronts are generally coupled to each other and in an isotropic medium and rays are always perpendicular to the wavefront. The traveltimes of propagating wavefields are then approximated using neighboring rays in the vicinity of the central ray. Parameters describing a paraxial ray are its distance to the central ray and the deviation of its slowness vector from that of the central ray. Paraxial ray theory implies that the values of the parameters at any point of a paraxial ray are linearly dependent on those at its initial point (Hubral et al., 1992). This dependency is described by different propagator matrices (suggested by, e.g. Ĉervený, 1987; Bortfeld, 1989) from which, the second-order derivative matrices of the traveltime can be obtained. Bortfeld (1989) introduced a 4×4 propagator matrix for so-called seismic systems, i.e., homogeneous isotropic media separated by smoothly curved interfaces and generalized by Hubral et al. (1992) to laterally inhomogeneous layered media with an arbitrary (transmitted or reflected) central ray together with a paraxial ray in its close vicinity. For a detailed description of the ray method, I refer to Bortfeld (1989), Hubral et al. (1992) and Ĉervený (2001).

The following derivations are based on a 3D inhomogeneous layered isotropic medium with smooth interfaces as shown in Hubral et al. (1992). The rays pass through this medium originating from an initial surface and ends in a final surface. The description of displacement and ray slowness vecotors as well as the coordinate systems on the initial (or the anterior) and the final (or posterior) surfaces are reviewed in Figure 2.4. Bortfeld (1989), Hubral et al. (1992) and Schleicher et al. (1993) demonstrated that a relationship between the central ray and an arbitrary paraxial ray can be expressed by means of the 4×4 ray propagator matrix

$$\underline{\underline{\mathbf{T}}}(G,S) = \begin{pmatrix} \underline{\mathbf{A}} & \underline{\mathbf{B}} \\ \underline{\mathbf{C}} & \underline{\mathbf{D}} \end{pmatrix}, \tag{2.1}$$

where $\underline{\mathbf{A}}$, $\underline{\mathbf{B}}$, $\underline{\mathbf{C}}$ and $\underline{\mathbf{D}}$ are 2×2 submatrices of $\underline{\underline{\mathbf{T}}}$. A linear relationship between the vector

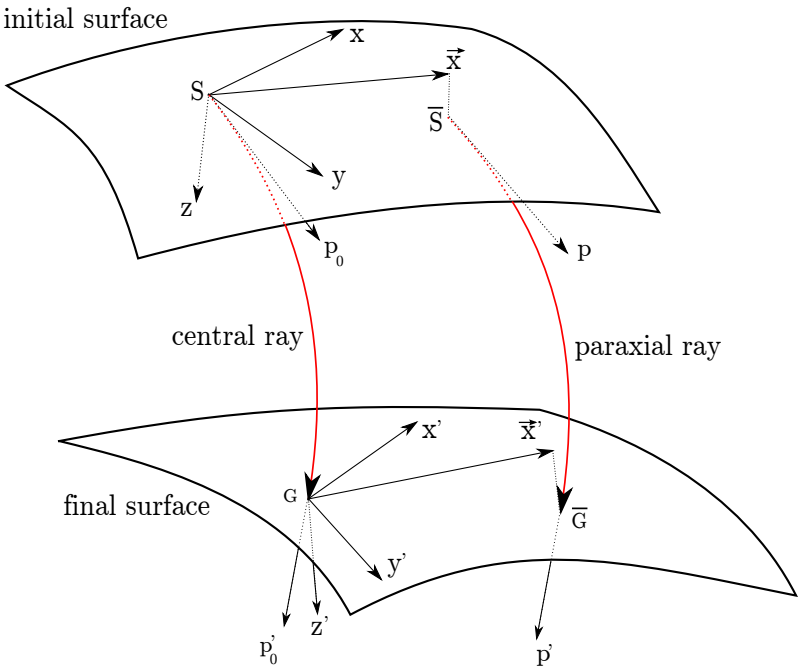

Figure 2.4: A central ray from S to G and a paraxial ray from $\overline{S}$ to $\overline{G}$ links the initial and the final surface cutting through a laterally inhomogeneous medium, modified after Hubral et al. (1992). The two rays are defined by 3D displacement vectors and ray slowness vectors at the initial and the final surface.

pairs $(\mathbf{x}, \mathbf{p}-\mathbf{p}_0)^T$ and $(\mathbf{x}', \mathbf{p}'-\mathbf{p}'_0)^T$ can be established by

$$\begin{pmatrix} \mathbf{x}' \\ \mathbf{p}'-\mathbf{p}'_0 \end{pmatrix} = \underline{\underline{\mathbf{T}}}(G,S) \begin{pmatrix} \mathbf{x} \\ \mathbf{p}-\mathbf{p}_0 \end{pmatrix}. \tag{2.2}$$

Above equation describes a first order relationship of a paraxial ray at its initial and final points by means of the propagator matrix of the central ray $\underline{\underline{\mathbf{T}}}$. Solving equation 2.2 for $\mathbf{p}$ and $\mathbf{p}'$ leads to the following system of equations (e.g. Hubral et al., 1992)

$$\mathbf{p} = \mathbf{p}_0 + \underline{\mathbf{B}}^{-1}\mathbf{x}' - \underline{\mathbf{B}}^{-1}\underline{\mathbf{A}}\mathbf{x} \tag{2.3a}$$

$$\mathbf{p}' = \mathbf{p}'_0 + \underline{\mathbf{D}}\underline{\mathbf{B}}^{-1}\mathbf{x}' - \underline{\mathbf{D}}\underline{\mathbf{B}}^{-1}\underline{\mathbf{A}}\mathbf{x} + \underline{\mathbf{C}}\mathbf{x} \quad , \tag{2.3b}$$

The ray slowness vectors of a paraxial ray at the initial and final surface can be calculated, if the corresponding central ray (i.e. $\underline{\mathbf{A}}$, $\underline{\mathbf{B}}$, $\underline{\mathbf{C}}$, $\underline{\mathbf{D}}$ and $\mathbf{p}_0$, $\mathbf{p}'_0$) and the location of the start and the final point of the paraxial ray is known (Müller, 1999).

2.3.2 Traveltime equations in 3D

The traveltime along the ray from $\overline{S}$ to $\overline{G}$ can be specified in terms of the ray propagator matrix and ray slownesses along the central ray, only (e.g. Müller, 2003; Bergler, 2004). Hamilton's equation describes the traveltime difference between a central ray (SG) and paraxial ray $(\overline{SG})$. Thus, for transmitted rays from the initial surface to the final surface it reads (Bortfeld, 1989)

$$dt = t\left(\overline{S},\overline{G}\right) - t\left(S,G\right) = \mathbf{p}'\mathbf{dx}' - \mathbf{pdx}. \tag{2.4}$$

Substitution of equations 2.3a and 2.3b into equation 2.4 and subsequent integration yields a parabolic traveltime formula for the paraxial ray (see, e.g. Ursin, 1982; Bortfeld, 1989; Hubral et al., 1992; Schleicher et al., 1993)

$$t_{par}\left(\overline{S},\overline{G}\right) = t_0 - \mathbf{p}_0\mathbf{x} + \mathbf{p}_0'\mathbf{x}' - \mathbf{x}\underline{\mathbf{B}}^{-1}\mathbf{x}' + \frac{1}{2}\mathbf{x}'\underline{\mathbf{DB}}^{-1}\mathbf{x}' + \frac{1}{2}\mathbf{x}\underline{\mathbf{B}}^{-1}\underline{\mathbf{A}}\mathbf{x}, \tag{2.5}$$

where t_0 is the traveltime along the central ray. It is valid up to the second-order terms in $\mathbf{x}$ and $\mathbf{x}'$. Schleicher et al. (1993) introduced the 2×2 second-derivative matrices as

$$\underline{\mathbf{N}}_S^G = \left(\frac{\partial^2 t}{\partial\left(x_S\right)_i \partial\left(x_S\right)_j}\right)_{i,j=1,2} = \underline{\mathbf{B}}^{-1}\underline{\mathbf{A}}, \tag{2.6}$$

$$\underline{\mathbf{N}}_G^S = \left(\frac{\partial^2 t}{\partial\left(x_G\right)_i \partial\left(x_G\right)_j}\right)_{i,j=1,2} = \underline{\mathbf{DB}}^{-1}, \tag{2.7}$$

$$\underline{\mathbf{N}}_{SG} = \left(\frac{\partial^2 t}{\partial\left(x_S\right)_i \partial\left(x_G\right)_j}\right)_{i,j=1,2} = \underline{\mathbf{B}}^{-1}. \tag{2.8}$$

Ursin (1982) and Schleicher et al. (1993) demonstrated that another second-order traveltime formula can be obtained from parabolic traveltime approximation. Squaring equation 2.5 and retain only second-order terms in $\mathbf{x}$ and $\mathbf{x}'$, and inserting equations 2.6 to 2.8 into equation 2.5 yields a hyperbolic traveltime form

$$t_{hyp}^2 = \left(t_0 - \mathbf{p}_0\mathbf{x} + \mathbf{p}_0'\mathbf{x}'\right)^2 + t_0\left(-2\mathbf{x}\underline{\mathbf{N}}_{SG}\mathbf{x}' + \mathbf{x}\underline{\mathbf{N}}_S^G\mathbf{x} + \mathbf{x}'\underline{\mathbf{N}}_G^S\mathbf{x}'\right). \tag{2.9}$$

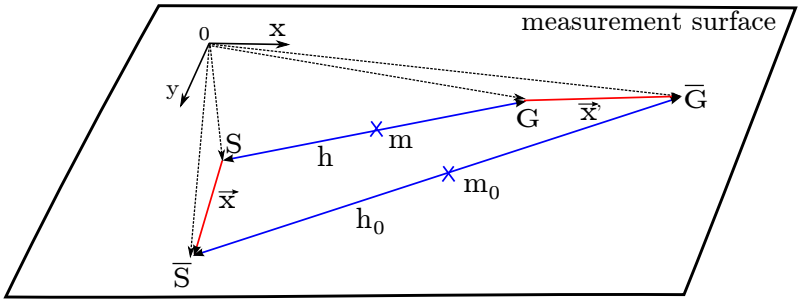

Figure 2.5: Relation between midpoint and half-offset coordinates (blue), displacement vectors (red), and position vectors (dotted). Modified after Müller (2003)

2.3.3 Midpoint and offset coordinates

In reflection seismology, sources and receivers are usually located on the same surface, i.e., the anterior and posterior surfaces coincide (Bortfeld, 1989). This allows to incorporate practically more useful coordinates, midpoint and half-offset. In order to transform from source and receiver coordinates to the new coordinates, in the following, a planar measurement surface which coincides with the (x, y)-plane of the general Cartesian coordinate system is considered. Each source and receiver with coordinates $\mathbf{x}$ and $\mathbf{x}'$ can be described by 2D position and displacement vectors (see Figure 2.5). With simple calculations, midpoint and half-offset coordinates are obtained via (see, e.g. Müller, 2003)

$$\mathbf{m} = \frac{1}{2}\left(\mathbf{x}' + \mathbf{x}\right), \qquad \mathbf{h} = \frac{1}{2}\left(\mathbf{x}' - \mathbf{x}\right). \tag{2.10}$$

Inserting these definitions into equation 2.9 yields hyperbolic traveltime approximation in terms of midpoint and half-offset coordinates

$$\begin{aligned} t_{hyp}^2\left(\mathbf{m}, \mathbf{h}\right) = &\left(t_0 + \frac{\partial t}{\partial \mathbf{m}}\mathbf{m} + \frac{\partial t}{\partial \mathbf{h}}\mathbf{h}\right) \\ &- t_0\left(\mathbf{m}\underline{\mathbf{M}}_{\mathbf{mh}}\mathbf{h} + \frac{1}{2}\mathbf{h}\underline{\mathbf{M}}_{\mathbf{h}}\mathbf{h} + \frac{1}{2}\mathbf{m}\underline{\mathbf{M}}_{\mathbf{m}}\mathbf{m}\right), \end{aligned} \tag{2.11}$$

where

$$\underline{\mathbf{M}}_{\mathbf{h}} = \underline{\mathbf{B}}^{-1}\underline{\mathbf{A}} + \underline{\mathbf{D}}\underline{\mathbf{B}}^{-1} + \underline{\mathbf{B}}^{-1} + \left(\underline{\mathbf{B}}^{-1}\right)^{\mathbf{T}}, \tag{2.12}$$

$$\underline{\mathbf{M}}_{\mathbf{m}} = \underline{\mathbf{B}}^{-1}\underline{\mathbf{A}} + \underline{\mathbf{D}}\underline{\mathbf{B}}^{-1} - \underline{\mathbf{B}}^{-1} - \left(\underline{\mathbf{B}}^{-1}\right)^{\mathbf{T}}, \tag{2.13}$$

$$\underline{\mathbf{M}}_{\mathbf{mh}} = \underline{\mathbf{D}}\underline{\mathbf{B}}^{-1} - \underline{\mathbf{B}}^{-1}\underline{\mathbf{A}} - \underline{\mathbf{B}}^{-1} + \left(\underline{\mathbf{B}}^{-1}\right)^{\mathbf{T}}, \tag{2.14}$$

are second-order derivatives matrices of the traveltime with respect to midpoint and half-offset coordinates (e.g. Schleicher et al., 1993; Müller, 1999, 2003).

Equation 2.11 defines a finite-offset stacking operator in midpoint and half-offset coordinates with a total of 14 independent parameters. In the case when initial and final surface as well as the initial point S and the final point G are coincident, the central ray propagates through an arbitrary inhomogeneous medium and is reflected in itself at the normal-incident-point (NIP) on a chosen reflector. In the case of monotypic waves, the central ray is identical with the zero-offset ray (Hubral, 1983) and, thus

$$\left.\frac{\partial t}{\partial \mathbf{h}}\right|_{\mathbf{h}=0} = 0. \tag{2.15}$$

In addition, it follows that the mixed second-order derivatives of the traveltime vanish Müller (2003)

$$\underline{\mathbf{M}}_{\mathbf{mh}} = 0. \tag{2.16}$$

Making use of the simplifications and the symplecticity relationships (described in, e.g. Schleicher et al., 1993; Müller, 1999, 2003; Bergler, 2004), the hyperbolic zero-offset traveltime approximation can express in much more compressed form:

$$t_{hyp}^2\left(\mathbf{m},\mathbf{h}\right) = \left(t_0 - 2\mathbf{p}_0^{\mathbf{T}}\cdot\mathbf{m}\right)^2 + 2t_0\left(\mathbf{m}^{\mathbf{T}}\underline{\mathbf{M}}_{\mathbf{m}}\mathbf{m} + \mathbf{h}^{\mathbf{T}}\underline{\mathbf{M}}_{\mathbf{h}}\mathbf{h}\right), \tag{2.17}$$

where the vector $\mathbf{p}_0^{\mathbf{T}}$ defines the horizontal projection of the slowness vector. Here, the number of independent variables has been reduced from 14 to 8 (Müller, 2003; Bergler, 2004). Equation 2.17 represents the zero-offset CRS stacking surface, which expands in offset and midpoint coordinates in an arbitrary 3D medium.

2.3.4 Kinematic wavefield attributes

The CRS traveltime derivatives are expressed in terms of physical properties of wavefronts related to the incident/emerging wavefields. In 3D medium, the parameter $\mathbf{p}_0^{\mathbf{T}}$ contains information about the azimuth and the emergence angle (dip) of the emerging central ray. It also includes near surface velocity (Müller, 2003; Bergler, 2004).

The matrices $\underline{\mathbf{M}}_{\mathbf{m}}$ and $\underline{\mathbf{M}}_{\mathbf{h}}$ can be related to the wavefront curvatures of two hypothetical waves, namely the so-called NIP and normal wave (Hubral, 1983). These wavefronts are created by two artificial seismic experiments. Figure 2.6 illustrates the experiments.

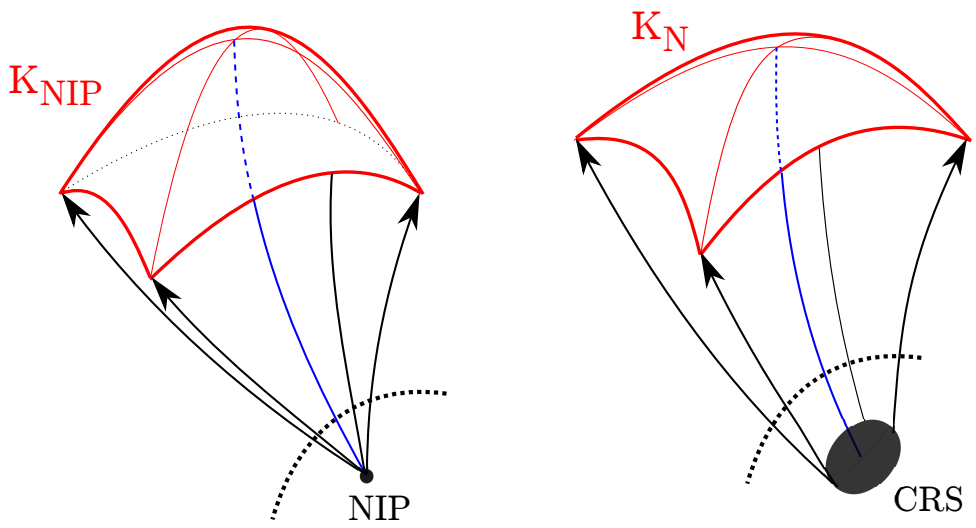

Figure 2.6: The wavefronts of the NIP (left) and normal (right) wavefront propagating along the central ray (blue) are depicted. The NIP wave is emitted by a fictitious point source at the normal incidence point (NIP) (Hubral, 1983), whereas the normal wave is emitted by a curved exploding reflector element, the so-called common reflection surface (CRS). Both parameters are measured at the surface.

The first one, the so-called NIP wave experiment, which is emitted from a fictitious point source on the reflector. The excited wave propagates upward along the central ray and is measured on the surface. The local curvature of the wavefront can be expressed by means of a 2×2 matrix $\mathbf{K}_{NIP}$. Hubral (1983) showed that the matrix $\underline{\mathbf{M}}_{\mathbf{h}}$ can be expressed in terms of the curvature of the NIP wavefront by

$$\underline{\mathbf{M}}_{\mathbf{h}} = \frac{2}{v_0}\mathbf{H}\mathbf{K}_{\mathbf{NIP}}\mathbf{H}^T, \tag{2.18}$$

where $\mathbf{H}$ is the upper left 2×2 submatrix of the transformation matrix from the ray-centered Cartesian to the global Cartesian coordinate system (Spinner, 2007).

The second experiment is the normal wave experiment, in which a whole curved reflector segment in the vicinity of the NIP is assumed to be densely covered with point sources. If all these sources are excited at the same time, a wave is generated with a local wavefront curvature equal to the one of the reflector. The corresponding rays are normal to the reflector and the associated wave is called normal wave (Hubral, 1983). The wave emerges at the measurement surface with the wavefront curvature defined by a 2×2 matrix $\mathbf{K}_N$. As only normal rays are involved in the considerations, the experiment equals a zero-offset experiment. The curvature matrix $\mathbf{K}_N$ of the normal wave can be related to the matrix $\underline{\mathbf{M}}_{\mathbf{m}}$ via

$$\underline{\mathbf{M}}_{\mathbf{m}} = \frac{2}{v_0}\mathbf{H}\mathbf{K}_{\mathbf{N}}\mathbf{H}^T. \tag{2.19}$$

The two angles α and ϕ together with the six independent elements of the symmetric matrices $\mathbf{K}_{NIP}$ and $\mathbf{K}_N$ are summarized as kinematic wavefield attributes in three dimensional space. In case of an homogeneous overburden, the attributes can be directly related to properties of the reflector: α and ϕ correspond to the dip and orientation of the reflector element at the NIP. It is evident that $\mathbf{K}_N$ carries information about the reflector curvature, whereas $\mathbf{K}_{NIP}$ carries information about the overburden and depth (Mann, 2002).

After simple substitution of equations 2.18 and 2.19 into the traveltime approximation 2.17 and considering $\Delta\mathbf{m} = \mathbf{m} - \mathbf{m}_0$, it reads (e.g. Müller, 2003; Bergler, 2004)

$$\begin{aligned} t_{hyp}^2(\Delta\mathbf{m}, \mathbf{h}) = &(t_0 + 2\mathbf{p}_m \cdot \Delta\mathbf{m})^2 \\ &+ \frac{2t_0}{v_0}\left(\Delta\mathbf{m} \cdot \mathbf{H}\mathbf{K}_N\mathbf{H}^T\Delta\mathbf{m} + \mathbf{h} \cdot \mathbf{H}\mathbf{K}_{NIP}\mathbf{H}^T\mathbf{h}\right). \end{aligned} \tag{2.20}$$

The equation above is the conventional form of the hyperbolic stacking operator used in the 3D CRS approach.

The reduction from 3D to 2D models is straightforward. In a 2D model the material parameters depend only on x- and z-coordinates. The initial surface and the ending surface reduce to curves. Thus, the two-component vectors become scalars and the 4×4 propagator matrices reduce to 2×2 matrices (see, e.g. Müller, 1999, 2003; Bergler, 2004).

2.3.5 The 2D case

Schleicher et al. (1993) followed Shah (1973) and Hubral and Krey (1980) in order to express the parabolic and hyperbolic paraxial traveltime equations in terms of midpoint and half-offset coordinates. Afterwards, Tygel et al. (1997) combined that result with the formulation of the propagator matrix in terms of wavefront curvatures according to Hubral (1983). Their combination allows to a parabolic paraxial traveltime approximation in 2D in terms of the CRS stack parameters:

$$t_{par}(\Delta m, h) = t_0 + \frac{2\sin\alpha}{v_0}\Delta m + \frac{\cos^2\alpha}{v_0}\left(K_N\Delta m^2 + K_{NIP}h^2\right). \tag{2.21}$$

For simple layered media, Ursin (1982) showed that the hyperbolic traveltime formula better describe near-vertical reflections. If Equation 2.21 is squared and only the terms up to second-order in midpoint and half-offset are retained (Schleicher et al., 1993), the hyperbolic traveltime equivalent is obtained via

$$t_{hyp}^2\left(\Delta m, h\right) = \left(t_0 + \frac{2\sin\alpha}{v_0}\Delta m\right)^2 + \frac{2t_0\cos^2\alpha}{v_0}\left(K_N\Delta m^2 + K_{NIP}h^2\right). \tag{2.22}$$

Assuming that the correct CRS stacking parameters are known for every time sample in the ZO section as well as near surface velocity (v_0), the prestack data can be summed up along the stacking surfaces (extended in the both midpoint and half-offset directions) defined by the parameter triplets (α, K_{NIP} *and* K_N). The summation result is then assigned to the specific zero-offset time sample in the time domain. Since the subsurface structure is in general unknown, the correct CRS stacking parameters are unknown, too. Therefore, the important part of the CRS stacking procedure is the determination of the stacking parameters which is briefly reviewed in the next section.

2.4 CRS implementation

The CRS wavefield attributes for each ZO location are determined automatically by means of coherence analysis, e.g., the semblance norm (Taner and Koehler, 1969) along the stacking operator

$$S = \frac{\sum_{j=-W/2}^{W/2}\left(\sum_{i=1}^{N} f_{i,j+k(i)}\right)^2}{N\sum_{j=-W/2}^{W/2}\sum_{i=1}^{N} f_{i,j+k(i)}^2}, \tag{2.23}$$

where $f_{i,j}$ denotes the amplitude of the j^{th} sample of the i^{th} trace of N traces. A time window of width W is defined around the CRS operator at sample $k(i)$. A good choice for the length of the time window is the dominant period in the data (see Figure 2.7). Whenever the coherency is maximized, an optimal parameter set is found. It is optimal in the sense that its associated hyperbolic traveltime surface fits an event in the prestack data best. The data is then summed up along this stacking surface. The summation result is placed into the respective ZO time sample.

However, the search for all CRS parameters at the same time is a cumbersome and time-consuming process which requires large computational resources. To avoid computational costs, Müller et al. (1998) suggested that the search for the stacking parameters can be split up into three one-parametric independent searches in the 2D CRS. Each search is performed in a lower dimension subset of data, e.g., in CMP or ZO domain. Thus, it reduces the number of parameters to determine and speeds up the calculation. This approach is called the pragmatic search strategy and allows to obtain initial values for CRS parameters. However, since the initial wavefield attributes are determined in three one-parametric searches, it cannot be expected that the three one-parametric searches yield the same results as the multi-parameter search. Therefore, in order to find the best

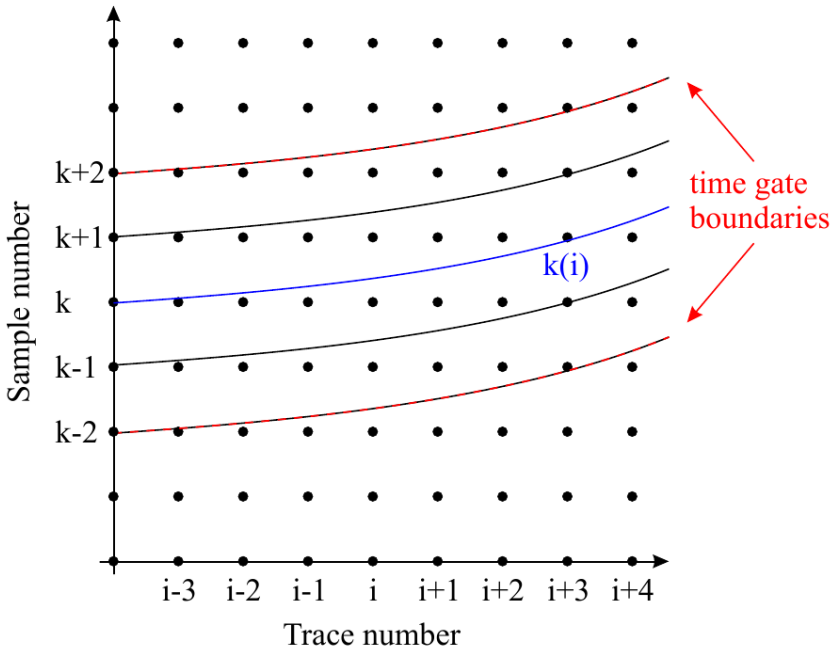

Figure 2.7: The semblance S for a sample k is evaluated from a multitude of time shifted CRS operators within a time window that is disposed symmetrically around the test sample in CMP configuration (modified after Müller, 2003).

possible stacking parameters, the initial values serve as input to an optimization algorithm. The optimization will in most cases not only enhance the quality of the stack section, but also of the determined parameters. This is of great importance when applying subsequent applications based on these CRS attributes. A large variety of optimization algorithms is available in literature and ranges from the flexible polyhedron search (Nelder and Mead, 1965) to the simulated annealing algorithm (Press et al., 2002).

In the same fashion with 2D, the eight kinematic wavefield attributes of the 3D CRS stacking operators are determined by means of a coherence analysis. In order to obtain efficient search strategies, Müller (2003) and Bergler (2004) suggested a solution using the split stacking operators and a combination of two techniques: a linear search defining initial attributes and a simulated annealing method for the final results. In the context of this thesis, I do not use the refined attributes to keep computational costs low.

2.5 General remarks

2.5.1 Aperture considerations

The spatial extent of the CRS stacking operator is called aperture. The aperture size in midpoint and offset directions must be chosen appropriately to obtain optimal CRS parameters and stacked sections. For large apertures, the hyperbolic traveltime approximation may no longer be valid, whereas a small aperture may decrease the quality of the CRS parameter estimation. The proper choice of the offset and midpoint apertures depends on the characteristics of the data set under consideration, and is usually done after performing some numerical tests with the data. Furthermore, apertures for the CRS parameter search and for the actual stacking might be chosen independently. The size of offset aperture is often determined by the offset-to-target ratio. This is a good approximation because for a stratified medium the assumption of a hyperbolic traveltime curve is valid in that range. The target depth can be estimated with a starting velocity and the ZO traveltime (Bobsin, 2014). The midpoint aperture is not as easily determined as the offset aperture. Many authors, like Hertweck et al. (2003); Schleicher et al. (1997); Mann (2002), suggested the size of the projected Fresnel zone as the optimal midpoint aperture.

2.5.2 Spread-length bias

An important issue related to the reliability of the parameter search routines is that for non-hyperbolic events, the coherence analysis yields second-order stacking parameters and traveltimes that are biased by higher-order contributions. This effect which is proportional to the size of the search aperture is termed as spread-length bias and is also well known from conventional stacking analysis (Al-Chalabi, 1973; Hubral and Krey, 1980). The biased attributes determined in this way no longer represent second-order but best-fit parameters. Thus, they are not optimal for further second-order applications. The impact of the spread-length bias can be reduced by choosing small search apertures. However, the stable evaluation of normal and NIP wavefront curvatures requires sufficiently large move-out in the data.

2.5.3 Conflicting dips

Most current implementations of the CRS operator, e.g., the pragmatic approach, suffer from the occurrence of conflicting dip situations in the acquired data. In the case of a conflicting dip situation, where a strong unwanted event crosses a weak wanted event respectively, e.g., a reflection and a diffraction event, the latter may not be imaged very well. Conflicting dips may happen frequently in complex and semi-complex structures where the seismic events are faulted or pulled up by a salt dome or anticlines. The current 2D strategy to handle conflicting dips is equivalent to stacking data with different emergence angles

$\alpha^{(i)}$, where index i denotes the different contributing events (see, e.g. Soleimani et al., 2009; Walda and Gajewski, 2015). This strategy has some advantages that improve the continuity of reflection events as well as diffractions in the presence of conflicting dip situations.

Handling of conflicting dips in 3D still is a cumbersome task and needs to be addressed more. Müller (2009) suggested a modified workflow that utilizes the path summation technique to obtain an improved input for the conflicting dip search in the zero-offset domain. The actual detection is done by means of an adapted peak detection algorithm. For each detected event consistent sets of attributes are obtained by a newly introduced search step.

In the context of this thesis the conflicting dips are not handled.

Chapter 3

Prestack diffraction separation and imaging

The CRS attributes approximate the kinematic reflection response of a reflector segment as well as the response of a diffraction. Diffractions and reflections can thus be separated by means of the CRS attributes. I start this chapter with the importance of diffractions for the detection of small-scale heterogeneities. Afterwards, I present a method to effectively separate diffractions from reflections before stacking. The new method is based on the combination of an existing threshold function by Dell and Gajewski (2011) and the partial CRS stack technique by Baykulov and Gajewski (2009). The existing threshold function makes use of CRS attributes to identify diffractions in the data. The partial CRS stack is a robust technique for data regularization and enhancement. Both methods are explained in detail in the following. Afterwards, I present a diffraction-based method for migration velocity analysis. Subsequently, I apply time migration tuned to diffraction velocities on the diffraction-only data. To examine the performance of the proposed method, it is tested on a complex synthetic as well as a field data.

3.1 Diffractions and resolution in data processing

Diffracted waves are a direct indicator of small to medium scale heterogeneities in the subsurface and of the presence of faults, karsts, fracturing, local structures, lithological elements and structural changes. Therefore such waves carry useful information about the subsurface and can play a significant role in the geological interpretation of hydro-carbonate environments. For example, the identification of fracture density and orientation allows reservoir engineers to design an optimal well placement program that targets important spots, areas with increased production, and minimizes the number of wells used for a prospective area (Sturzu et al., 2014).

From a physical point of view, diffractions allow to distinguish objects with typical sizes

that are significantly smaller than the dominant wavelength. This fact links them to super-resolution. Most of suggested methods to increase the seismic resolution involve the image processing because they are only applied to seismic images, e.g, deconvolution techniques (see, e.g. Yilmaz, 2001). These methods might be effective in the detection of some details, but their resolution is limited to the Rayleigh criterion. With these methods, elements that are smaller than half of the wavelength can not be interpreted consistently. On the other hand, decreasing the wavelength of the seismic waves reflected at the target is almost impossible since in addition to the earth effect as a low pass filter, the high frequencies that are present in the data are often lost during standard processing (Khaidukov et al., 2004).

To see the influence of diffractions in the data, special care should be taken into account during the acquisition, processing and interpretation in order to preserve such weak signals:

- data acquisition in a dense grid with short receiver spacing, high fold, and with a sufficiently high signal-to-noise ratio.
- preservation of all diffracted energy during processing.
- diffraction separation should be performed without harming the frequency content of the signals (see e.g., Grasmueck et al., 2013).

However, diffraction data can be used as a supplement to the structural images produced by reflection imaging. In fact, the goal of diffraction imaging is not to replace these traditional techniques, but rather to provide interpreters with an additional image with structural details.

3.1.1 Diffraction characteristics

Diffractions are typically one or two orders of magnitude weaker than specular reflections from the same depth (Krey, 1952; Landa et al., 1987). Diffraction tails are especially weak signals. Khaidukov et al. (2004) discussed the concept of super-resolution achieved through diffraction imaging, which is defined as the recovery of smaller details beyond the seismic wavelength, or sub-wavelength. In general, a reflection can be defined as a seismic response from smooth interfaces if the wavelength is significantly lower than the boundary curvature radius. On the other hand, if the curvature radius is reduced and becomes comparable to the wavelength, Snell's law becomes inapplicable. A seismic response from such a curved interface is technically called diffraction (see, e.g. Landa et al., 1987; Kanasewich and Phadke, 1988)

Although dynamic features of various types of diffractions are different, their kinematics follow the same laws (Keller, 1962; Berryhill, 1977; Klem-Musatov, 1995; Landa, 2013). Figure 3.1 illustrates a point and an edge diffraction model and their seismic response in

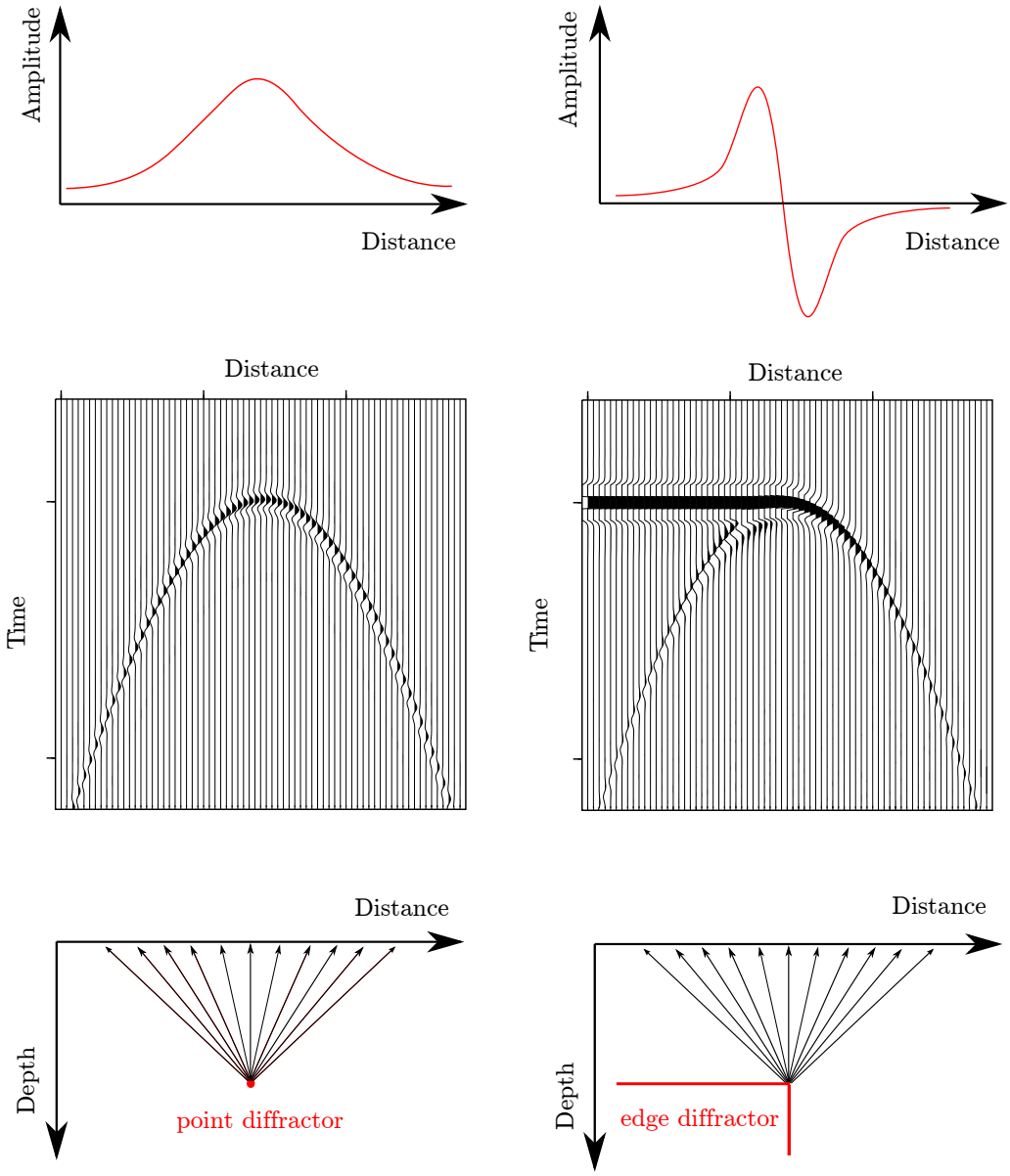

Figure 3.1: Illustration of two types of diffractions. Point diffraction (left) and edge diffraction (right). Top: amplitude along the two diffractions. Middle: diffraction traveltimes in a common-offset gather. Bottom: depth model and rays. One can see that the edge diffraction exhibits a 180 degrees change in the polarity which differentiates it from the point diffraction. In this case, the maximum amplitude in a common-offset section occurs where the diffraction meets the reflection.

the time domain. At the edge, the diffraction undergoes a phase change of 180 degrees compared to the reflection. This implies that the edge diffraction hyperbola is divided into two regions in which the algebraic signs of the amplitudes are opposite. The forward scattered part of the hyperbola that stems from the associated reflection has the same polarity, while the backward scattered part beneath the reflection has the opposite polarity. In contrast, the point diffraction does not exhibit any phase reversal. In the case of an edge, a horizontal reflecting truncated layer is tangent to the diffraction hyperbola at its apex. The amplitude of the edge diffraction hyperbola is half the absolute value of the amplitude of the reflection from the truncated layer. The maximum amplitude occurs in a seismic stacked section where the diffraction meets the reflection. This position in not equal to the apex of the diffraction hyperbola if the reflector is dipping (Dell, 2012).

In general, a diffraction event is a symmetric curve with the apex over the point diffractor or exactly at the top of an edge. However, diffraction events might look different in various seismic reference systems, e.g., common-shot (CS) configuration. Therefore, they are not easy to recognize among other wavefields. On the other hand, since traveltime curves of reflections and diffractions coincide in a CMP gather, it again leads to difficulties to distinguish diffractions. In contrast, diffractions are often visible in brute stacks because their traveltime move-out is much higher in common-offset (CO) sections. Considering this fact, diffraction detection is much easier in the common-offset domain.

Detection of diffractions based on their dynamic properties is very challenging. For instance, the phase of an edge diffraction in CMP gathers does not show any change in the polarity. This effect can lead to a smeared image after stacking since phase-reversed amplitudes cancel out each other. Moreover, some diffractions, e.g., point diffraction, as it was mentioned above, do not exhibit any phase reversal. Thus the kinematic features of diffractions are preferable for their identification and subsequent separation (Landa et al., 1987).

3.1.2 Detection and separation of diffractions

As it is outlined in the introduction, the importance of diffracted waves in reflection seismology has long been recognized. Primarily, the objective was to detect diffracted waves in data. Hubral (1975) studied the determination of the diffractor location in a constant velocity medium with dipping layers. Klem-Musatov et al. (2008) developed the theory of an asymptotic description of seismic diffracted waves in structurally complex media.

Over recent years, diffraction separation and imaging in the prestack domain has been partially studied. Khaidukov et al. (2004) proposed a reflection-stack type of migration of prestack shot gathers to focus reflections to a point and smear diffractions over a large area. Muting the reflection focus and defocusing the residual wavefield results in a shot gather that contains diffraction-only data. Kozlov et al. (2004) presented diffraction imaging in depth using a modified Kirchhoff migration, where the migration aperture was tapered

to filter out the specular energy. Fomel et al. (2007) developed a method for wavefield separation and diffraction imaging based on the so-called plane-wave destructor. This method can be applied to common offset gathers and used to obtain a migrated section based on the optimally focused diffracted component of the wavefield. Moser and Howard (2008) proposed a method for diffraction imaging in the depth domain in the context of prestack depth migration. The idea behind this is that a general migration process can be divided into two stages: one that utilizes specular reflections and one that suppresses them. Building a special weight function in the migration operator that suppresses the plane component of the wavefield allows to generate diffraction-only data.

More recently, diffraction separation in common-image-gathers (CIG) has become interesting. The analysis of a CIG in the coordinates of structural angles has shown significant differences in the behavior of reflected and diffracted waves and this phenomenon could be thus used for their separation (see e.g., Landa et al., 2008; Reshef and Landa, 2009). In this domain the reflections are always convex, while the diffractions are straight lines. Landa et al. (2008) and Klokov and Fomel (2012) suggested a separation method based on filtering in the Radon transformed image using the offset vertex of a parabolic curve to parameterize the reflected wave and a quasi-linear parameterization for the diffracted one.

However, these methods are only based on the suppression of the reflection, and the assumption that what remains after reflection suppression are diffracted wave fields. They do not consider the kinematic or dynamic characteristics of diffractions. In an attempt to isolate diffractions based on the kinematic characteristics, Berkovitch et al. (2009) presented a method to detect local heterogeneities in a medium using a new kinematic correction for diffracted waves. This correction is based on the multifocusing method (see e.g., Gelchinsky et al., 1999) and has a very high accuracy to describe the kinematics of diffracted waves for arbitrary source and receiver positions. In a similar kinematic-based approach, Dell and Gajewski (2011) proposed a method to separate reflections and diffractions by using the CRS attributes. The process consists of stacking the coherent events with a CRS-based operator followed by the attenuation of reflected events in the poststack domain with a new type of diffraction-filter. The filter is based on the CRS attributes and can distinguish diffractions from reflections.

In the context of this thesis, I focus on the kinematic features of diffractions using the insightful CRS wavefield attributes which have a physical interpretation and account for diffraction identification best. Therefore in the next section, I briefly review the kinematic characteristics of diffractions and I continue with two important diffraction traveltime approximations, the double-square-root (DSR) and the CRS-based diffraction operator (Soleimani et al., 2009) equations.

3.1.3 Diffraction Kinematics

The basic idea of the Kirchhoff diffraction stack is that a reflector can be seen as an ensemble of diffractors, each of them representing a secondary source or Huygens source in

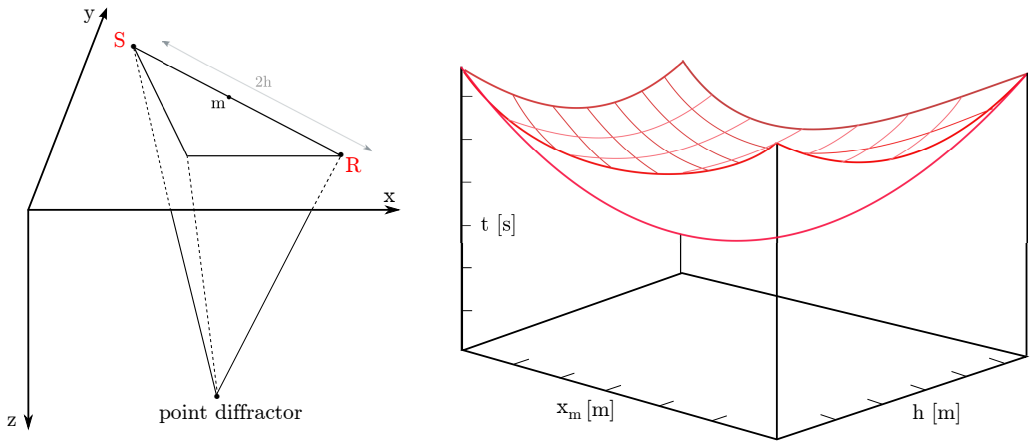

Figure 3.2: A 3D sketch of a point diffractor in a homogeneous space with the geometry of source and receiver (left). The 2D diffraction traveltime response due to the point diffractor (commonly known as Cheops pyramid) equivalent to the DSR equation in midpoint-offset space (right).

the subsurface. The reflective response is then the superposition of elementary diffractions from these points and the reflection traveltime surface is the envelope of the elementary diffraction traveltime surfaces (Dell, 2012). In this sense, a real scatterer or diffractor is usually a small object in comparison to the dominant wavelength which can be understood as a small reflector with an infinite curvature and undefined orientation (Mann, 2002). Based on the Kirchhoff integral method, the elementary 2D diffraction traveltime equation is given by (Claerbout, 1985)

$$t_D = \sqrt{\frac{t_0^2}{4} + \left(\frac{x_m - h}{v}\right)^2} + \sqrt{\frac{t_0^2}{4} + \left(\frac{x_m + h}{v}\right)^2}, \tag{3.1}$$

where t_0 is the zero-offset time, h is the half-offset, x_m is the midpoint and, v is the medium velocity.

Figure 3.2 displays a traveltime surface which is the diffraction impulse response from a point diffractor in midpoint-offset coordinates. Although the Kirchhoff-type traveltime equation is derived using the straight-ray assumption, it can be generalized to a hyperbolic relationship by a Taylor series expansion for an arbitrary medium (see, e.g., Geiger, 2001; Vanelle and Gajewski, 2002). However, DSR has better accuracy (see, e.g. Vanelle et al., 2010; Schwarz et al., 2012)

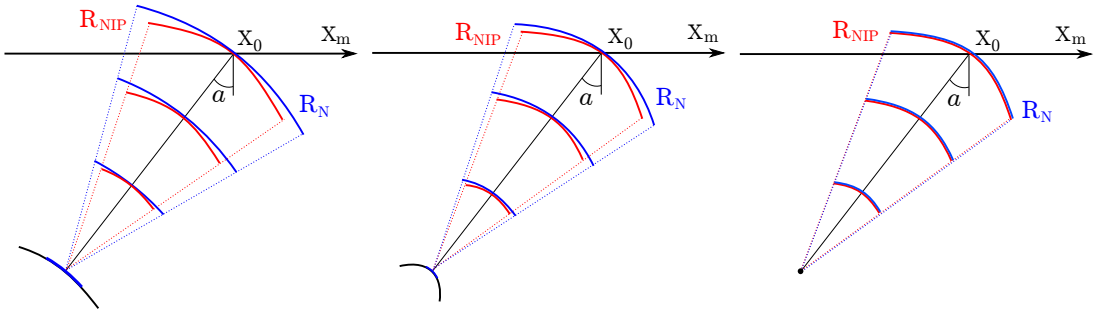

Figure 3.3: Illustration of the CRS approach for diffracted events. Red lines delineate the Normal waves, blue lines delineate the NIP waves. With decreasing reflector curvature, the radii of R_N and R_{NIP} become closer. As opposed to reflections, for diffractions any direction describes a possible zero-offset ray along which the NIP- and normal wave can be considered.

3.1.4 CRS for diffractions

Although Equation 2.22 was initially derived for reflections, it can also be applied for diffractions since, according to Mann (2002), a diffractor can be described by a reflector of undefined orientation and infinite curvature. The latter property implies that the common-reflection-surface shrinks into a point and thus for diffractions $R_N = R_{NIP}$. This concept is illustrated in Figure 3.3, showing that with decreasing reflector curvature, the radii of R_N and R_{NIP} become closer. Therefore, in the diffraction case, Equation 2.22 is simplified to

$$t^2_{CRSD}(\Delta x_m, h) = \left(t_0 + \frac{2\sin\alpha}{v_0}\Delta x_m\right)^2 + \frac{2t_0\cos^2\alpha}{v_0 R_{NIP}}\left(\Delta x_m^2 + h^2\right), \tag{3.2}$$

where v_0 is the near surface velocity. The ZO traveltime is t_0. The midpoint displacement and offset are Δx_m and h, respectively. The CRS parameter R_{NIP} is the radius of curvature of the wavefront of the NIP wave and α is the incidence angle.

Equation 3.2 represents the CRS-based diffraction operator which approximates the diffraction response up to second-order (Mann, 2002). If it is applied as a stacking operator, the stacking will enhance the diffractions and suppress the reflections, ideally resulting in diffraction-only data.

As it was mentioned before, the radii of curvature of the NIP- and N-wave coincide for diffractions. Thus, the ratio of R_{NIP} and R_N can be a good criterion to separate diffractions from reflections. In the ideal case, a diffractor should yield a ratio of R_{NIP}/R_N equal to one. However, in practice, we find that for diffractions R_N will be close to R_{NIP}, but the values will generally not coincide exactly. This is due to the band-limited nature of the data. In order to ensure a reliable detection, Dell and Gajewski (2011) proposed the following exponential threshold function for diffraction detection

$$W_D = \exp\left(-\frac{|R_N - R_{NIP}|}{|R_N + R_{NIP}|}\right) \quad . \tag{3.3}$$

If R_{NIP} and R_N are close to each other, i.e., for diffractions, the function W_D will be close to one. The function value will be close to zero for reflections. Therefore a user-chosen threshold can be applied to identify diffractions: If the value of W_D is above the threshold, the data is stacked and if it is below, the data is not stacked. By this weighting procedure, reflection energy can effectively be removed. However, the choice of the threshold can be problematic. If the threshold is chosen too low, reflection events are not fully suppressed. An overestimated choice of the threshold, on the other hand, can suppress diffracted energy as well.

Guntern (2013) and Voss (2013) have investigated the influence of the threshold function by Dell and Gajewski (2011) on synthetic and field data. They found that the choice of the threshold determines the amount of residual reflected energy in the aimed-for diffraction-only stack. In conclusion, the threshold is heavily sensitive to the complexity of the medium and the data quality. Effectiveness of the threshold function in pre- and poststack diffraction separation is further discussed in the chapter 5.

Since poststack diffraction separation has been proven to be vulnerable to the presence of strong noise (see, e.g. Dell and Gajewski, 2011; Bakhtiari Rad and Gajewski, 2015; Bakhtiari Rad et al., 2015b; Bauer et al., 2015; Schwarz, 2015), I suggest to separate diffractions from reflections in the whole volume of prestack data by changing the kernel of the partial CRS introduced by (Baykulov and Gajewski, 2009) which is a robust technique for prestack data enhancement and regularization.

3.1.5 Partial CRS stack

The Partial CRS method is derived from the ZO CRS stack, where the same parameters are used as in the CRS stack, i.e., no additional stacking parameter is required. The partial CRS surface is used to sum up the finite-offset data coherently within an aperture expanded in both midpoint and half-offset coordinates without any further common-offset (CO) processing. The CO CRS stack technique (Zhang et al., 2008) may provide more accurate compared to the partial CRS especially in complex media. However, due to the large number of the CO CRS parameters, the problem is of higher dimensionality, which makes processing less stable and computationally more expensive (Bauer et al., 2015). In fact, the partial CRS technique combines the stability of zero-offset processing with the improved illumination of common-offset processing.

As it is illustrated in Figure 3.4, partial CRS stacking is carried out over a reduced aperture centered on the finite-offset position instead of a full stacking. Accordingly, the stacking result is written not to the zero-offset coordinate $(x_0, t_h, h = 0)$ but to a finite-offset position with the coordinates $(x_0, t_h, h \neq 0)$. Therefore, it allows to generate a new trace at this position with an increased signal-to-noise ratio. The new trace can therefore be considered

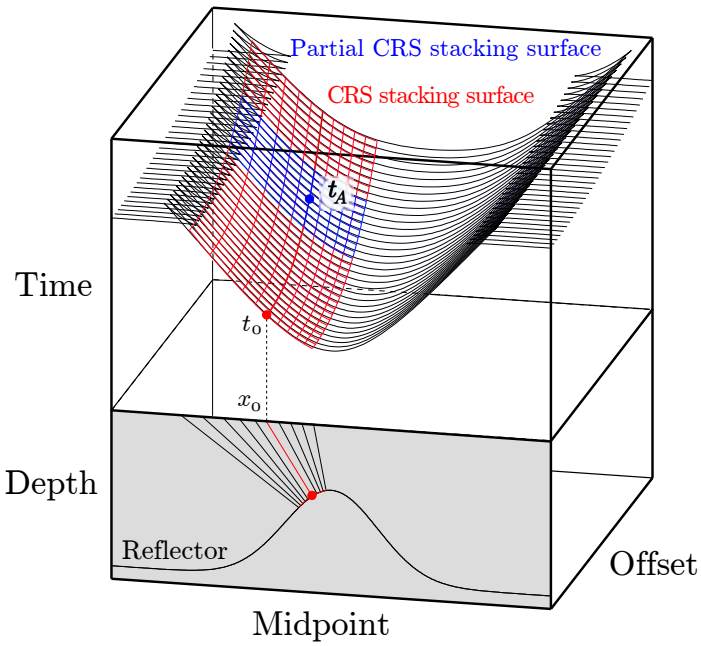

Figure 3.4: Sketch of a 2D model and the resulting data (modified after Müller, 2003; Baykulov and Gajewski, 2009): the black lines represent the multi-coverage data in the midpoint and half-offset domain. The red surface is the CRS stacking surface corresponding to an arbitrary point on the reflector. In the case of the CRS stack, the summation result is assigned to a ZO point with coordinates $(x_0, t_0, h = 0)$. However, in the case of partial stacking for a finite-offset point with coordinates $(x_0, t_A, h \neq 0)$, the traces are stacked along the blue surface and assigned to the same finite-offset point.

equivalent to a prestack trace. Repeated application for all offsets thus provides enhanced prestack data.

However, in the proposed workflow for prestack diffraction separation, the diffraction weight function initially evaluates every ZO sample whether the sample belongs to a diffraction or not. If not, nothing is extrapolated for reflections. If yes, in the next step, the ZO CRS attributes related to every finite-offset diffraction sample should be determined via a best-fitting search process. Here I use the solution suggested by Baykulov and Gajewski (2009) to determine the attributes for the related ZO attributes. It reads as described by the ZO time to:

$$t_0 = -\frac{h_A^2 \cos^2 \alpha}{v_0 R_{NIP}} + \sqrt{\left(\frac{h_A^2 \cos^2 \alpha}{v_0 R_{NIP}}\right)^2 + t_A^2}, \tag{3.4}$$

where t_A is the finite-offset traveltime of the diffraction sample under consideration, h_A is the finite-offset $(h_A \neq 0)$.

In the following, I discuss the accuracy of different types of the traveltime approximations

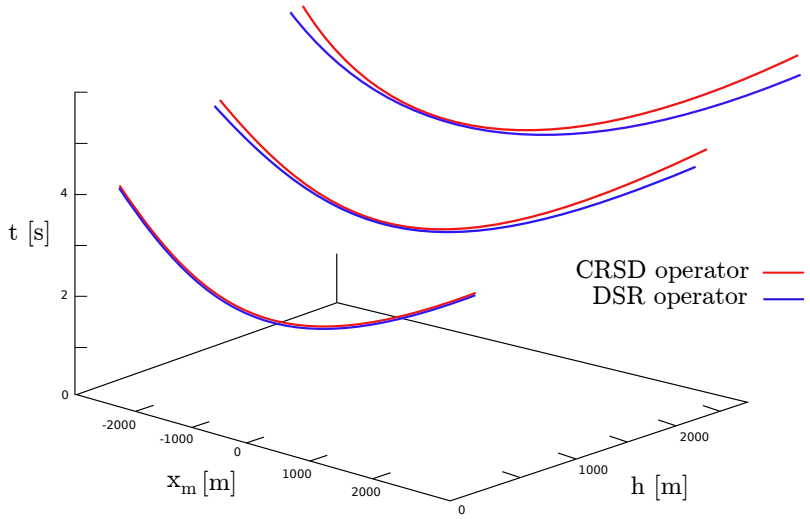

Figure 3.5: Double-square-root (DSR) and CRS-based diffraction (CRSD) operator for a 2D homogeneous model with a single point diffractor at a depth of 1 km. The model parameters were taken according to Dell (2012). The velocity is 1500 m/s. The operators coincide in the planes defined by $x_m = 0$ and $h = 0$. The larger the offset, the more the operators deviate from each other.

for diffractions.

3.1.6 CRSD versus DSR approximations

In a homogeneous medium, where the rays are straight lines, the diffraction traveltime can be computed by the double-square-root (DSR) operator. In contrast, the CRSD operator is a single-square root operator which coincides with the DSR operator for zero-offset, i.e., for $h = 0$. For offsets higher than zero, the DSR traveltime surface and the CRSD traveltime surface deviate from each other. This fact is investigated for a simple point diffractor in depth as seen in Figure 3.5. For larger offsets, the DSR operator approximates the diffraction traveltime better than the hyperbolic CRS (see, e.g. Dell, 2012). Thus, I suggest to use a double-square-root-based CRS operator to stack diffractions properly which is presented in the next section.

3.1.7 The implicit CRS (i-CRS)

The conventional CRS operator may exhibit a suboptimal fit to non-hyperbolic events, e.g., diffractions. Hence, it can be shown that the hyperbolic CRS expression is not ideally suited for imaging diffractions or reflectors of high curvature (see, e.g. Vanelle et al., 2010; Schwarz et al., 2012). However, because the imaging of small objects plays an important

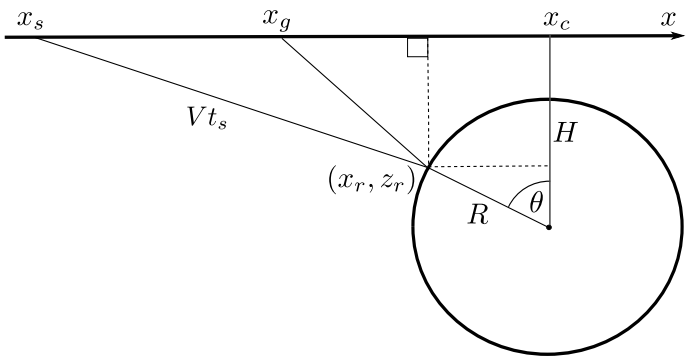

Figure 3.6: i-CRS geometry after Schwarz et al. (2012). The circle is described by its center point (x_c, H) and the radius R. The constant velocity is denoted by V. The angle θ can be determined in an implicit way by evaluating Snell's law (Vanelle et al., 2010).

role in a complex geologic setting, double-square-root-based approximations have gained increasing attention in recent years. The conventional CRS operator can be modified to fit events with a high curvature. The implicit CRS (or i-CRS) method introduced by Vanelle et al. (2010) and its optically shifted version (Schwarz et al., 2012) are DSR-based CRS-type operators which are designed as a sum of two single square roots. Another DSR-based CRS-type stacking operator is multifocusing method which is not considered in the context of this thesis. For a detailed description of the multifocusing method, I refer to Gelchinsky et al. (1999).

The i-CRS approach results from Fermat's principle and represents an implicit method to find the best stacking operator. The i-CRS operator represents a sum of two square roots and for an isotropic homogeneous 2D medium is expressed as

$$t = t_s + t_g, \tag{3.5}$$

where t_s and t_g are the traveltimes from the source and receiver to the reflection point, respectively. Thus they are equal to

$$t_s = \frac{1}{V}\sqrt{(x - h - \Delta x_c - R\sin\theta)^2 + (H - R\cos\theta)^2} \tag{3.6}$$

and

$$t_g = \frac{1}{V}\sqrt{(x + h - \Delta x_c - R\sin\theta)^2 + (H - R\cos\theta)^2}. \tag{3.7}$$

The following relationship between CRS and effective i-CRS parameters was derived and throughly investigated by Schwarz et al. (2012):

$$V = \frac{v_{NMO}}{\sqrt{1 + \frac{v_{NMO}^2}{v_0^2}\sin^2\alpha}} \quad , \tag{3.8a}$$

$$\Delta x_c = \frac{-R_N \sin\alpha}{\cos^2\alpha\left(1 + \frac{v_{NMO}^2}{v_0^2}\sin^2\alpha\right)} \quad , \tag{3.8b}$$

$$H = \frac{v_0 R_N}{v_{NMO}\cos^2\alpha\left(1 + \frac{v_{NMO}^2}{v_0^2}\sin^2\alpha\right)} \quad , \tag{3.8c}$$

$$R = \frac{\frac{v_0 R_N}{v_{NMO}\cos^2\alpha} - \frac{v_{NMO} t_0}{2}}{\sqrt{1 + \frac{v_{NMO}^2}{v_0^2}\sin^2\alpha}} \quad , \tag{3.8d}$$

with the normal moveout velocity

$$v_{NMO} = \sqrt{\frac{2 v_0 R_{NIP}}{t_0 \cos^2\alpha}} \quad . \tag{3.9}$$

The i-CRS parameters are shown in Figure 3.6. The angle θ is the common offset reflection angle, which for an arbitrary common offset can be determined iteratively as

$$\tan\theta = \tan\theta_0 + \frac{h}{H}\frac{t_s - t_g}{t_s + t_g}, \tag{3.10}$$

where θ_0 is the ZO reflection angle. Numerical studies revealed that the application of the reflection angle updated by more than one iteration does not lead to an increase in accuracy (Vanelle et al., 2010; Schwarz et al., 2012).

For the special case of diffractions, the number of wavefield attributes needed to properly approximate the corresponding diffraction response reduces to two (R=0). Therefore we end up with the following explicit expression

$$t_{i-CRSD} = t_s + t_g \quad , \tag{3.11a}$$

$$t_s = \frac{1}{V}\sqrt{(x - h - \Delta x_c)^2 + H^2} \quad , \tag{3.11b}$$

$$t_g = \frac{1}{V}\sqrt{(x + h - \Delta x_c)^2 + H^2} \quad , \tag{3.11c}$$

Figure 3.7 displays the coherence sections of the hyperbolic CRS and i-CRS operators for a simple model with an approximated point diffractor ($R = 10m$) and overburden velocity of 1500 m/s in a depth of 1 km, and a planar reflector in a depth of 2 km. One can observe

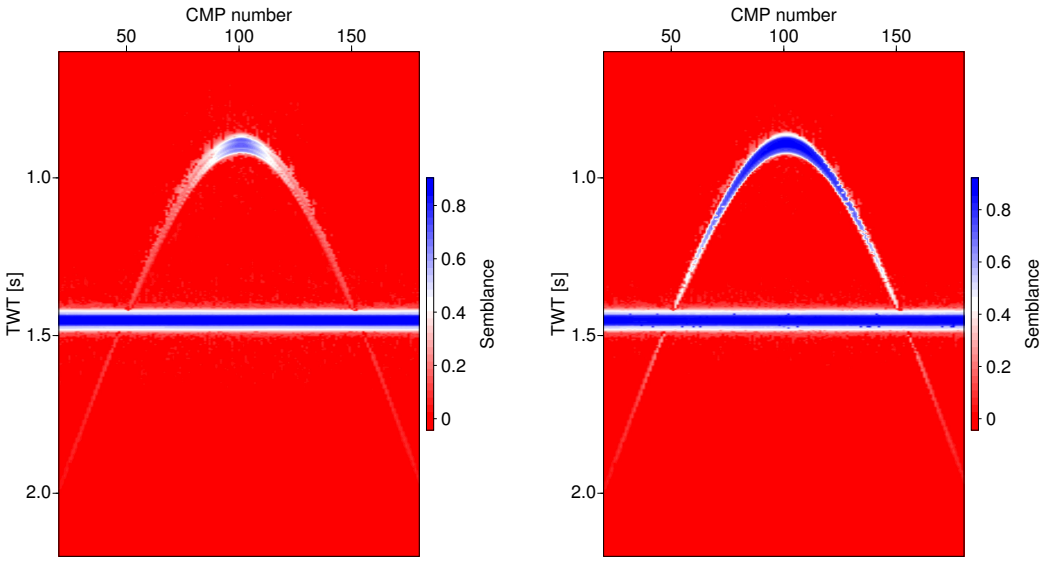

(a) (b)

Figure 3.7: Coherency section for a simple point diffractor and a planar reflector in a homogeneous medium obtained by (a) the conventional hyperbolic CRS and (b) the i-CRS operator. It is evident that the i-CRS operator gives considerably higher values of semblance especially in the case of the diffraction.

that the application of the i-CRS leads to considerably higher values of semblance and hence, has a better stacking result in terms of coherence and accuracy. I use i-CRS to partially stack the data along the diffraction travetimes in the proposed workflow.

3.2 Workflow for prestack diffraction separation

In order to combine the features of the diffraction weighting function with the partial i-CRS stack method, I suggest the following strategy to obtain diffraction-only data:

1. Determination of the CRS / i-CRS parameters (e.g., Mann, 2002; Müller, 2003; Vanelle et al., 2010; Schwarz et al., 2012).
2. Evaluation of the separation criterion (according to Equation 3.3) for every ZO sample with proper choice of the threshold based on the complexity of the subsurface.
3. Finding the related ZO time and i-CRS parameters for each sample in different offsets using the solution suggested by Baykulov and Gajewski (2009).
4. Execution of the partial i-CRS stack with an optimal aperture in both h and x_m directions.

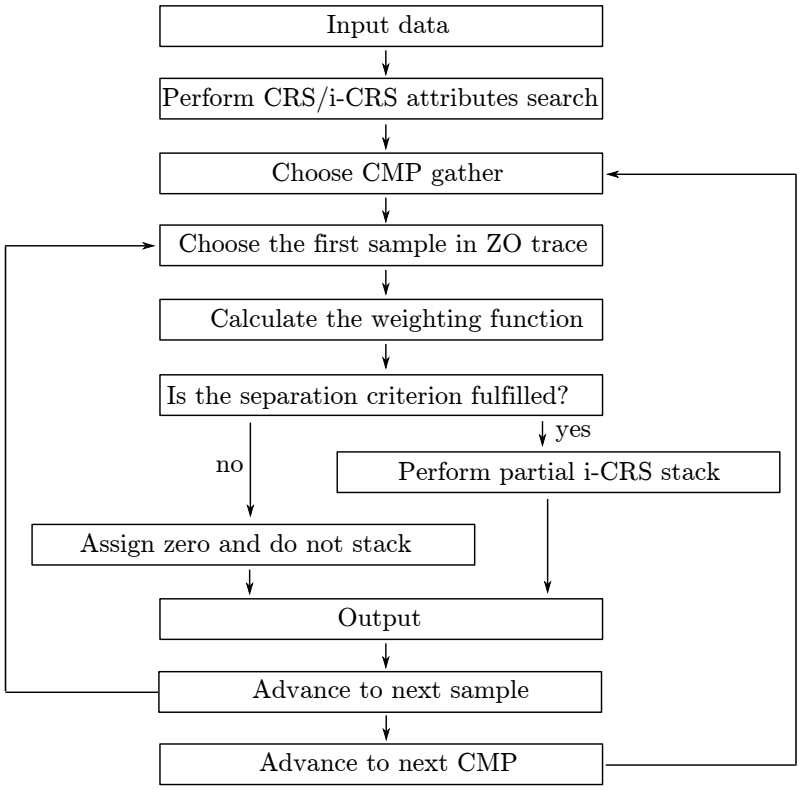

Figure 3.8: A flowchart which expresses the procedure of the 2D prestack diffraction separation.

Figure 3.8 shows the above workflow for prestack diffraction separation in a flowchart. After the determination of the wavefield attributes for each ZO sample, the partial i-CRS stack is implemented for the ZO samples which belong to diffracted events. Consequently, the prestack diffraction-only data are obtained which can have exciting applications, e.g., in time migration velocity model building, which is explained in the following.

3.2.1 Diffraction-based migration velocity analysis

Migration velocity analysis (also known as MVA) is based on the analysis of common image gathers (CIG) that represent migrated images obtained from different offsets Yilmaz (2001); Robein (2003). Migration with correct velocity produces CIGs with horizontally-aligned events, whereas velocity errors lead to visible differences between common-offset images. The stacking velocities are usually used as input for migration velocity model building. Residual move-out correction is subsequently required to correct the effect of the reflector dip in the CIGs (Robein, 2003).

However, diffractions can be used in migration velocity model building as well (see, e.g. Landa et al., 2008; Reshef and Landa, 2009). The MVA using diffracted events is

not a new concept. Harlan et al. (1984) addressed this problem and proposed methods to isolate diffraction events around faults. They quantified focusing using statistical tools and introduced the MVA techniques applicable to simple geology, e.g., constant velocity. Söllner and Yang (2002) used focusing of simulated diffractions using data-derived parameters to estimate interval velocities. Dell (2012) suggested a migration velocity scan routine applied to poststack diffraction-only data based on the semblance norm. In his method, the velocity is consistent with the data which gives the best focused diffraction.

I propose to use diffraction-only gathers to generate diffraction-only velocity spectra. It is assumed that only diffraction picks are present in these velocity spectra. Thus, they allow to build a time migration velocity model since stacking velocities are dip-independent after prestack diffraction separation. Therefore, these velocities can be directly used to migrate data. I use the semblance norm (Taner and Koehler, 1969) as the measure of coherency. The novelty of the proposed approach lies in the integration of two essential steps: diffraction separation and imaging using diffraction-only information.

In the following section, I demonstrate the potential and effectiveness of the CRS-based prestack diffraction separation by applying it to a synthetic data set of a salt model. Diffractions can help estimate more accurate velocities at the top of salt, particularly in the cases of rough salt bodies.

3.3 Application to the Sigsbee-2A data set

The first example concerns the Sigsbee-2A data set which represents a deepwater setting of the Sigsbee escarpment in the central Gulf of Mexico. The data was produced by SMAART JV. The key feature of the model is a large salt body with a very complex geometry. The data does not contain multiples. Some normal and thrust faults are present in the data. The Sigsbee model often serves as a benchmark model for migration algorithms. The topography of the top of salt is the cause of many strong diffractions and bowties. Two horizontal chains of diffractors are also located in the model that can be seen at about 5 and 7.5 km depth. An ideal migration algorithm should handle these problems and reduce the artifacts.

Figure 3.9 displays the general stratigraphy of the model along with the interval velocity distribution. The prestack data volume was simulated by means of a finite-difference (FD) approximation of the acoustic wave equation. The data set features almost 8 km of offset with a shot interval of 45 m and a receiver spacing of 23 m and a fold of 87. All acquisition parameters are given in Table 3.1. Noise with S/N ratio of 10 was added to the data.

Most of the CMPs ranging from 25 to 2069 are stacked by the CRS method. Firstly, the CRS attributes are found by the pragmatic search approach (see, e.g. Müller et al., 1998). If attributes are refined by means of the different type of optimization methods (see, e.g., Müller et al., 1998; Mann, 2002; Walda and Gajewski, 2015), diffraction separation is enhanced. However, in order to keep computational costs low and to speed up the process,

Acquisition geometry	
Number of shots	496
Shot interval	45.72 m
Minimum offset	0 m
Maximum offset	7932 m
Number of receivers	348
Maximum fold	87
CMP interval	11.43 m
CMP range	25-2069 m
Recording parameters	
Recording time	11 s
Sampling interval	8 ms
Frequency content	
Dominant frequency	20 Hz

Table 3.1: The Sigsbee-2A model: modeling parameters used for the generation of the data set.

the refined attributes were not used here.

I use a midpoint aperture of 300 m at the top and 500 m at the bottom. The offset aperture is 1000 m at the top and 4000 m at the bottom. ZO CRS attributes were then determined. The ZO stacked section is displayed in Figure 3.10. As expected, around the salt body a lot of diffraction patterns occur. Triplications, caused by synclines, are also present. Moreover, conflicting dips occur in the salt body. Above the salt an approximate horizontal layering of sediments can be seen. The left part without the salt body also shows a layering which is partially tilted.

The proposed method for prestack diffraction separation is then carried out on the data set. The threshold for diffraction separation is set to 0.9. Because of the complexity of the subsurface, the partial CRS stacking apertures in midpoint and offset directions were chosen as small as possible. Figures 3.11 and 3.12 display diffraction-only data as a result of post- and prestack diffraction separation, respectively. Through a comparison, it is apparent that the prestack diffraction separation leads to a better diffraction separation as well as data enhancement compared to the poststack method. The poststack separation is vulnerable to the presence of strong noise, whereas the prestack diffraction separation method exhibits good performance in the case of noisy data since it benefits from the data enhancement facility of the partial CRS stack (Bakhtiari Rad and Gajewski, 2015). The red arrows indicate some diffractions that were better separated using prestack diffraction separation.

In addition to the diffraction separation, prestack diffraction separation allows to generate prestack diffraction gathers. Four CMP positions of 250, 700, 1250, 1600 and their corresponding diffraction gathers from different structural features to investigate the potential of the new method are discussed here. Figure 3.13 displays the CMP gather 250

in the left part of the salt model before and after prestack diffraction separation. Since the diffractions in this region do not stem from the salt topography, they have low amplitudes and are masked by the stronger reflections and noise. In the respective diffraction-only gather, these weak diffractions have been well separated and the data is heavily enhanced. However, some residual reflection energy still is present.

Figure 3.14 displays the CMP gather 700 and the corresponding diffraction gather in the region where the strata and the salt body coincide. Again, the weak diffractions have been separated as well as the strong ones. Figure 3.15 displays CMP gather 1250, which is located at the top of the salt and above one of the steep flank of the salt dome. Some artifacts are still present, e.g., at 1000 m offset and 6 s , where conflicting dips can be recognized in the section prior to separation. In order to successfully apply the new workflow to such regions, conflicting dip processing is required, which is not considered in the context of this thesis because of its computational costs. Finally, Figure 3.16 displays the CMP position of 1600 above a diffraction stemming from the salt body. Again, the same results as before for diffraction separation as well as data enhancement are achieved.

3.3.1 Diffraction imaging of the Sigsbee-2A

As it was mentioned in the last section, an important application of the prestack diffraction separation is its interesting role in time migration velocity model building. I therefore take a closer look at the velocity spectra resulting from CRS stacking before and after diffraction separation for CMP locations 250, 700, 1250 and 1600 (Figure 3.17 to 3.20) to further evaluate the performance of the proposed method. Higher coherence values as well as better focusing can be achieved by considering diffraction-only data. As pointed out above, stacking velocities do not depend on the reflector dip after diffraction separation and therefore they can immediately be applied for time migration. Here, the diffraction-based time migration velocity model were built using automatic picking of high coherences for all CMPs.

Figure 3.21(a) displays the time-migrated section of the Sigsbee-2A using normal velocity analysis and, Figure 3.21(b) displays the time-migrated section of the diffraction-only data using diffraction velocities. I observe that the strong top-of-salt diffractions as well as weak diffractions from the non-salt part of the data are generally well-imaged, validating the correctness of the estimated time migration velocities. Moreover, no reflection is present and the data are enhanced. Red arrows indicate the events that were better imaged as a result of diffraction-based migration velocity analysis.

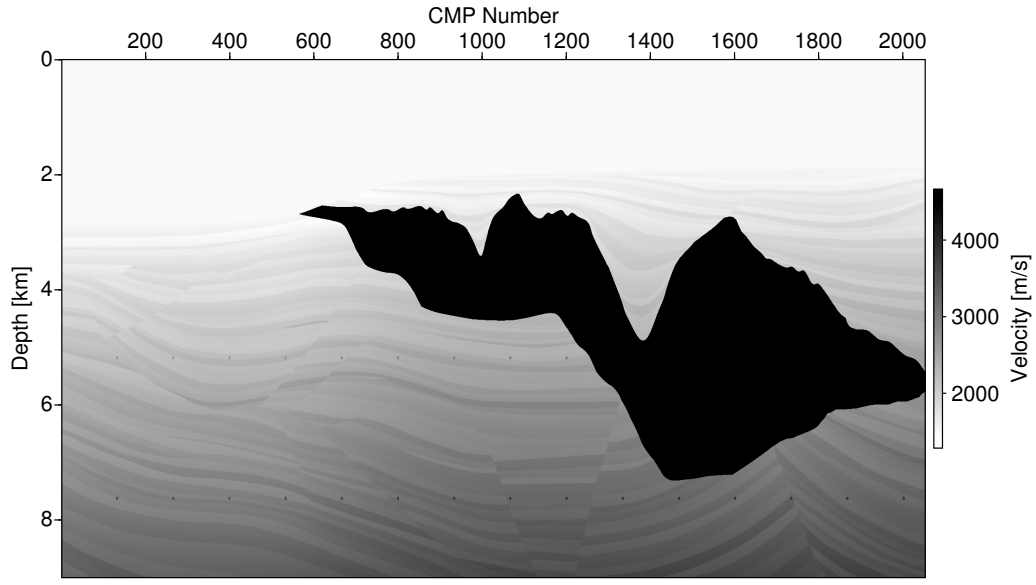

Figure 3.9: Sigsbee-2A velocity model. The model features a realistic geological complexity found at the Sigsbee escarpment in the gulf of Mexico. The complex geometry of the salt body generates numerous diffraction patterns and bow-tie structures.

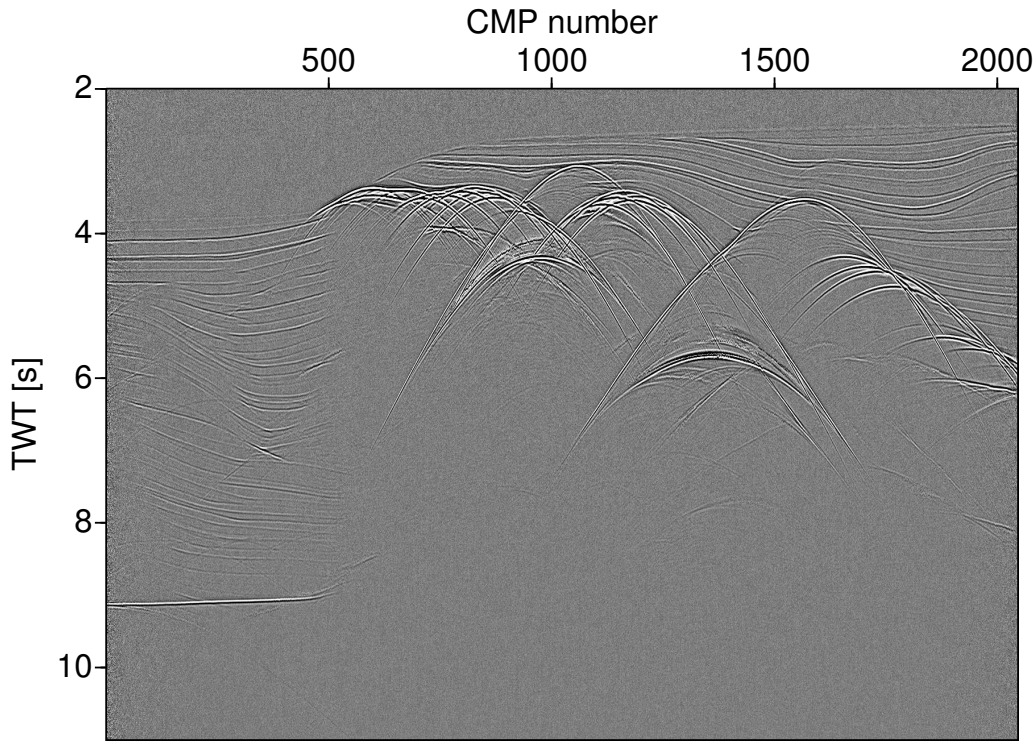

Figure 3.10: ZO stacked section of the Sigsbee-2A model.

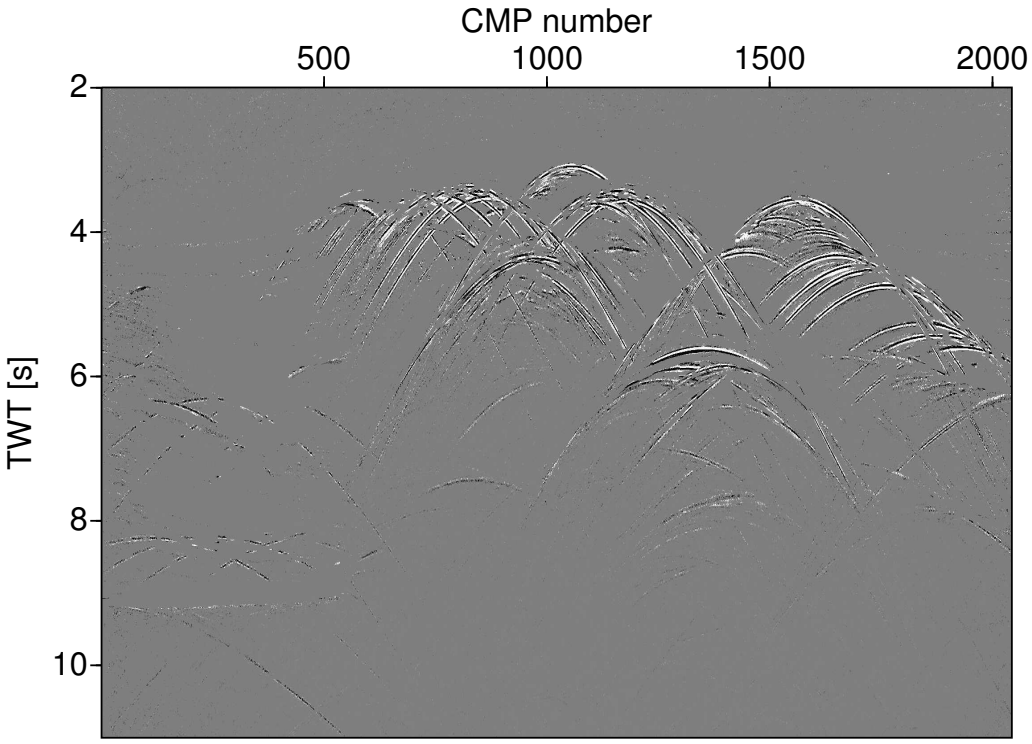

Figure 3.11: Sigsbee-2A model: the ZO diffraction-only section obtained via poststack diffraction separation.

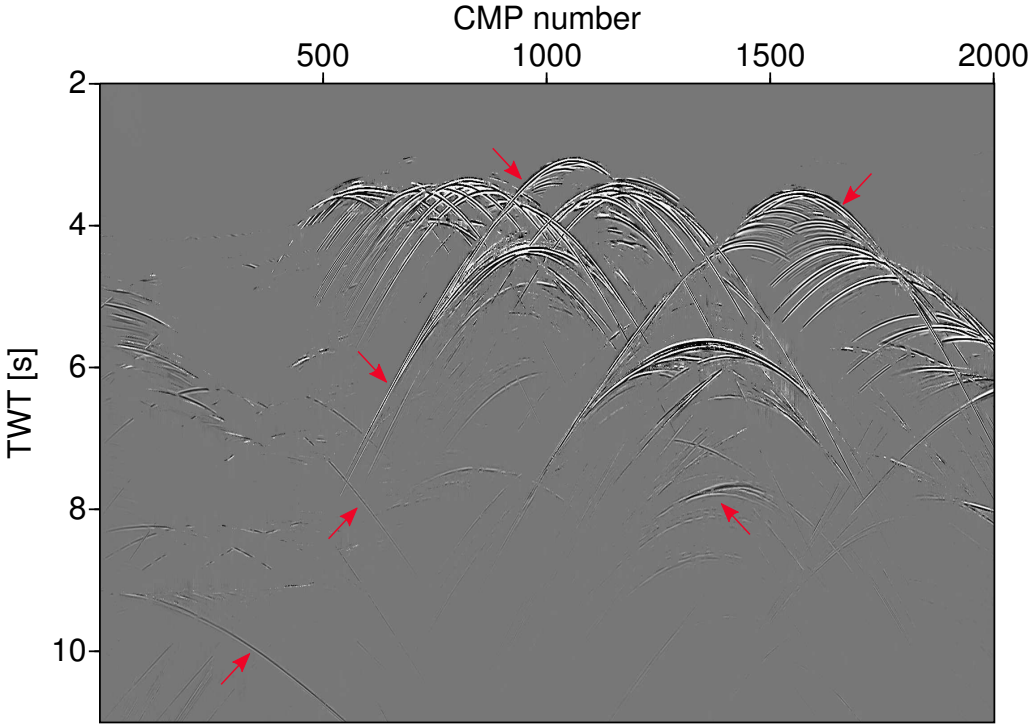

Figure 3.12: Sigsbee-2A model: the ZO diffraction-only section obtained via prestack diffraction separation. The red arrows indicate the diffractions that were better separated after prestack diffraction separation.

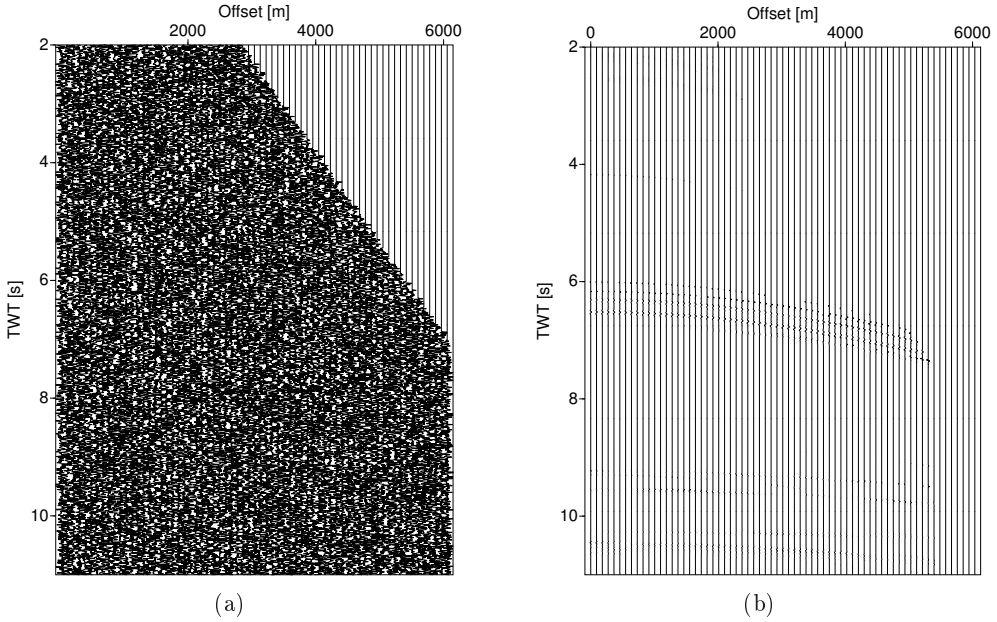

(a) (b)

Figure 3.13: CMP 250 of the Sigsbee-2A model: (a) before and (b) after prestack diffraction separation.

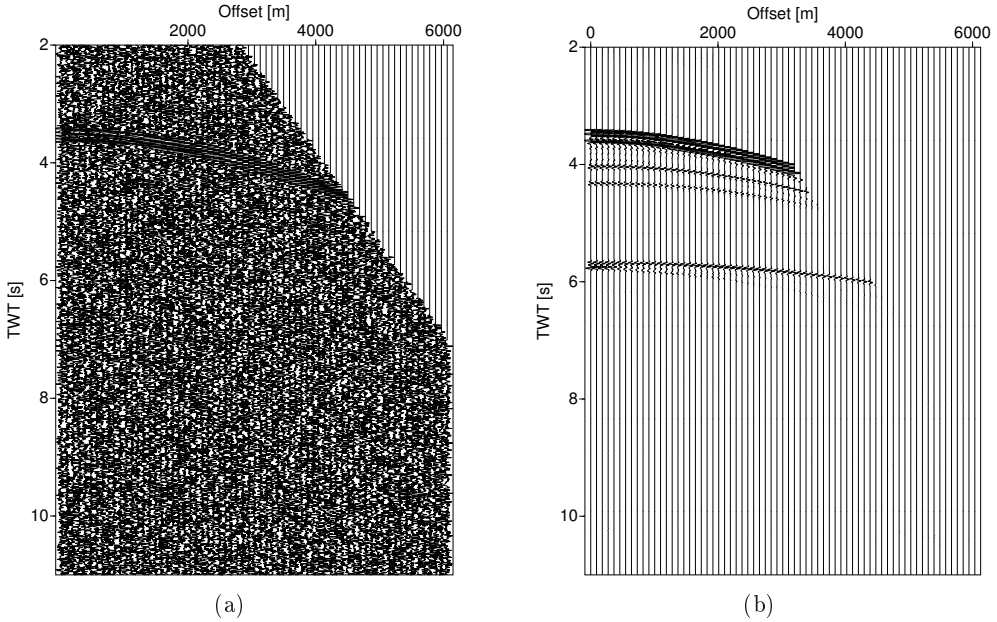

(a) (b)

Figure 3.14: CMP 700 of the Sigsbee-2A model: (a) before and (b) after prestack diffraction separation.

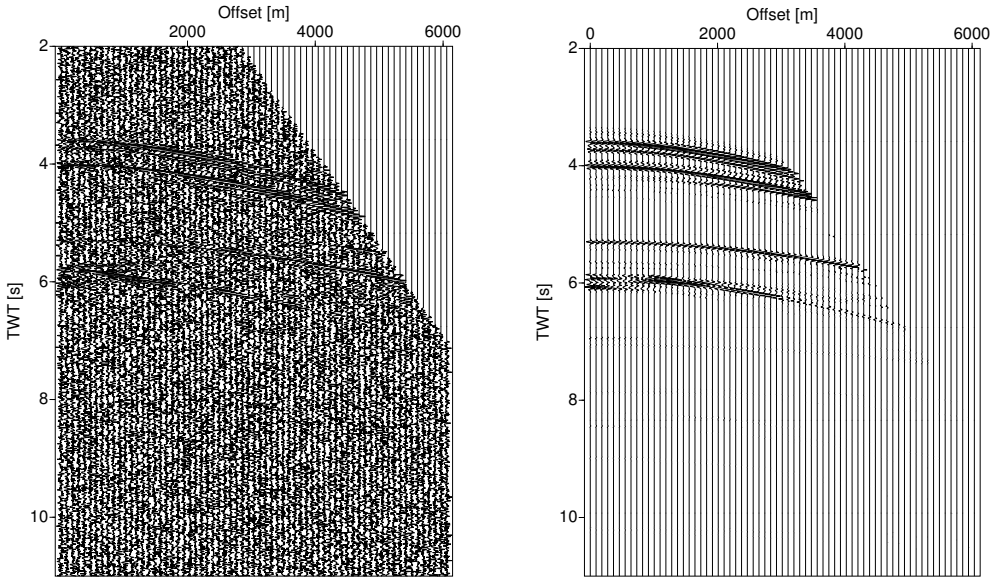

Figure 3.15: CMP 1250 of the Sigsbee-2A model: (a) before and (b) after prestack diffraction separation.

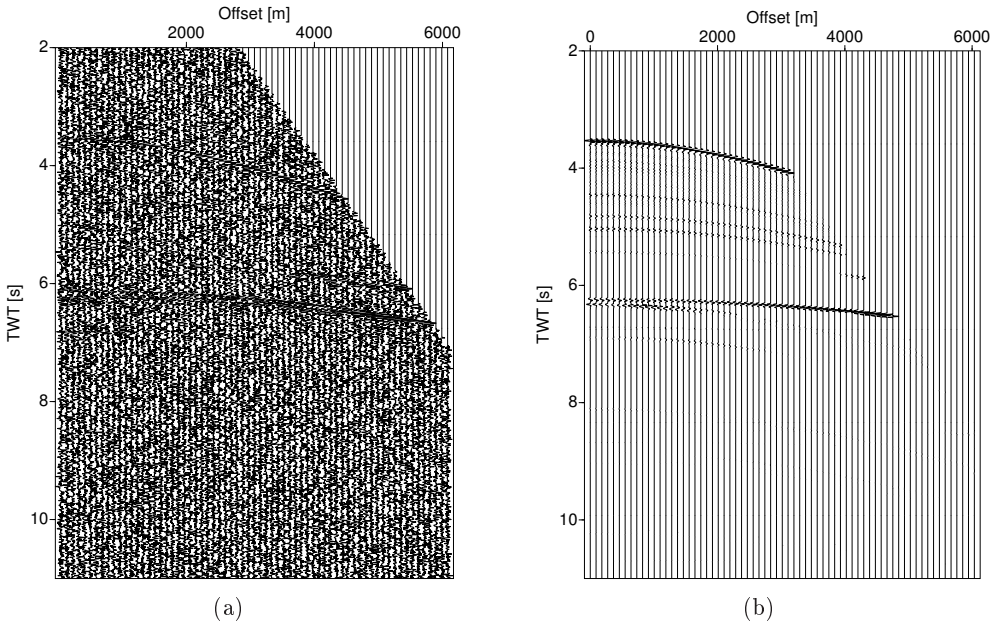

Figure 3.16: CMP 1600 of the Sigsbee-2A model: (a) before and (b) after prestack diffraction separation.

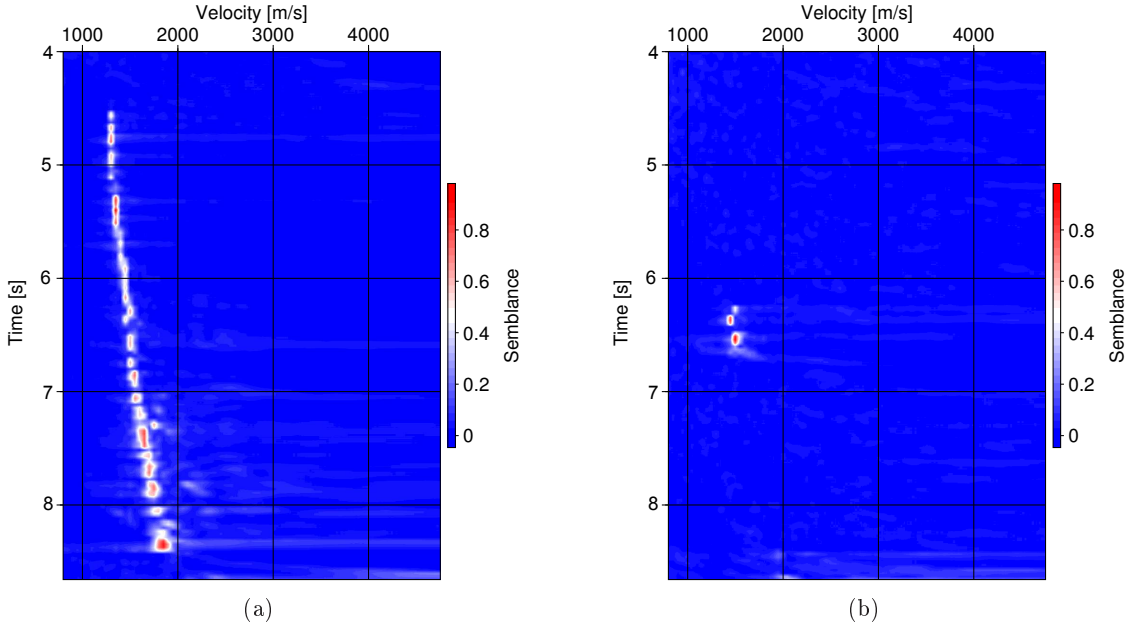

Figure 3.17: Sigsbee-2A model, the velocity spectra for CMP 250: (a) before and (b) after prestack diffraction separation.

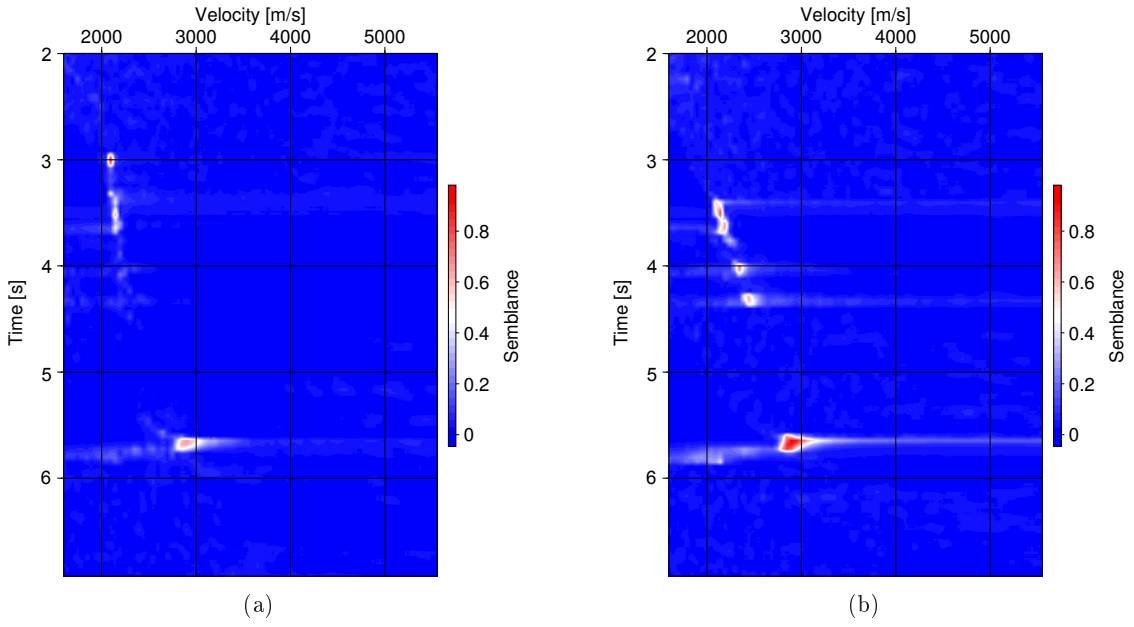

Figure 3.18: Sigsbee-2A model, the velocity spectra for CMP 700: (a) before and (b) after prestack diffraction separation.

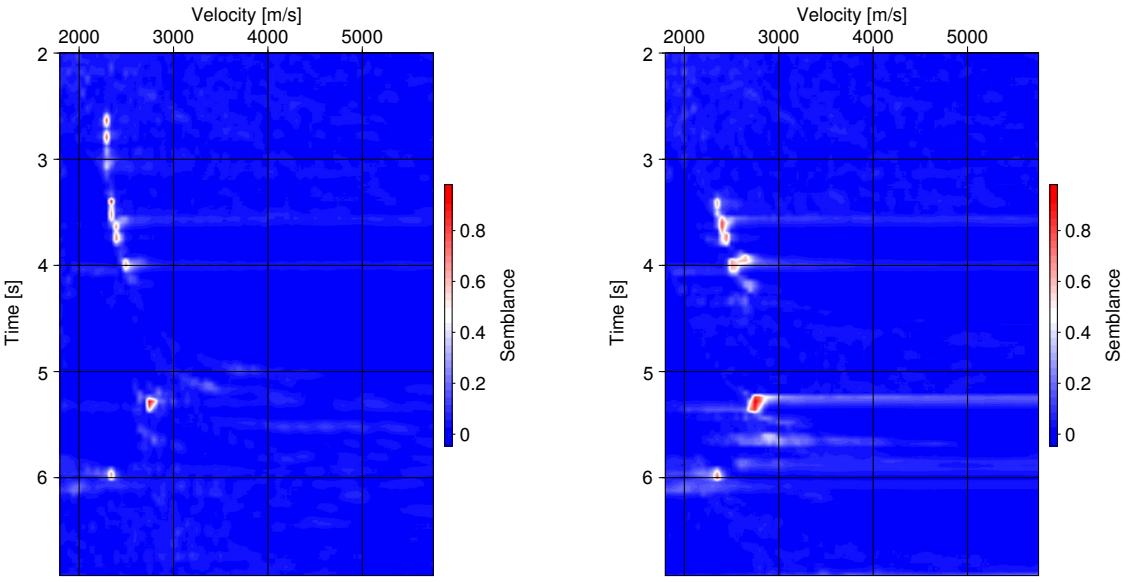

(a) (b)

Figure 3.19: Sigsbee-2A model, the velocity spectra for CMP 1250: (a) before and (b) after prestack diffraction separation.

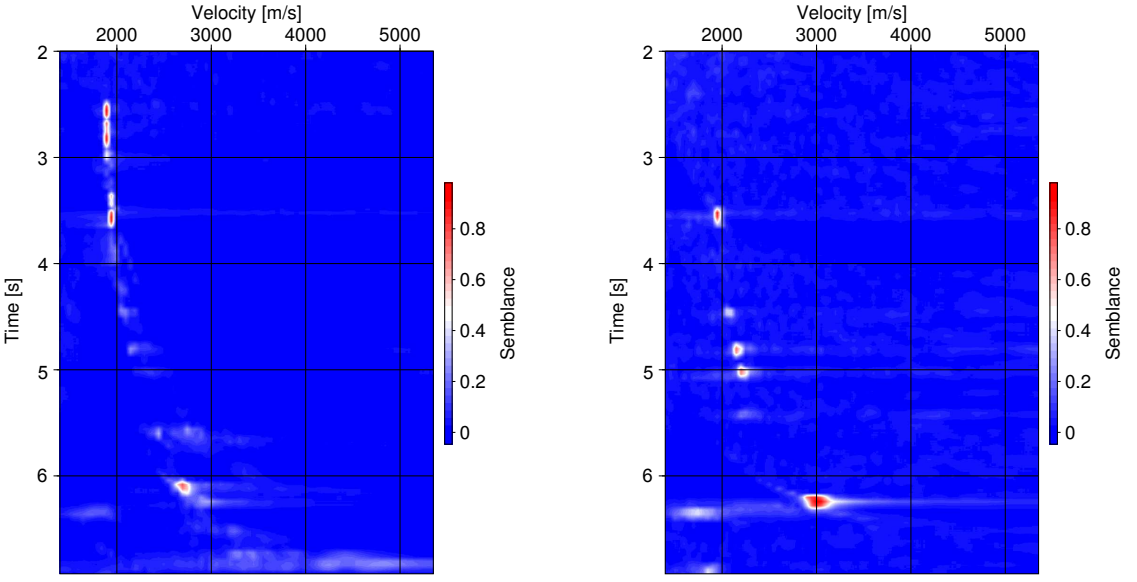

(a) (b)

Figure 3.20: Sigsbee-2A model, the velocity spectra for CMP 1600: (a) before and (b) after prestack diffraction separation.

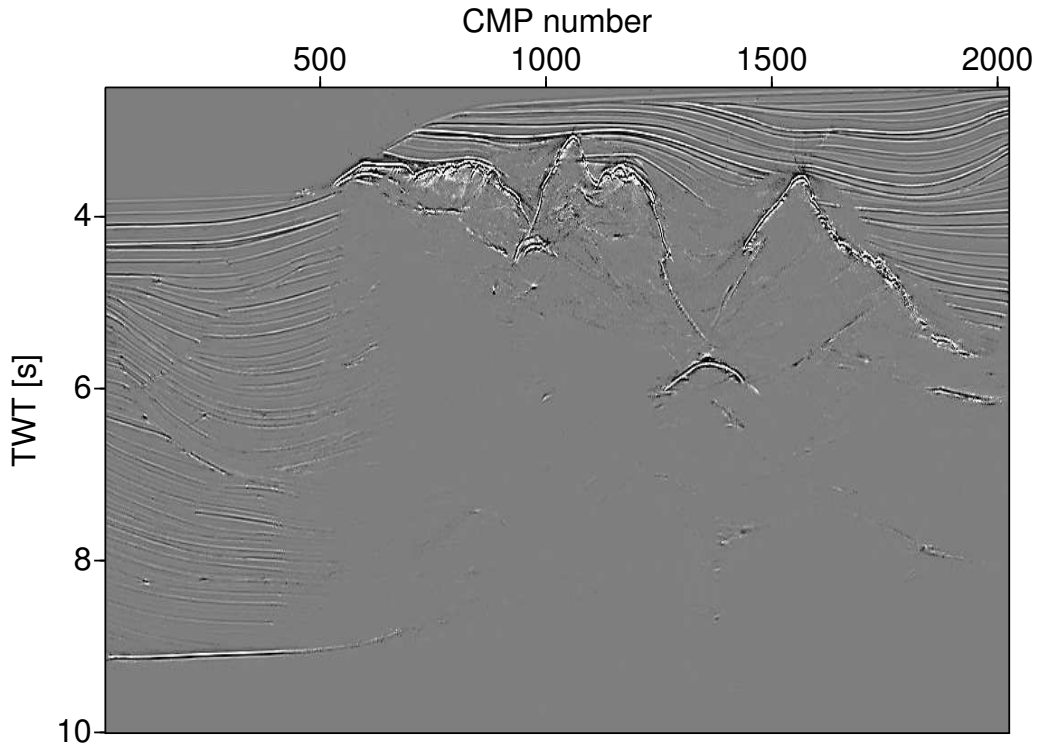

(a)

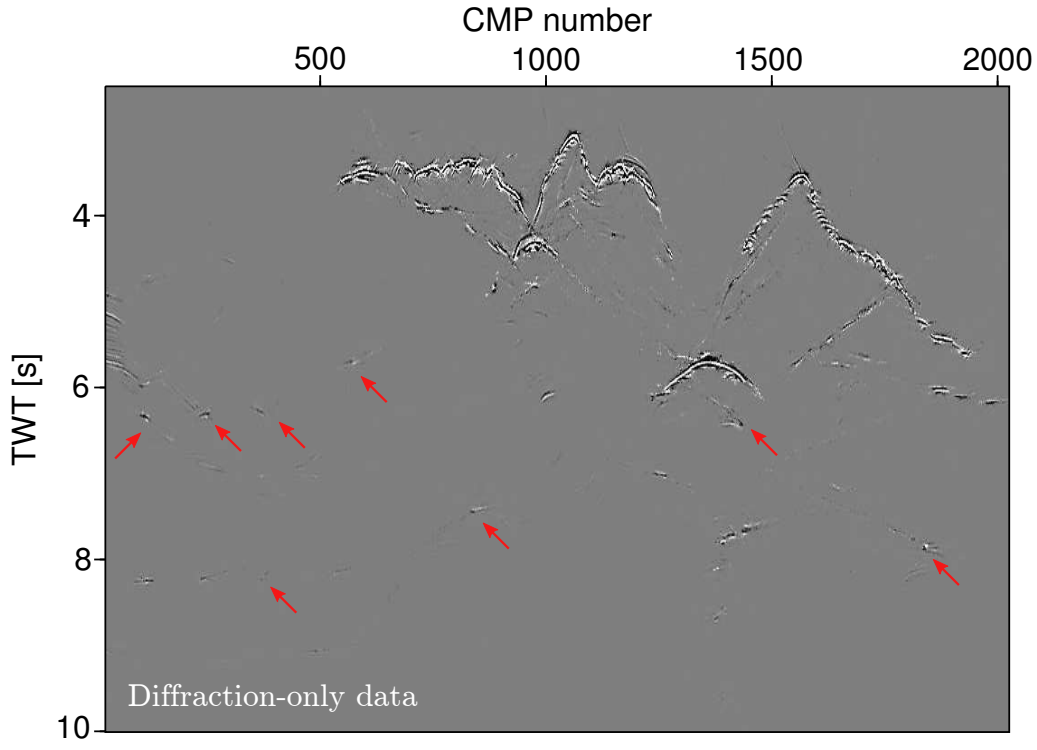

(b)

Figure 3.21: Sigsbee-2A model: the time-migrated section of (a) the whole data and (b) diffraction-only data. The red arrows indicate the events that were better imaged after prestack diffraction separation.

3.4 Application to field data

In order to further evaluate the performance of the new method, I choose a 2D marine field data from the central Levantine Basin located in the Eastern Mediterranean Sea. The data was provided by TGS-NOPEC. The line extends from the Israeli shelf towards the central part of the Levantine basin and the Eratosthenes Seamount. I processed a subset of the line (around 2500 CMPs) which represents roughly 30 km of the profile. Figure 3.22 shows the approximate position of the profile. The Levantine basin is located in the eastern Mediterranean Sea and is locally confined by the coast lines of Lebanon, Israel and Egypt to the east and south. To the north it is limited by Cyprus, whereas the Eratosthenes seamount together with the Herodotus basin mark the limit towards the west.

Netzeband et al. (2006) describe in detail the evolution of the salt complex in the Levantine basin. Figure 3.23 provides a structural overview of the seismic line. Above the salt, parallel pretectonic units are identifiable. They are separated from the divergent syntectonic units by a slump complex. The slide of the slump complex could be caused by over steepening or initial salt tectonics for example.

According to Netzeband et al. (2006), the deformation pattern of the intraevaporitic sequence includes folds and thrust faulting, which gives evidence for extensive salt tectonic and shortening during the depositional phase. Postdepositional gravity gliding caused salt rollers in the extensional marginal domain, compressional folds, and faults within the Levantine Basin. More details can be found in Netzeband et al. (2006). The high number of receivers results in a very high fold of 288. An overview of the acquisition parameters is given in the table 3.2.

I processed the data with the CRS method to obtain the wavefield attributes. The CMP

Acquisition geometry	
Number of shots	1077
Shot interval	45.72 m
Minimum offset	150 m
Maximum offset	7338 m
Number of receivers	576
Maximum fold	288
CMP interval	12.5 m
CMP range	2351-4793 m
Recording parameters	
Recording time	9.2 s
Sampling interval	2 ms
Frequency content	
Dominant frequency	20 Hz

Table 3.2: Acquisition parameters for the field data.

interval was 12.5 m with offsets between 150 and 7338 m. I use a midpoint aperture of 260m at the top and 1000 m at the bottom. The minimum and maximum offset apertures are 2000 m and 6000 m. The stacked section is shown in figure 3.24. As it is evident in the figure, the water depth increases from left to right. The sediments under the seafloor are layered partly divergent and partly horizontal. On the left, starting at 2.1 s, a reflector dips downward. Multiples are also present in the data and can be seen around 3 to 4 s especially in the right part of the section.

Diffractions are present mostly in the left part, from 2 to 3 s. These are caused by salt rollers. An approximately horizontal parallel layering occurs above the triangular structures on the right. The structure between the upper divergent layers and the lower parallel layers is not clear. Some diffraction hyperbolas are visible on the left but a chaotic pattern on the right is also visible. Because of the complex geological features of the area, out-of-plane diffractions are expected to be present especially mostly in the right part.

After the CRS attributes were determined, the pre- and poststack diffraction separation methods are applied to the data set. I chose 0.8 as the threshold for both separation scenarios. The results of the diffraction separation are shown in Figure 3.25. By comparison, I observe that the diffractions are better separated via prestack diffraction separation. The data are also enhanced and less residuals are present.

The diffraction separation in the right part is challenging since a lot of out-of-plane diffractions and multiples are present there. Some gaps and terminations present in the diffraction-only stacked section are due to the conflicting dips which are not handled in the proposed workflow since it is computationally very expensive. If conflicting dips are handled, diffraction separation exhibits significant improvements (see, e.g. Walda and Gajewski, 2015).

I chose four CMPs for a more detailed investigation. Figure 3.26 shows the results for CMP 2500 before and after diffraction separation. The strong diffractions, mostly around 2.3 s TWT, are caused by the rugged top of salt. A number of weaker diffractions is also present. Figure 3.27 shows CMP 2900 before and after prestack diffraction separation. Strong diffraction events can be recognized between 2.5 and 3 s TWT after the separation. The CMP gathers at positions 3200 and 3800 are displayed in Figures 3.28 and 3.29. Again, they exhibits the robustness of the proposed method to generate diffraction gathers. In all CMPs, the data are also enhanced.

As a final investigation of the field data, velocity spectra prior to and after diffraction separation are generated. Four examples are shown in Figures 3.30 to 3.33 for CMP locations 2500, 2900, 3200 and 3800 respectively. I recognize higher coherency maxima that are well-focused after the separation. The diffraction-only stacks lead to spectra that contain distinct maxima at higher times, which cannot be identified in the spectra prior to the separation.

3.4.1 Diffraction imaging of the field data

Diffraction imaging for this data is a challenge since only few strong diffractions are present mostly in the left part of the section, between 2 to 3 s. Moreover, the conflicting dips are heavily present almost everywhere. Diffraction imaging using the separated diffractions with high threshold leads to a poor result. Thus, I lowered the threshold value from 0.8 to 0.5, aiming to improve the subsequent diffraction imaging. In other words, diffractions by themselves are not capable to give a good imaging in this data. Therefore, the residual reflections present in data after diffraction separation can improve time imaging together with diffractions.

To evaluate the applicability of the proposed method for diffraction imaging, I used the results of the prestack time migration of the whole wavefield as a benchmark. Figure 3.34 displays the prestack time migrated section from the diffraction predominant part of the data, i.e. from CMP position 2500 to 3400 and from 2 to 3 s in time. The migration velocity model was obtained using the i-CRS attribute-based method suggested by Bobsin (2014). Note that the conflicting dips are handled in the benchmarked section based on a solution proposed by Walda and Gajewski (2015). Figure 3.35 displays the time migration results of the diffraction-only data using the diffraction velocities from the same area. The conflicting dips are not handled in this section. Comparing the results, I observed that diffractions from the top of salt are well-collapsed, validating the velocities. The red arrows indicate the events that were better imaged. However, as expected, residual reflections are present because of too low threshold.

3.4.2 General remarks

Diffraction-based imaging may fail and lead to blurred images in regions without enough diffractions. In addition, conflicting dips and out-of-plane diffractions due to the complex structures of the region may also deteriorate diffraction velocity model building and subsequent imaging. In the next chapter, I will extend the workflow to 3D in order to overcome the problem of out-of-plane diffractions.

Diffraction separation and imaging can be further improved by using better weighting function. Recently, a variety of new weighting function based on the CRS attributes for diffraction separation was suggested (see, e.g. Wissmath., 2016; Schwarz, 2015; Bakhtiari Rad et al., 2016). In the chapter 5, I will focus on different types of the diffraction weight and subsequently I propose a new diffraction weight based on the Fresnel zone which can be incorporated in the both pre- and poststack diffraction separation workflows.

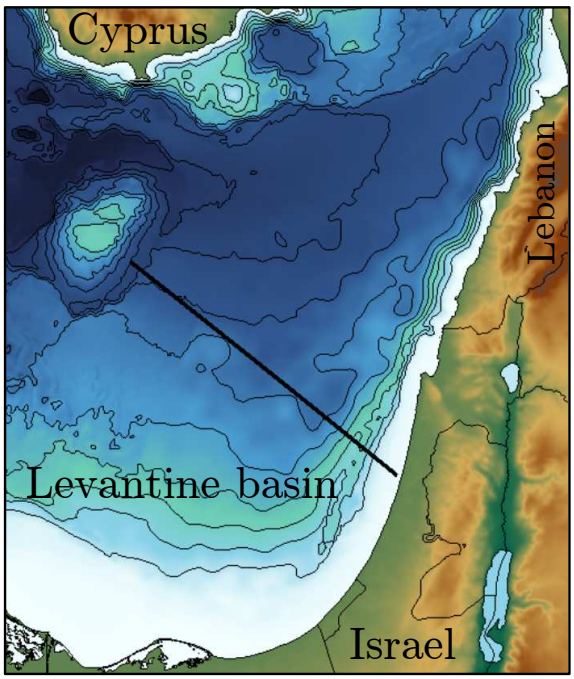

Figure 3.22: The field data: a map showing the eastern Mediterranean Sea (modified after Netzeband et al., 2006). The approximate location of the processed line is indicated by the black line.

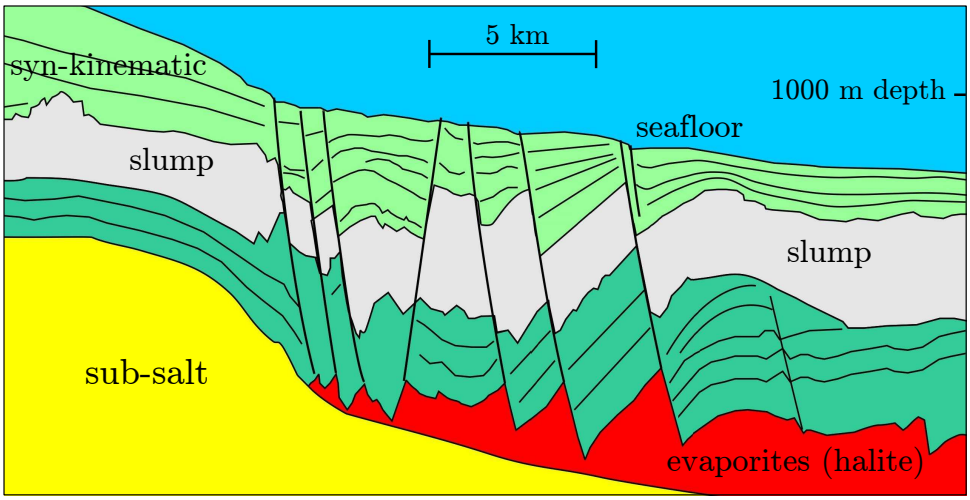

Figure 3.23: The field data: Salt tectonic in the Levantine basin (modified after Netzeband et al., 2006). Above the salt (red) parallel pretectonic units (dark green) are identifiable. They are separated from the divergent syntectonic units (bright green) by a slump complex (gray). Blue color indicates see water.

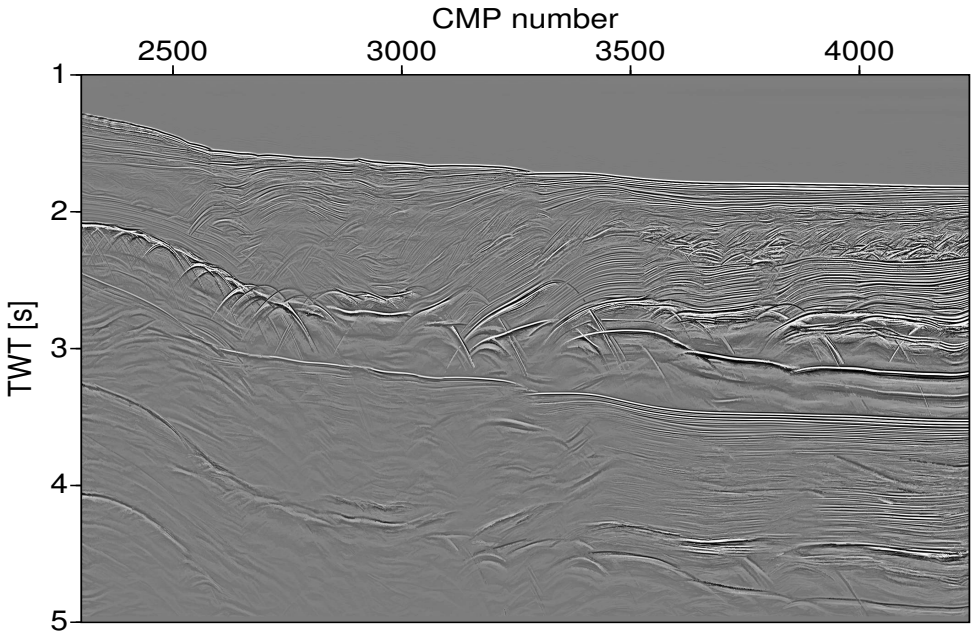

Figure 3.24: The ZO CRS stacked section of the field data.

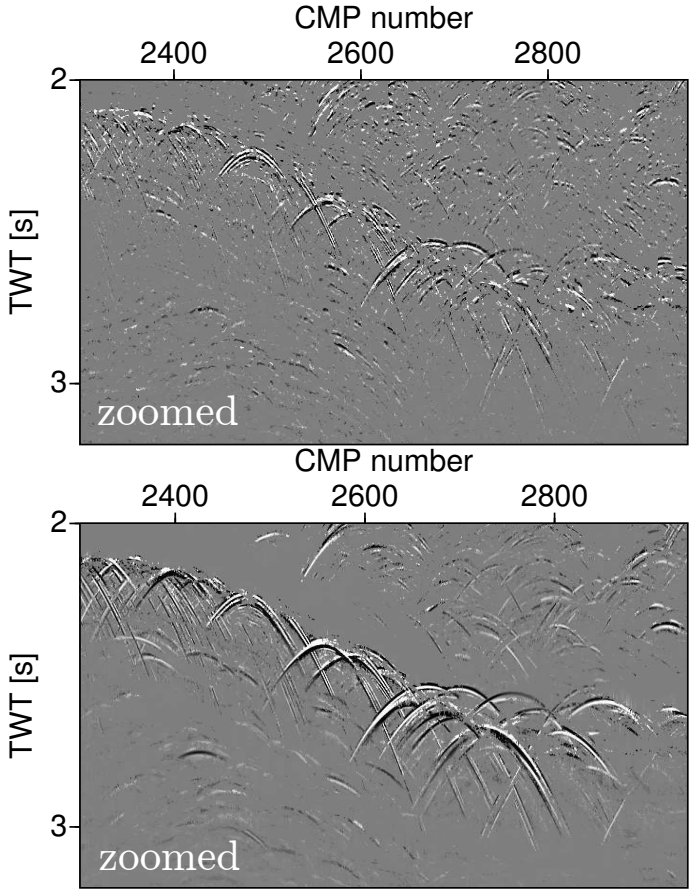

Figure 3.25: The field data: The ZO diffraction-only stacked section as a result of poststack diffraction separation (top) and the prestack approach (bottom).

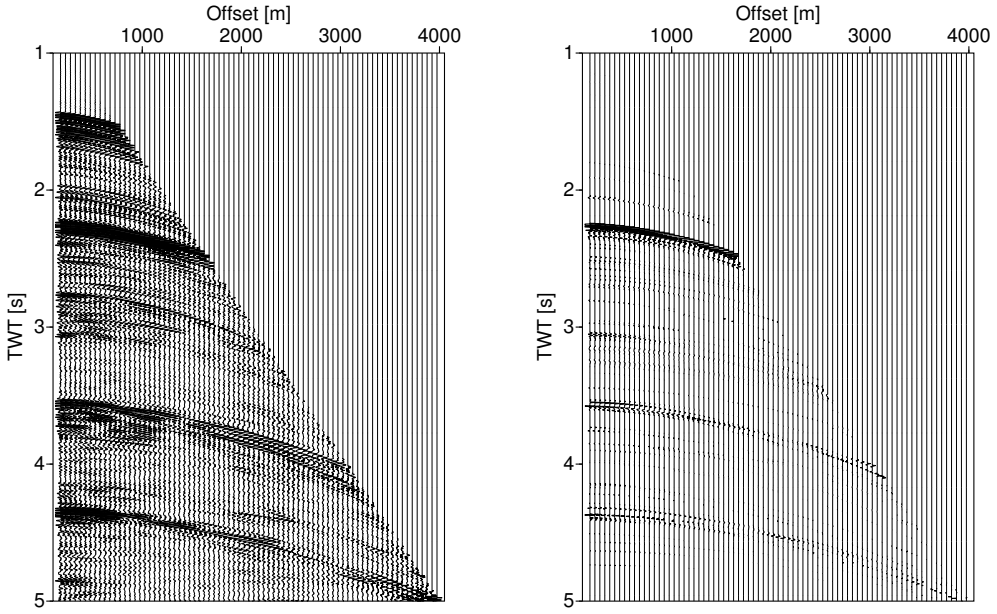

Figure 3.26: CMP location 2500 of the field data: (a) before and (b) after prestack diffraction separation.

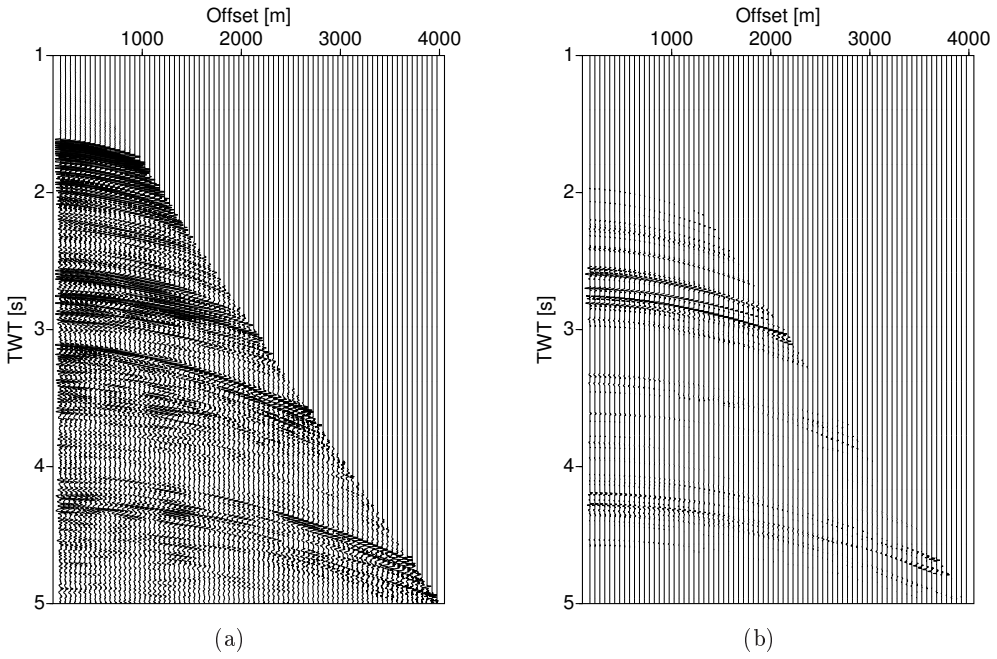

Figure 3.27: CMP location 2900 of the field data: (a) before and (b) after prestack diffraction separation.

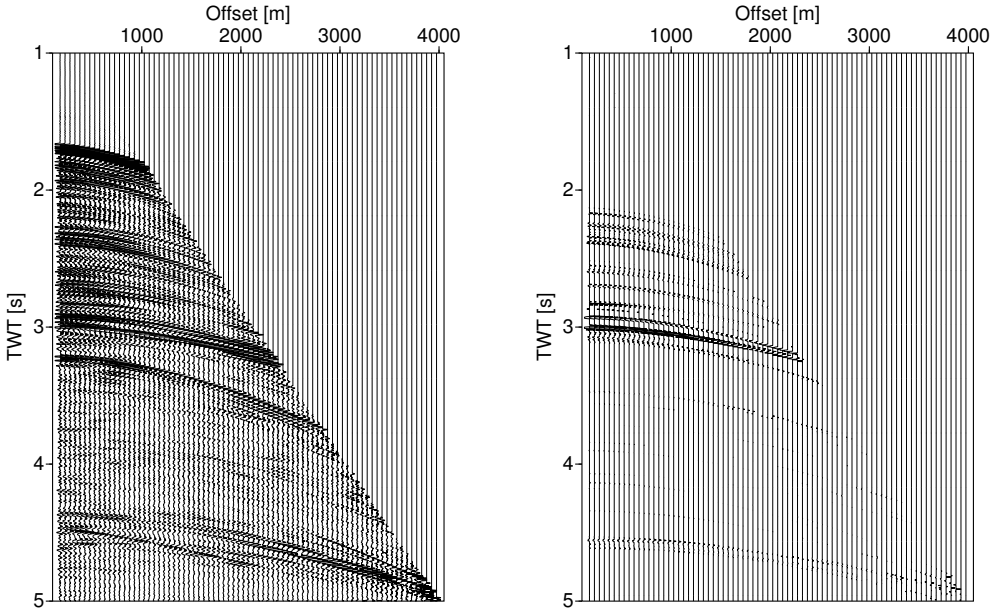

Figure 3.28: CMP location 3200 of the field data: (a) before and (b) after prestack diffraction separation

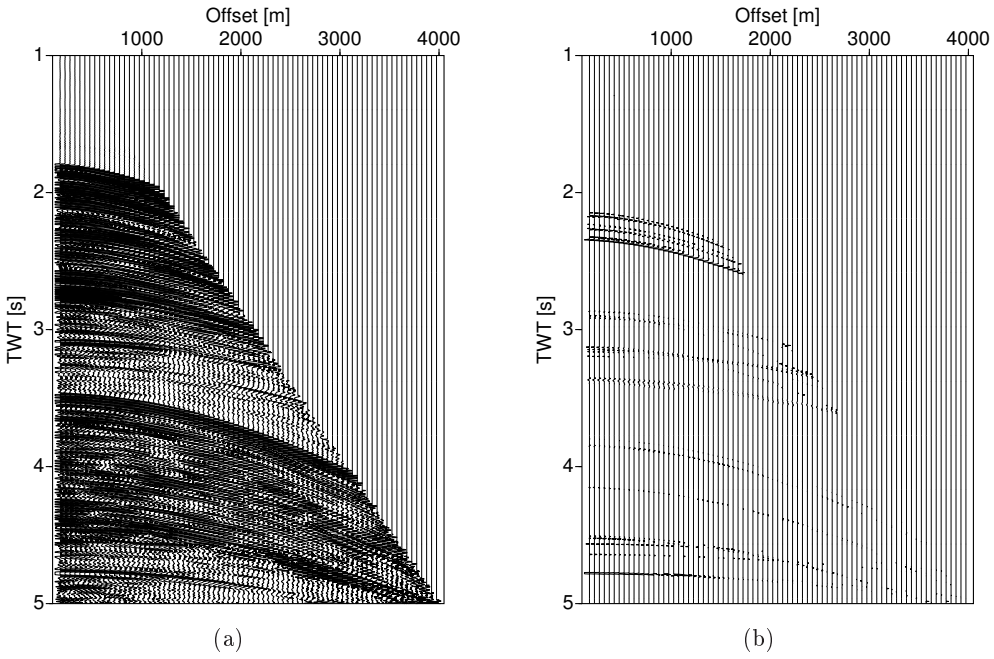

Figure 3.29: CMP 3800 of the field data: (a) before and (b) after prestack diffraction separation.

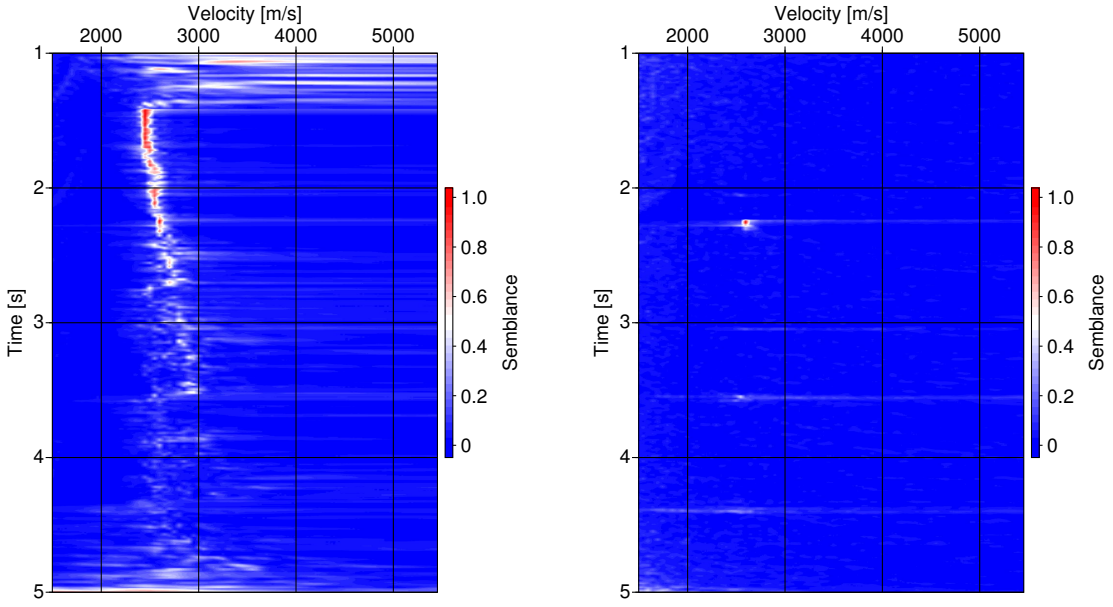

Figure 3.30: Velocity spectra for CMP location 2500 of the field data (a) before and, (b) after prestack diffraction separation.

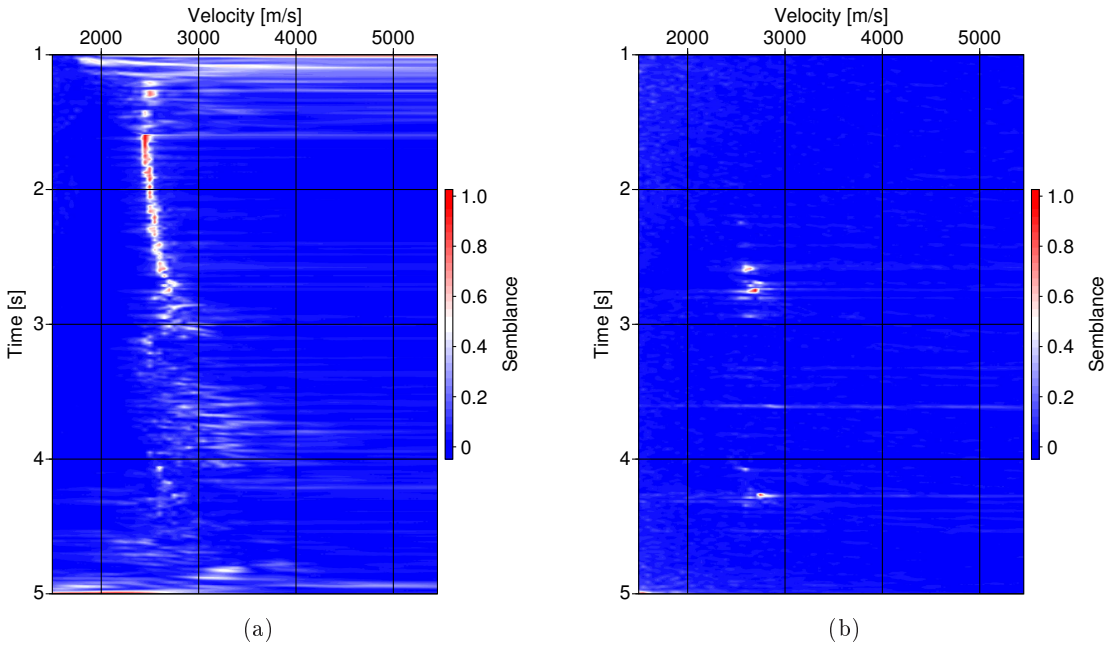

Figure 3.31: Velocity spectra for CMP location 2900 of the field data (a) before and, (b) after prestack diffraction separation.

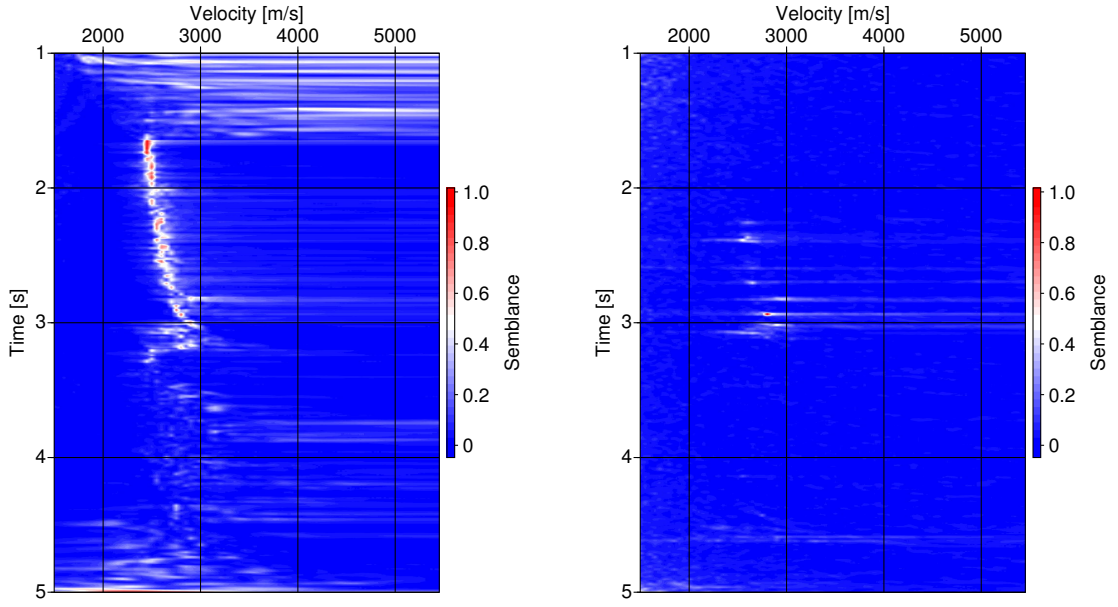

Figure 3.32: Velocity spectra for CMP location 3200 of the field data (a) before and, (b) after prestack diffraction separation.

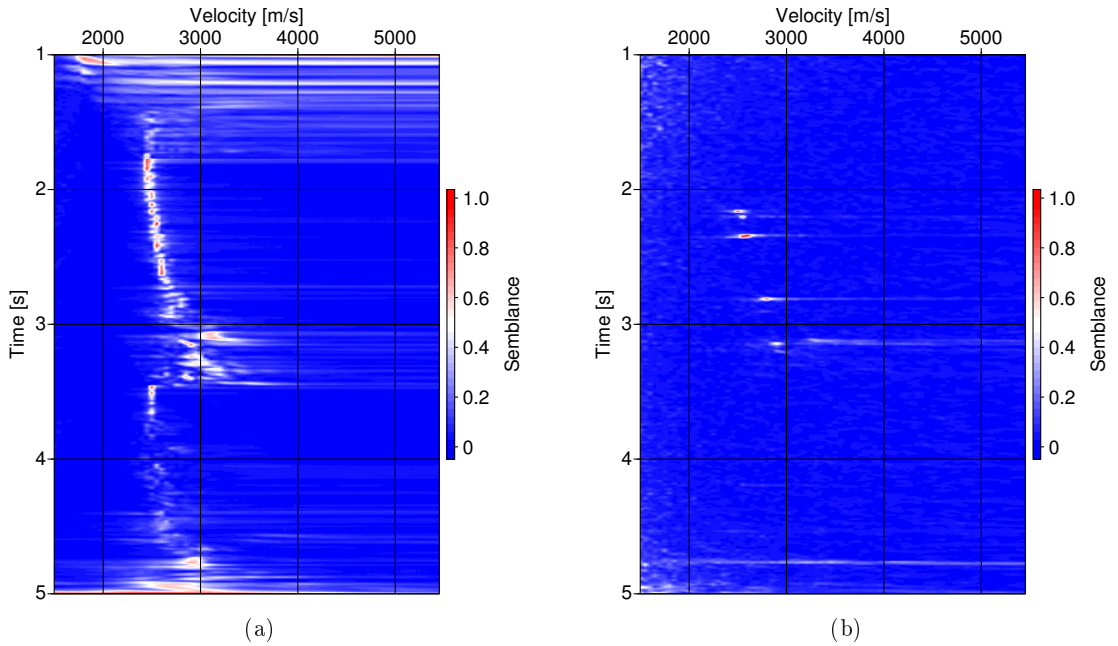

Figure 3.33: Velocity spectra for CMP location 3800 of the field data (a) before and, (b) after prestack diffraction separation.

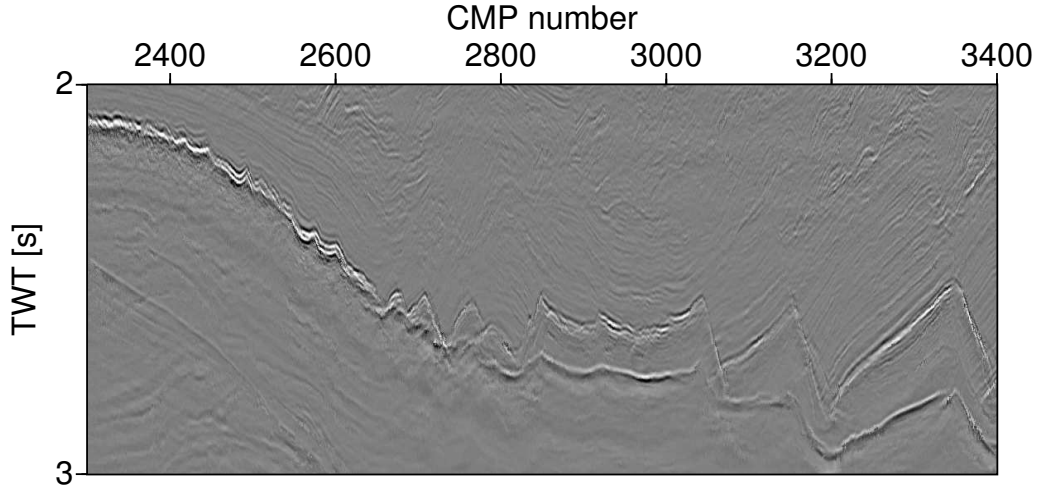

Figure 3.34: The field data: the time-migrated section of the whole data used as a benchmark.

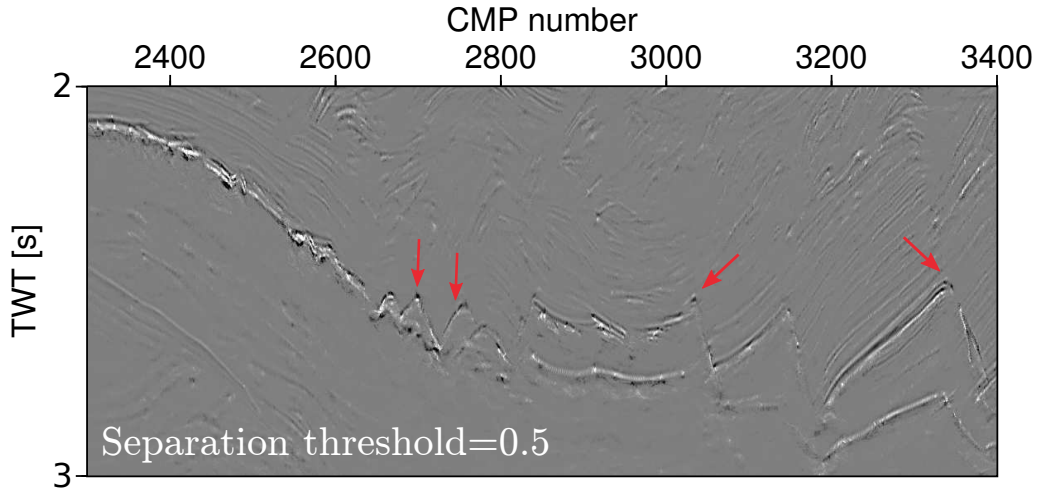

Figure 3.35: The field data: the time-migrated section of the diffraction-only data. The red arrows indicate the events that were better imaged using the proposed method.

Chapter 4

3D diffraction-based time imaging

2D imaging of complex geological features, e.g., salt bodies, irregular boundaries, fault plains which serve as the main sources of diffractions, are less accurate in contrast to the 3D techniques. As a general rule, out-of-plane events are imaged correctly only in 3D. Since a diffraction by itself is inherently a 3D phenomenon, 3D seismic methods are necessary for correct diffraction imaging. In this chapter, I discuss the possibility of the CRS-based diffraction separation in 3D. Afterwards, I extend the prestack diffraction separation workflow to 3D and in the final step, I perform time migration velocity analysis tuned to diffractions. The data examples comprise a simple synthetic data as well as a complex synthetic data set.

4.1 2D versus 3D seismic imaging

For a long time only 2D processing methods were applied to the seismic data. 2D data are acquired using sources and receivers laid out along a (more and less) straight line on the earth's surface. Most of 2D seismic imaging techniques assume that all signals are originated from the plane exactly under the profile. If this assumption is fulfilled, the 2D seismic image obtained after migration can represent a true section of the subsurface. However, in reality most of the seismic energy are reflected from different planes and thus, in-plane assumption of 2D seismic migration may lead to a distorted image of the surface and a subsequent misinterpretation. Moreover, 2D seismic images have been proven that they lack the detail obtained from the 3D methods (see, e.g. Yilmaz, 2001).

In recent years, 3D reflection seismic techniques have become powerful tools in the world of seismic exploration. Only 3D imaging can provide the detailed knowledge of reservoir features and handle out-of-plane reflections. The advent of 3D seismic has transformed the upstream oil industry because it enabled exploration in areas with complex structures lying below complex overburden. The imaging deficiencies of 2D seismic profiling were remedied

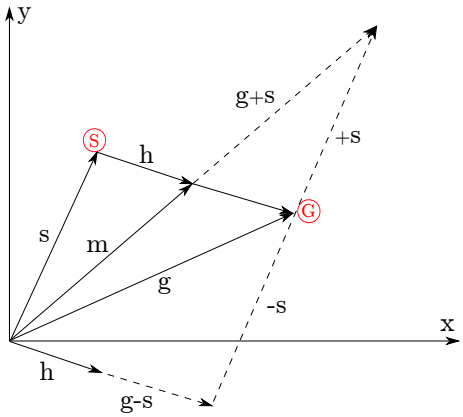

Figure 4.1: A topview of geometric relationships between the field coordinate vectors in the offset-midpoint coordinate vectors ($\Delta\mathbf{x}_m$ and $\mathbf{h}$). The circled S and G denote source and receiver, respectively.

by the implementation of 3D seismic data acquisition which allows data processing to migrate reflections to their correct image coordinates in 3D space. Data examples emphasizing the improvements of the final subsurface image due to the use of 3D seismic imaging are shown in, e.g., Yilmaz (2001) or Biondi (2004).

4.1.1 3D seismic geometry

A typical 3D seismic data acquisition is a grid of closely spaced seismic lines, crossing each other and provide densely sampled measurements of the subsurface reflectivity. Each seismic trace is characterized by the corresponding positions of the source and receiver. The coordinates of source and receiver are defined according to a preferably orthogonal coordinate system. The so-called in-line is a seismic line parallel to the x-axis direction in which the data is recorded. Lines which are perpendicular to in-lines are commonly referred to as cross-lines (or x-lines). If the properties of the subsurface do not change in the cross-line direction, all rays remain within the vertical observation plane defined by the acquisition line and the geometry shrinks into a 2D seismic survey for each y position.

In 3D, the midpoint and half-offset coordinates are vectors, whereas in 2D, they reduce to scalars. The azimuth is the angle between the vertical projection of a line of interest and true north. If the sources and receivers are aligned along one direction, as they are for marine surveys, it is assumed that the x-axis is aligned with this direction. In this case most of the offsets are distributed in a narrow range of azimuth.

Many of the basic concepts that have been developed for 2D seismic imaging are still valid for 3D imaging. Each seismic trace is again characterized by the corresponding positions of the source and receiver. 3D seismic prestack data is assumed to be a 5D hyper-volume of data including two offset in x- and y-axis of the global Cartesian coordinate system, and

two midpoints in x- and y-direction (see Figure 4.1) and the time axis.

4.1.2 3D CRS for point diffractions

According to the CRS theory, for a 3D diffracted event from a point diffractor, the matrices of wavefront curvature become identical, implying component-wise equality of the two. In this case, equation (2.17) can be simplified to (e.g. Müller, 2003; Bergler, 2004)

$$\begin{aligned} t_D^2(\Delta\mathbf{x}_m, \mathbf{h}) &= (t_0 + 2\mathbf{p}\Delta\mathbf{x}_m)^2 + 2\,t_0\left(\Delta\mathbf{x}_m^{\mathbf{T}}\mathbf{M}_{NIP}\Delta\mathbf{x}_m + \mathbf{h}^{\mathbf{T}}\mathbf{M}_{NIP}\mathbf{h}\right) \\ &= (t_0 + 2\mathbf{p}\Delta\mathbf{x}_m)^2 + 2\,t_0\left(\Delta\mathbf{x}_m + \mathbf{h}\right)^{\mathbf{T}}\mathbf{M}_{NIP}\left(\Delta\mathbf{x}_m + \mathbf{h}\right) \quad . \end{aligned}$$

This equation represents the 3D CRS-based diffraction stacking operator.

As mentioned in the previous chapter, for a point scatterer, the equality of the curvature matrices allows to identify the diffracted events and separate them from reflections. However, this equality condition is barely fulfilled in practice. Therefore, a weighting function as a filter for diffraction separation is required. I extended the 2D diffraction weight proposed by Dell and Gajewski (2011) to three dimensions without significant modifications:

$$W_D = \exp\left\{ -\sum_{i=0}^{1}\sum_{j=0}^{1}\left|\frac{K_N^{ij} - K_{NIP}^{ij}}{K_N^{ij} + K_{NIP}^{ij}}\right|\right\}, \tag{4.1}$$

where K_N^{ij} and K_{NIP}^{ij} are components of the corresponding matrices of the wavefront curvature. Again, like in the 2D case, if these components are close to each other, i.e., for point diffractions, the function W_D will be close to one. For reflections, the function value will be far from one. If the function W_D is above the threshold, the data are stacked and, if W_D is below, data are not stacked. The choice of the threshold depends on the complexity of the subsurface (Dell and Gajewski, 2011).

4.2 Edge diffraction separation

The sub-surface discontinuities can be categorized either as surfaces, edges, or isolated tips and points. For a smooth surface reflector, the planar surfaces generate specular (reflected) events, meaning that they strictly obey Snell's law (Keller, 1962). Events back-scattered from all other types of discontinuities are diffractions that do not obey Snell's law (see

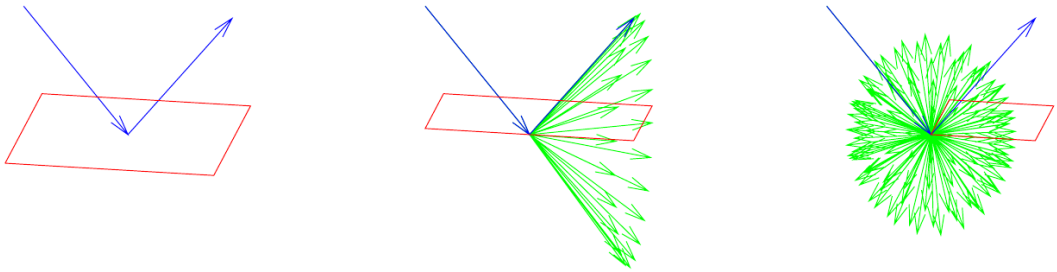

Figure 4.2: Surface reflection (left), edge diffraction (middle) and tip diffraction (right) (modified after Moser, 2011). The blue ray denotes the specular reflection and the green ray indicates diffraction. The diffraction due to a tip of a surface (or the end of an edge) does not follow Snell's law. The radiation pattern of edge diffractions depends on the azimuth of source and receivers line.

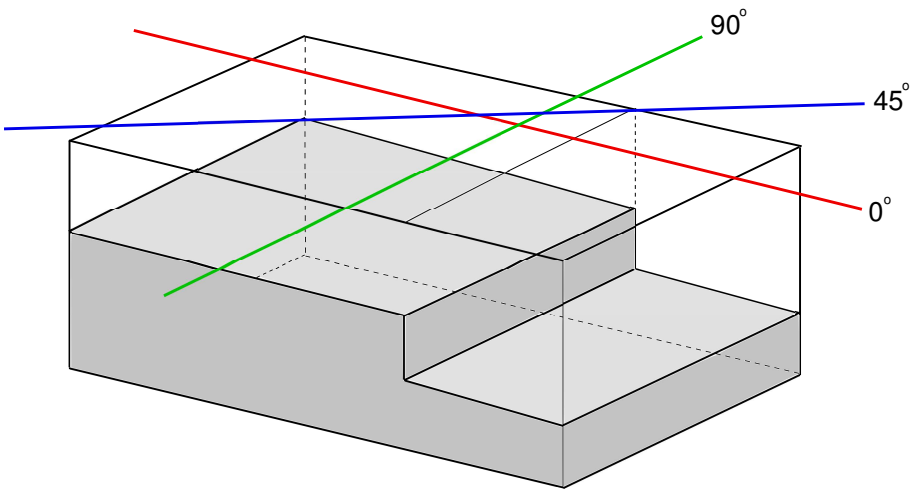

Figure 4.3: An edge model. The lines above indicate the CRS azimuthal attribute-search process in the 3D space. The green line is aligned with the strike of the edge, the red line is normal to it and, the blue line is in 45 degrees off the angle to the edge. In the case of edge diffraction separation using the CRS attributes, only if the strike of the edge diffractor is aligned to one of the CRS attribute-search azimuths (for instance, the green line here), the edge diffraction is separated.

Figure 4.2). However, edge diffractions in three dimensions appear as dipping events as they obey Snell's law only along the edge, but not transversely to it (Klem-Musatov et al., 2008).

Azimuth dependency of three dimensional edge diffractions is another challenge in diffraction imaging (see, e.g. Klokov et al., 2011). In 2D CRS, any type of diffraction can be separated using the CRS-based weighting function. In 3D, the classical strategy to find the wavefield attributes comprises 3-search in three azimuths to keep computational cost reasonable, i.e., individual search process along one in-line, one x-line and an extra line with 45 degrees of azimuth (see Müller, 2003; Bergler, 2004). Accordingly, the CRS-based diffraction weighting function can identify point diffractions best. However, in case of an edge diffractor, only if the strike is aligned to one of the CRS azimuthal search-lines, it is separated (note the green line in the Figure 4.3), however, in the other azimuths, the edge diffraction is partly separated and may lead to a smeared and less reliable image. Therefore, in most diffraction separation works, reflections are fully suppressed, edge diffractions are partly suppressed, while tip and point diffractions stand out unsuppressed.

4.3 3D time imaging tuned to diffractions

Time migration still serves as the first reliable tool for seismic imaging. It is fast and robust especially in the case of voluminous 3D data sets. However, time migration velocity determination in areas with steep dips faces challenges and requires several updates of stacking velocities in order to remove the effect of the dip.

If diffraction-only data are available, the resulting stacking velocities are dip-independent and thus do not need updates to remove the effect of the dip. Therefore, in the case of diffraction data, stacking velocities can immediately be used as time migration velocities. In order to combine the features of diffraction processing with the CRS method, I suggest the following strategy to obtain time-migration velocities tuned to diffraction-only data

1. Determination of the 3D CRS wavefield attributes by implementation of the code developed by Müller (2003); Dell (2012); Ahmed et al. (2015); Bakhtiari Rad et al. (2015b)

2. Evaluation of the separation criterion with proper choice of the separation threshold based on the complexity of the subsurface.

3. Finding the CRS attributes for each offset sample using a 3D extension of the solution suggested by Baykulov and Gajewski (2009).

4. Execution of a partial CRS stack (Baykulov and Gajewski, 2009) in 3D for diffractions with an optimal aperture in both $\mathbf{h}$ and $\Delta\mathbf{x}_m$ directions to generate diffraction-only gathers.

5. Automatic time migration velocity analysis (MVA) for each diffraction gather based on the semblance norm (Taner and Koehler, 1969).

6. Prestack time migration using velocities determined from diffraction-only data.

If there is a large number of diffraction in the data, they allow more accurate diffraction-based MVA. On the contrary, lack of enough diffractions or a poor diffraction separation deteriorates migration velocity model building, leading to smear the final image.

To evaluate the performance of the workflow, data examples including a simple and complex data are shown in the following. In order to keep the computational costs low, the non-point diffractions as well as conflicting dips are not handled in the proposed workflow.

4.4 Simple synthetic data example

I start the data example with a 3D simple synthetic model consisting of three homogeneous layers and a sphere with diameter of 100 m (see Figure 4.4). The velocity in the first layer is 1500 m/s, in the second layer is 1700 m/s, 1800 m/s in the third layer and in the sphere, velocity is 3000 m/s. The shot and receiver intervals are 25 m and the fold is 80. The offset range is 25 to 2000 m. The dominant frequency of the Ricker-wavelet is 20 Hz. Noise with S/N ratio of 5 was added to the data. Figure 4.5 displays the 3D CRS stacked section of the data for the 9 selected in-lines with the interval of 100 m. Note that the Norsar 3D raytracer software which is used in this experiment considers only high-curved reflectors as sources of diffractions even though the condition, $R \ll \lambda$, is not fulfilled. However, since the generated diffraction event still follows the diffraction traveltime and the CRS-based separation criterion ($R_N \approx R_{NIP}$) is valid for this event, I decided to use the data set for diffraction separation studies presented in the following.

4.4.1 Pre- and poststack diffraction separation results

The tasks of pre- and poststack diffraction separation are then carried out to generate diffraction-only data. Figures 4.6(a) and 4.6(b) display the ZO diffraction only data obtained via the post- and prestack diffraction separation methods, respectively. I used 0.85 as the threshold in both cases. Although the reflections are attenuated very well using both methods, the prestack method demonstrates advantages over the poststack separation. The diffraction-only data obtained via the proposed workflow exhibits higher S/N ratio because of the data enhancement facility of the partial CRS stacking method. Nevertheless, some artifacts are still present in both sections (e.g., at about 0.7 s) which are due to boundary effects as a result of the limited operator size at the end of the reflector boundary (Hertweck et al., 2003). The modeling parameters are given in Table 4.1.

In another attempt to evaluate the performance of the new workflow, I take a closer

Acquisition geometry	
Shot interval	25 m
Receiver interval	25 m
Minimum offset	25 m
Maximum offset	2000 m
Number of receivers	348
Maximum fold	80
Bin size	50× 25 m^2
Recording parameters	
Recording time	2 s
Sampling interval	4 ms
Frequency content	
Dominant frequency	20 Hz

Table 4.1: Parameters used for the generation of 3D simple synthetic data set.

look to an individual CMP gather before and after the prestack diffraction separation. Figure 4.7(a) displays the CMP gather #40 of the in-line #4 before prestack diffraction separation. To evaluate the robustness of the proposed workflow in diffraction separation and data regularization, I simulated a sparse data set with a 250 m gap in offset and 100 m in midpoint direction. The diffraction event at about 1.1 s is masked by noise. Figure 4.7(b) displays the same CMP after prestack diffraction separation. One can observe that, after applying prestack diffraction separation not only the diffraction event is separated well but the data is enhanced and the gap is filled, implying that the three tasks of wavefield separation, data enhancement and interpolation can be carried out simultaneously in one step (see, e.g. Bakhtiari Rad et al., 2015b,a).

4.4.2 Diffraction imaging results

In the next step, I perform time migration of the prestack diffraction-only data using diffraction velocities, i.e., the MVA applied here is tuned only to diffractions. I use the semblance norm as a measure of coherency. In addition to data enhancement, the prestack diffraction separation turns out to be advantageous in the 3D velocity model building. As it is shown in Figure 4.8, higher coherence values as well as better focusing is achieved via the new workflow. As I described before, diffraction velocities can immediately be applied for time migration since stacking velocities after prestack diffraction separation are dip-independent.

Figure 4.9 displays the time-migrated image of the diffraction-only data. The diffraction is well-focused, validating the correctness of the estimated time migration velocities. However, due to aforementioned aperture effect on boundaries, the migration operator does not sum up all the data necessary for complete destructive interference. As a result, migration artifacts appear, resulting in a smeared image (e.g., at around 0.7 s).

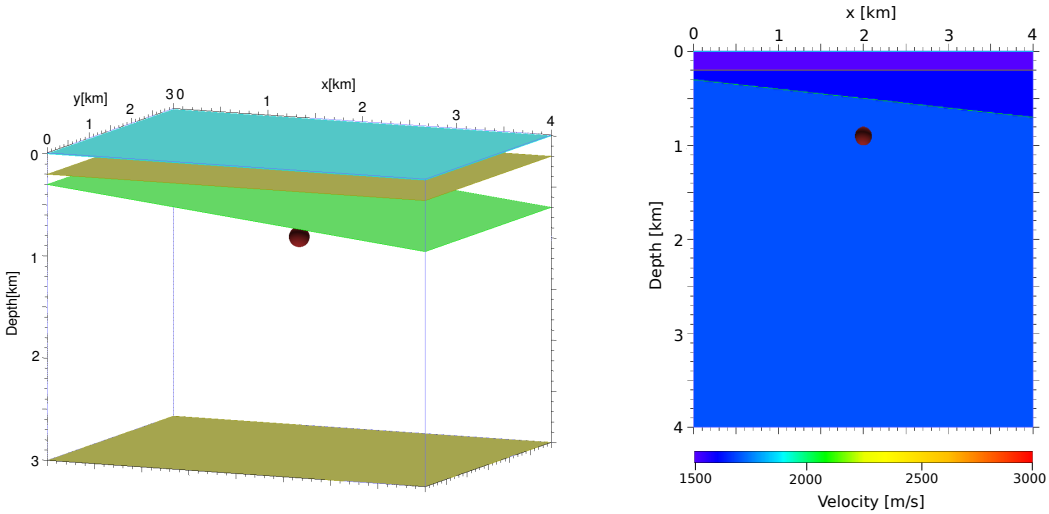

(a) (b)

Figure 4.4: (a) The 3D simple model consisting of three layers and a point scatterer which is distinguished by the red. (b) The cross-section of the velocity distribution in the model.

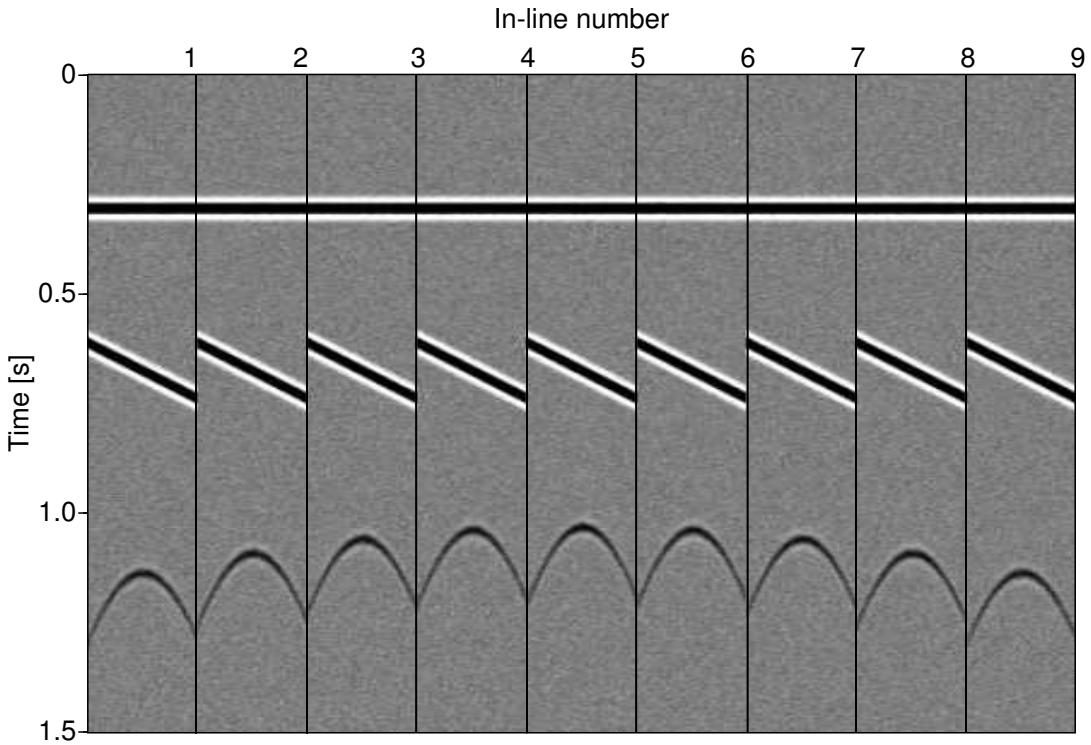

Figure 4.5: The 3D simple data: the CRS stacked section. A horizontal reflection, a dipping reflection and a diffraction are present from top to bottom. Note the amplitudes were clipped for better visualization.

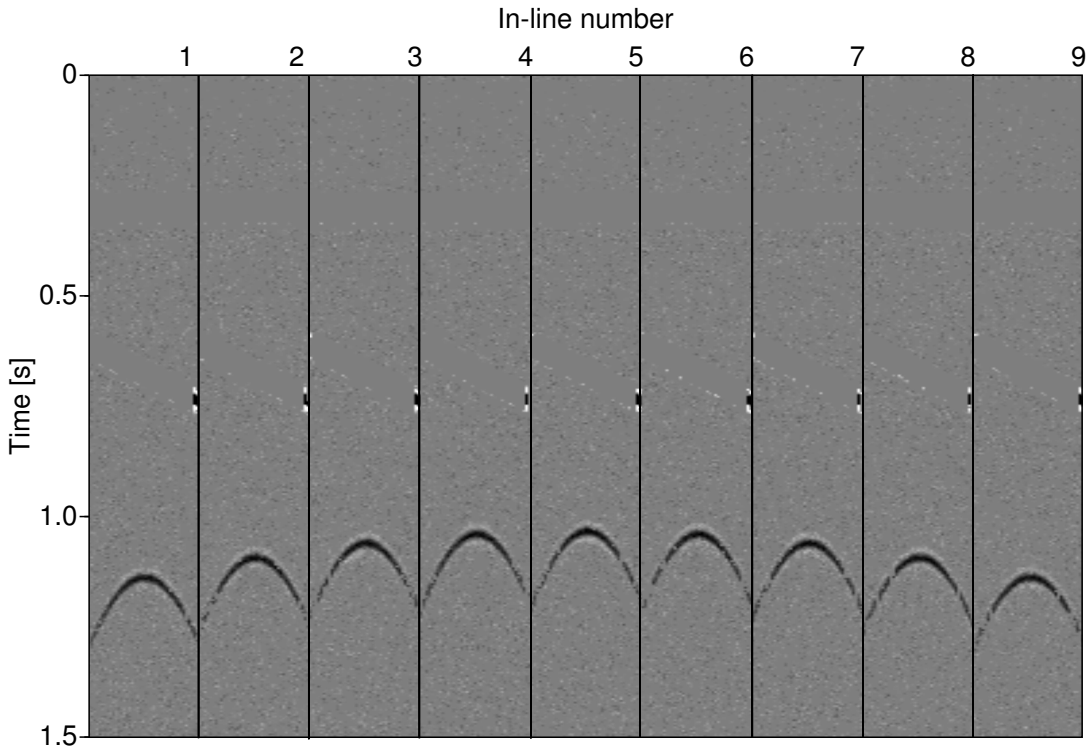

(a)

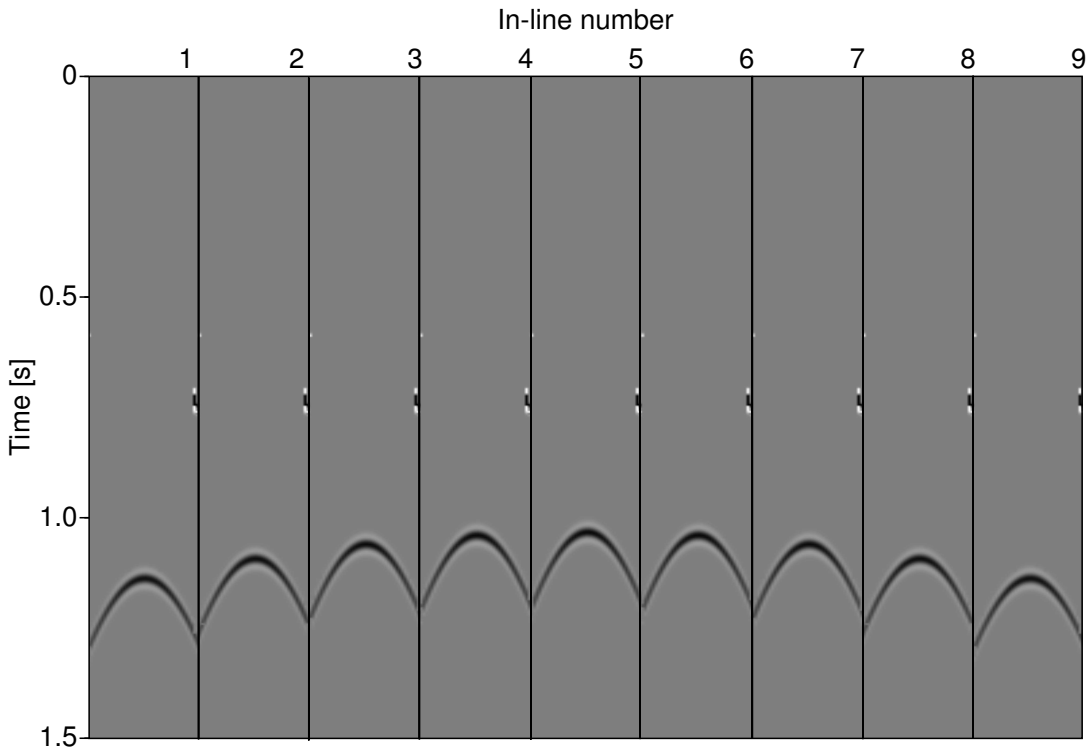

(b)

Figure 4.6: The 3D simple model: (a) diffraction-only data as a result of (a) post- and (b) prestack diffraction separation. Note the same clip in both sections.

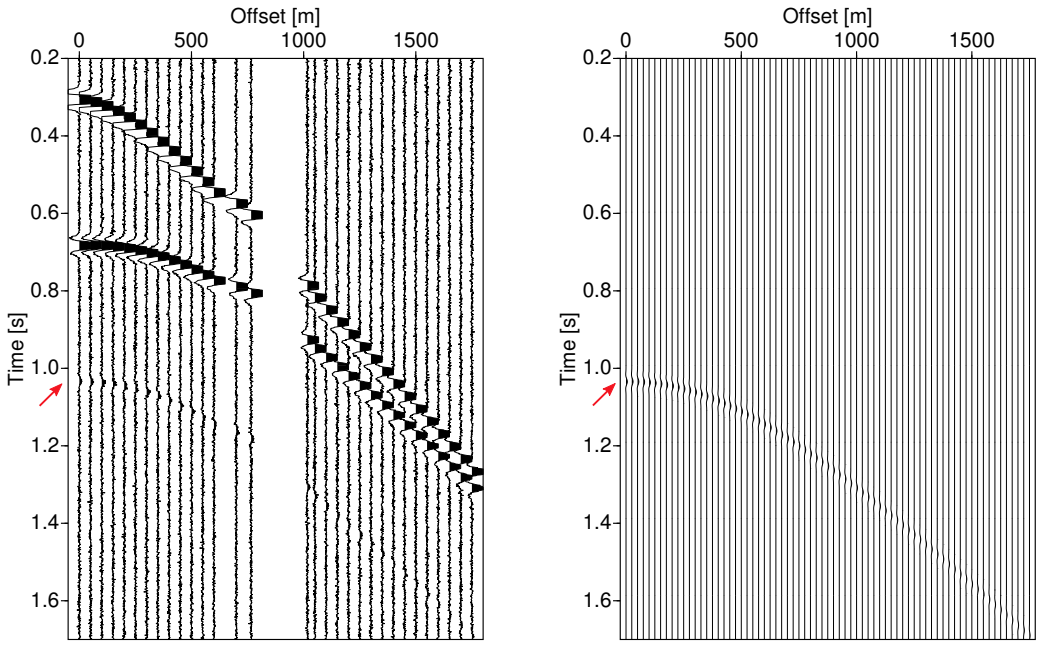

Figure 4.7: The 3D simple model: CMP location #40 of in-line #4. (a) before, and (b) after prestack diffraction separation. The diffraction apex is indicated with the red arrow at 1.1 s.

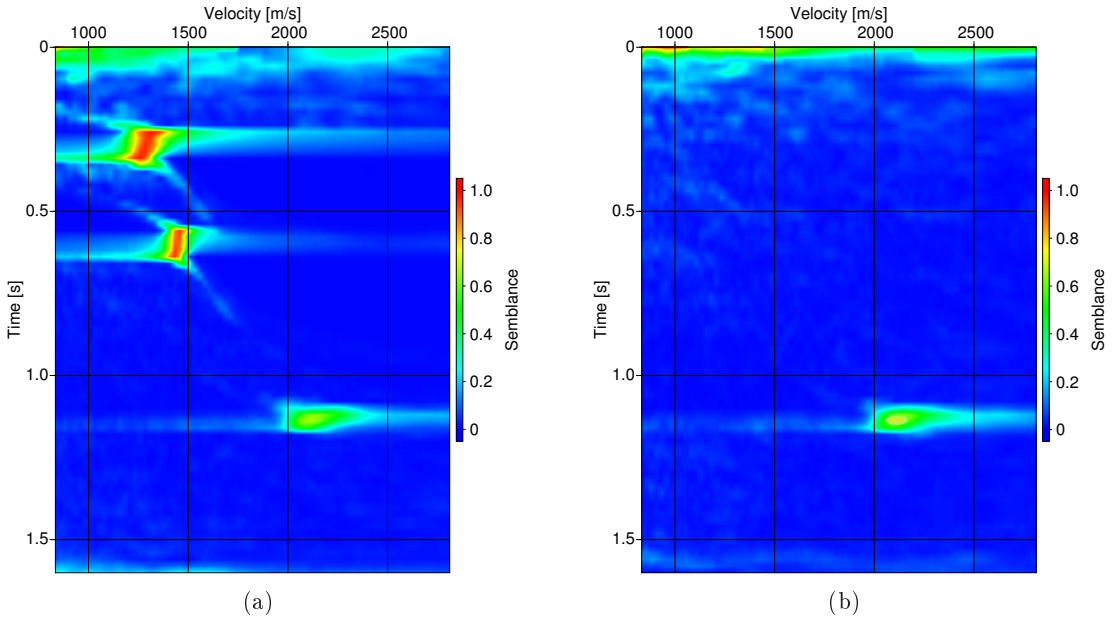

Figure 4.8: The 3D simple model: The velocity spectra for the corresponding CMP position in the previous figure. (a) before, and (b) after prestack diffraction separation. The maximum coherence for the diffraction at about 1.1 s.

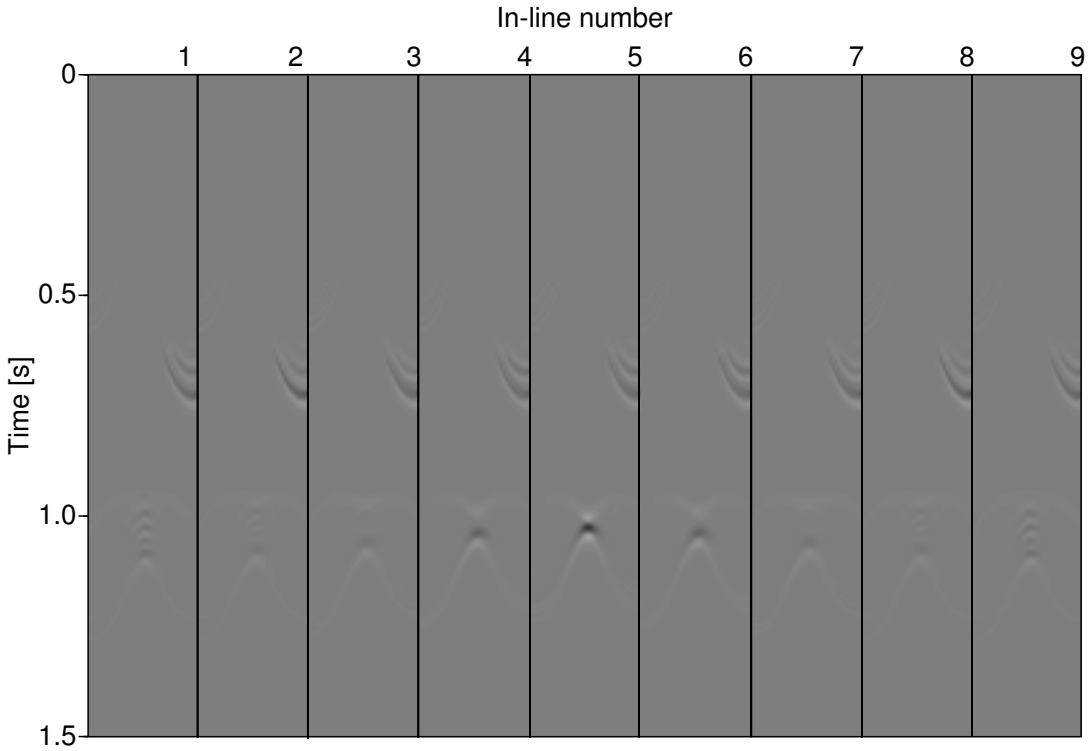

Figure 4.9: The 3D simple model: The time-migrated section of the diffraction-only data. The diffraction is well-focused to its apex (at the in-line #5). Some artifacts due to the residual reflection are also present, e.g. at around 0.7 s.

4.5 Application to the 3D SEG/EAGE salt model

In order to evaluate the performance of the workflow, I choose the SEG/EAGE wide azimuth (WAZ) complex data set. The data was introduced by Sandia National Library (SNL). The model describes a complex salt body in the Gulf of Mexico. The top of the salt is rugged and generates different patterns of diffraction events. I chose a portion of the data over the salt body for processing with in-line ranges from 94 to 286 and cross-line ranges from 43 to 428. The CMP bin size is 40×20 m^2 in in- and x-line directions, leading to a maximum fold of 18. The offset ranges from 0 to 2680 m.The modeling and acquisition parameters are given in Table 4.2.

Figure 4.10 displays the general view of the salt model in a 3D cross-plot in the top. In addition, two arbitrary in-line and x-line planes which cross the center of the salt body can be seen in the bottom. Figure 4.11(a) displays the stacked section of the in-line 200 from a location at the center of the salt body prior to diffraction separation. It exhibits different diffraction patterns, as expected, as well as conflicting dips, where diffractions and reflections intersect.

Acquisition geometry	
Number of sailline	26
Number of shot	96
Receiver interval	40 m
Shot interval	80 m
Minimum offset	0 m
Maximum offset	2680 m
Number of receivers	348
Maximum fold	20
Inline interval	40 m
Xline interval	20 m
Recording parameters	
Recording time	5 s
Sampling interval	4 ms
Frequency content	
Dominant frequency	18 Hz

Table 4.2: Parameters used for the generation of 3D SEG/EAGE synthetic model.

4.5.1 Pre- and poststack diffraction separation results

Figures 4.11(b) and 4.11(c), respectively, display ZO diffraction-only data as a result of post- and prestack diffraction separation. I use the same separation threshold in both cases. By comparison, it is evident that the prestack diffraction separation leads to a better result than the poststack diffraction separation: Not only are the diffracted events considerably

better separated but the data quality was also enhanced. However, some residual reflection energy is still present in both sections. Figure 4.12(a) to 4.12(c) show according results for x-line 300. Again, the prestack diffraction separation exhibits higher potential regarding diffraction separation and data enhancement compared to the poststack method.

For further evaluation, I choose a time slice through the center of the data set at about 2.5 s. Figure 4.13(a) to 4.13(c) display the stacked section, post- and prestack separated diffraction-only data, respectively. Although most of the diffracted energy is separated well, some residual reflections are still present in the data. Furthermore, some gaps and terminations are present in both sections since conflicting dips are not handled in the workflow and thus lead to difficulties in such regions.

4.5.2 Diffraction-based whole data imaging

Finally, I determine time migration velocities from the diffraction-only data obtained in the previous step. Figure 4.14(a) and 4.14(b) displays a common data point gather from in-line 130 and the corresponding velocity spectra before and after prestack diffraction separation, respectively. By comparing the results, I could confirm that indeed mostly diffractions are present in the diffraction-only data and only few residuals of reflections remain. I observe that, despite the low quality of the data (e.g., the low fold, the low SNR and the low maximum offset), 3D prestack diffraction separation leads to higher coherency and better focused picks for time migration velocity analysis. Note that the semblance based analysis is usually affected by the poor S/N ration. However, the ratio can be improved with the help of prestack diffraction separation, therefore, more reliable velocities can be extracted.

Figure 4.15(a) and Figure 4.15(b) display the same procedure for time migration velocity model building tuned to diffractions in x-line 300. Most of diffractions are present in diffraction-only gather after prestack diffraction separation and, only few reflection residuals remain. Subsequently, as it is seen in the velocity spectra, the prestack diffraction separation leads to higher maximum coherence as well as better focused picks. Here, the diffraction-based time migration velocity model were built using automatic picking of high coherences for all CMPs.

Figure 4.16 displays prestack time migration results before and after prestack diffraction separation for in-line 130, Figure 4.17 for x-line 300 and Figure 4.18 for a time slice at 2.5 s. I observe that the top-of-salt is imaged well and the diffractions are generally better collapsed after prestack diffraction separation, as outlined by the red arrows in the figure, suggesting that diffraction velocities can be a good supplement in regions where migration velocities are otherwise hard to obtain. However, diffraction-based imaging may fail and lead to blurred images in regions without enough diffractions. In addition, conflicting dips and unfocused diffractions due to more complex diffractor geometry than the point-type considered in this work may also deteriorate diffraction velocity model building and subsequent imaging.

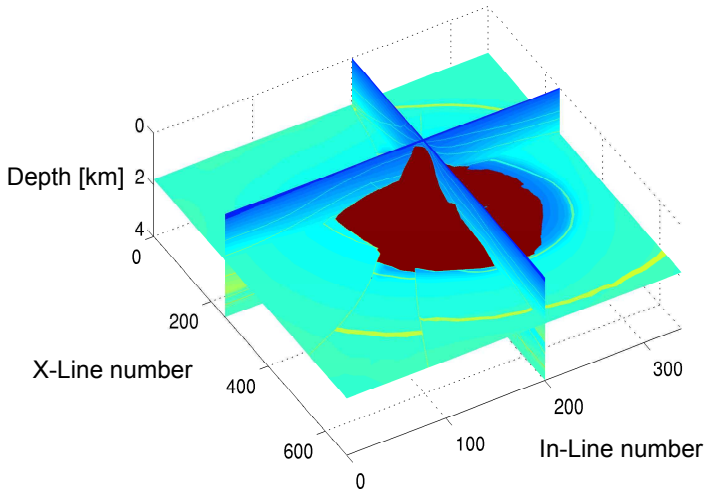

(a)

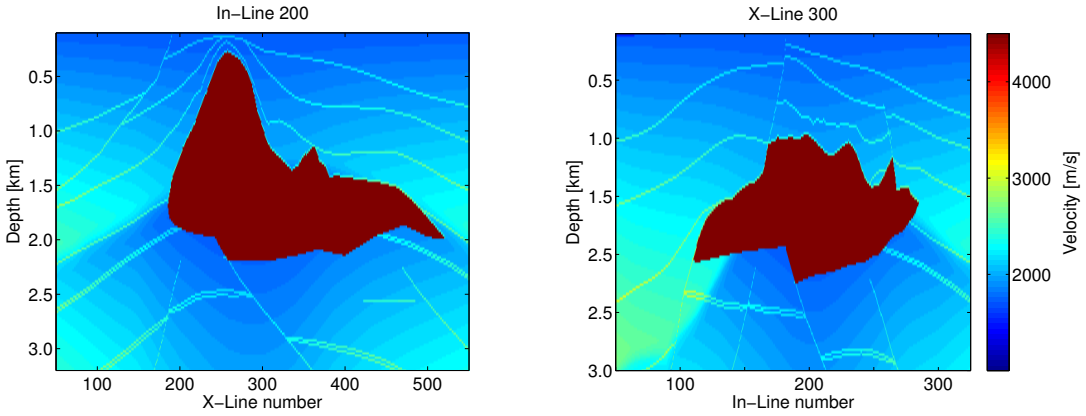

(b) (c)

Figure 4.10: A 3D view of the SEG/EAGE C3 WA salt model (a). The velocity is variant from 1500 to 4500 m/s. It models a salt body in the gulf of Mexico. (Bottom) Two arbitrary slices of an in-line 200 (b) and a x-line 300 (c).

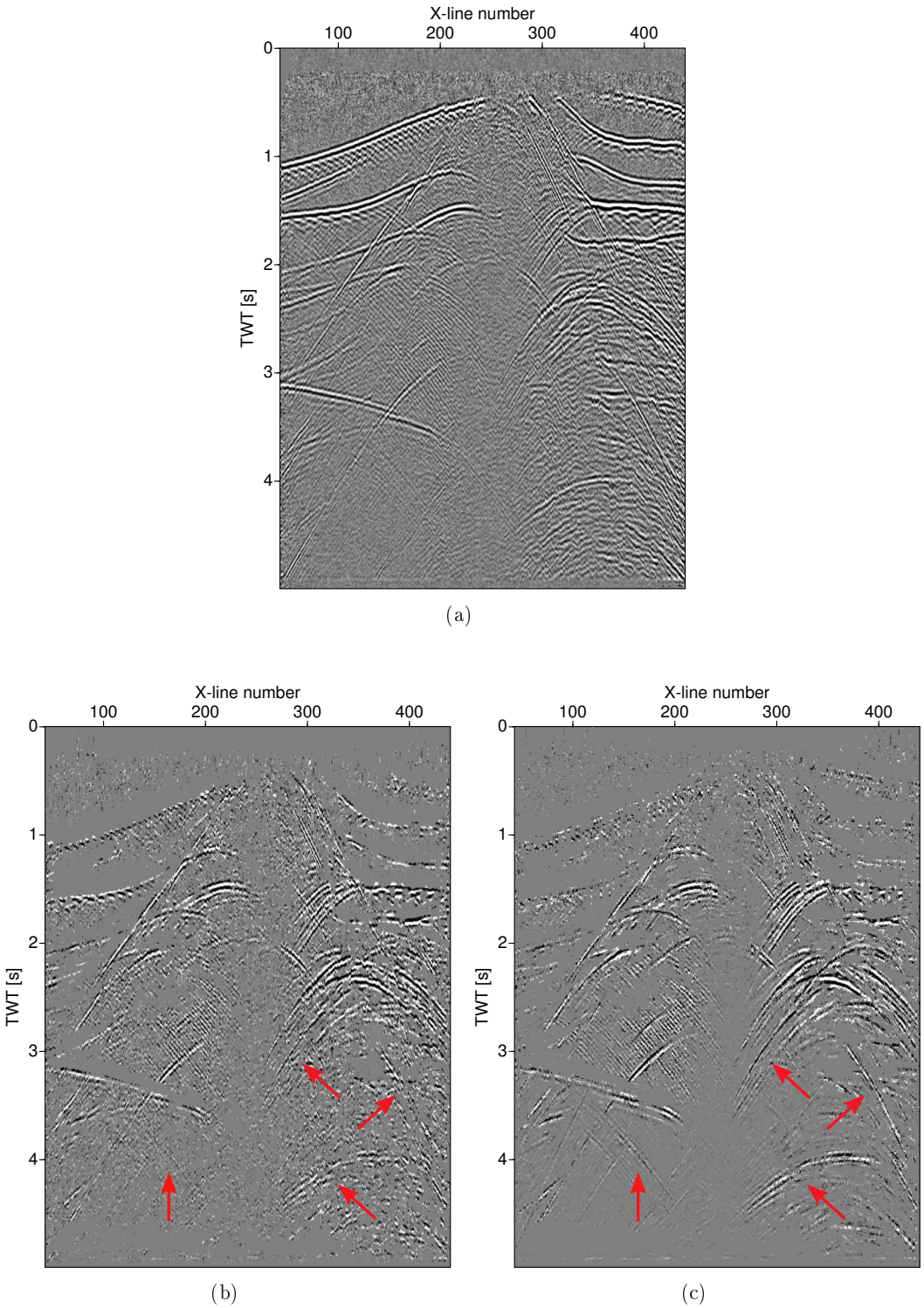

Figure 4.11: SEG/EAGE salt model, the in-line 200: (a) stacked section prior to diffraction separation, (b) ZO diffraction-only data after poststack diffraction separation, (c) ZO diffraction-only data after prestack diffraction separation. Red arrows indicate events that were better focused after prestack diffraction separation.

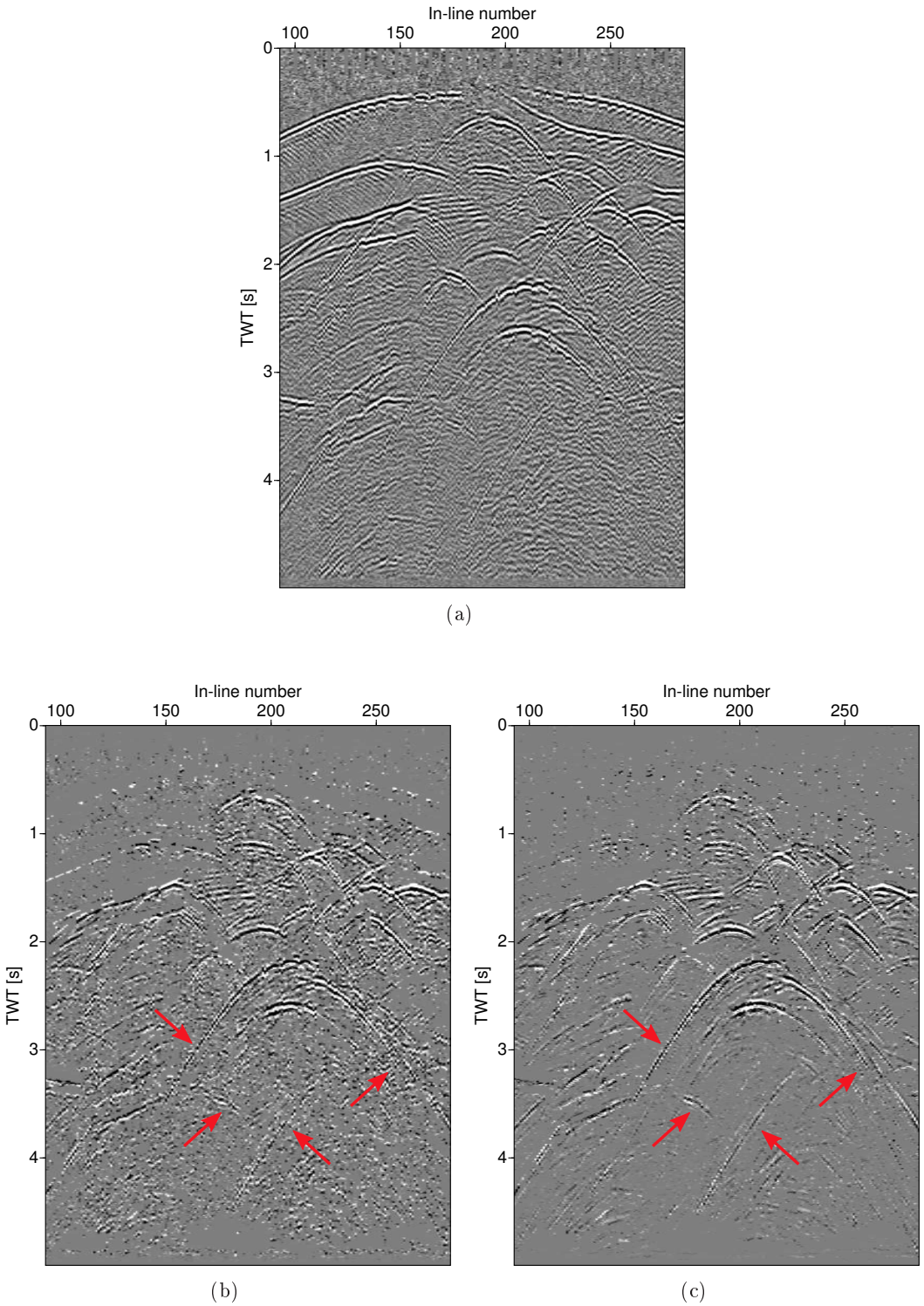

Figure 4.12: SEG/EAGE salt model, the x-line 300: (a) stacked section prior to diffraction separation, (b) ZO diffraction-only data after poststack diffraction separation, (c) ZO diffraction-only data after prestack diffraction separation. Red arrows indicate events that were better focused after prestack diffraction separation.

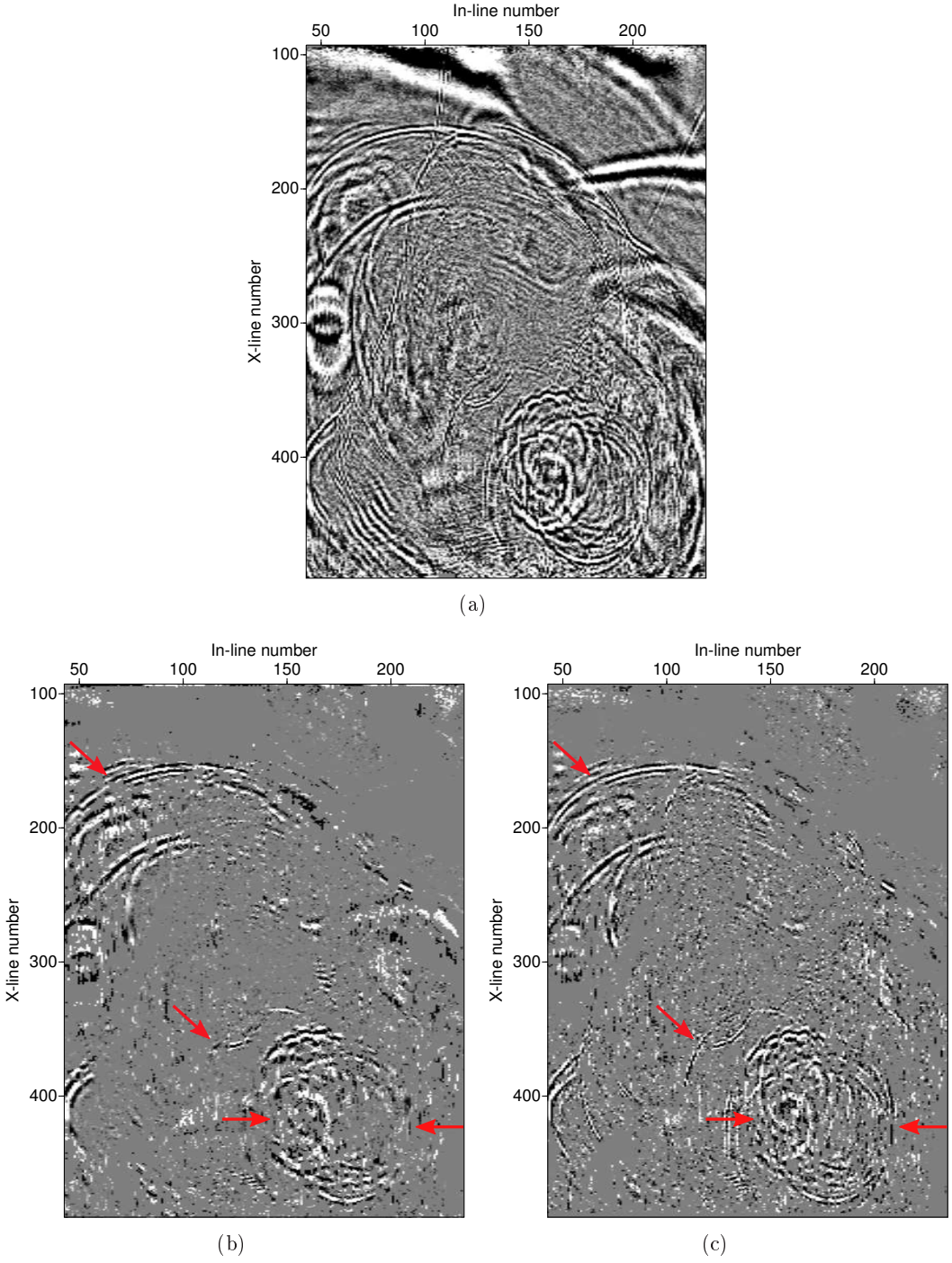

Figure 4.13: SEG/EAGE salt model, time slice at 2.5 s: (a) stacked section prior diffraction separation, (b) ZO diffraction-only data after poststack diffraction separation, (c) ZO diffraction-only data after prestack diffraction separation. Red arrows indicate events that were better focused after prestack diffraction separation.

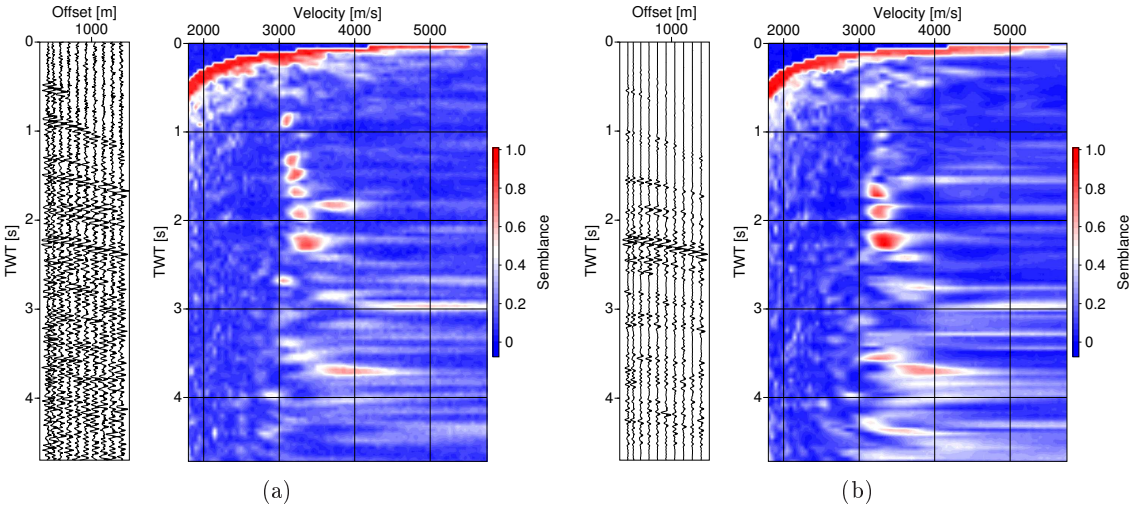

Figure 4.14: SEG/EAGE salt model: Results for a common-data-point (CDP) gather from in-line 130 and the corresponding velocity spectrum (a) before and (b) after prestack diffraction separation.

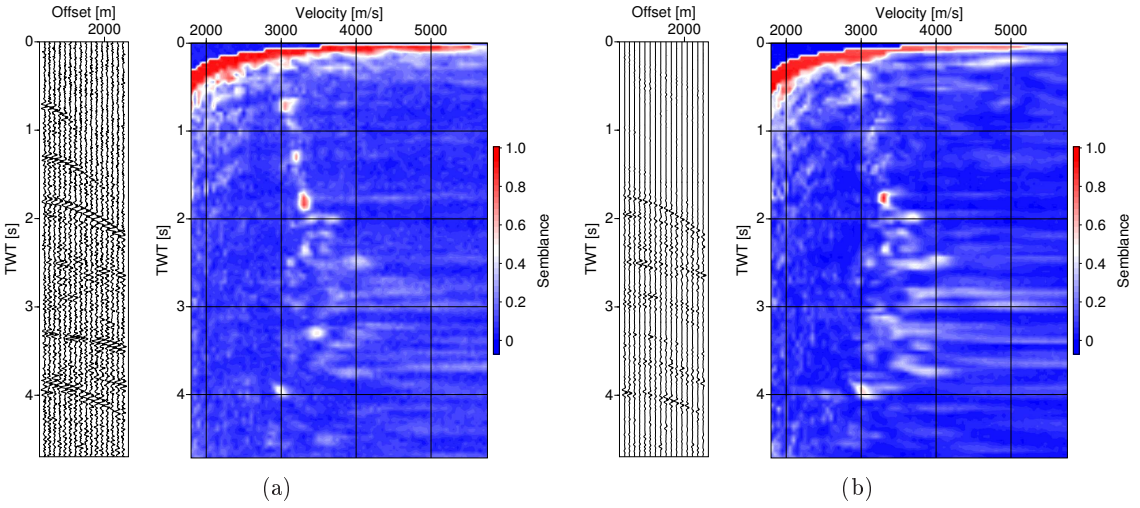

Figure 4.15: SEG/EAGE salt model: Results for a common-data-point (CDP) gather from x-line 300 and the corresponding velocity spectrum (a) before and (b) after prestack diffraction separation.

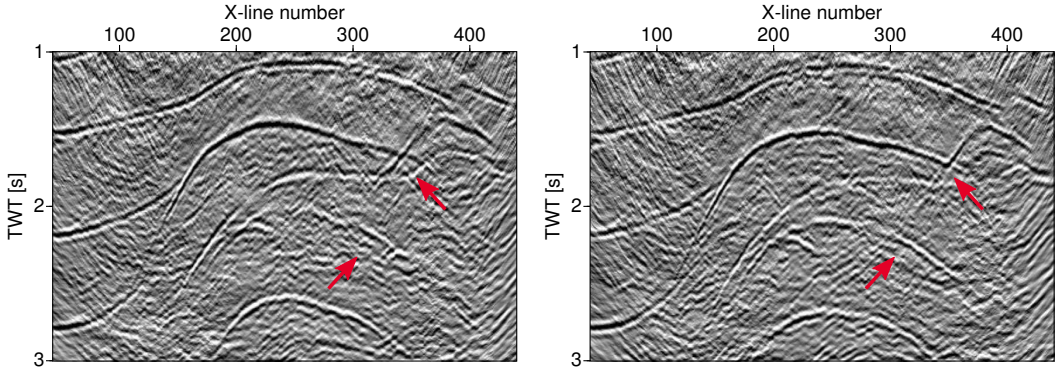

(a) (b)

Figure 4.16: SEG/EAGE salt model, the in-line 130: Prestack time migration using the velocity model obtained from data (a) before and (b) after prestack diffraction separation. Red arrows indicate events that were better focused using time migration velocities obtained from diffraction-only data.

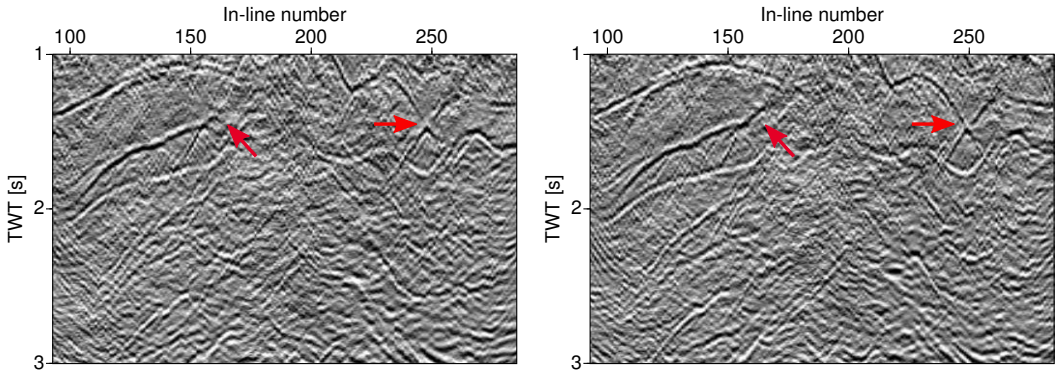

(a) (b)

Figure 4.17: SEG/EAGE salt model, the x-line 300: Prestack time migration using the velocity model obtained from data (a) before and (b) after prestack diffraction separation. Red arrows indicate events that were better focused using time migration velocities obtained from diffraction-only data.

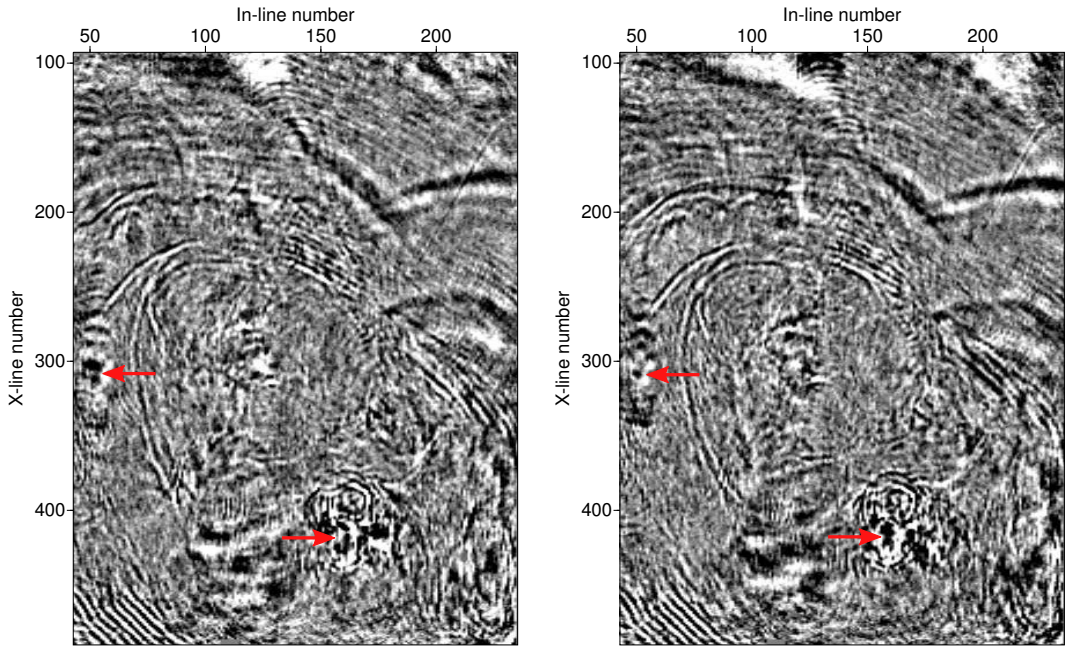

(a) (b)

Figure 4.18: SEG/EAGE salt model, the time slice at 2.5 s: Prestack time migration using the velocity model obtained from data (a) before and (b) after prestack diffraction separation. Red arrows indicate events that were better focused using time migration velocities obtained from diffraction-only data.

Chapter 5

Improved diffraction weight

In the previous chapters, I have presented a new approach for diffraction separation and imaging based on the partial CRS stack technique. I have compared the result of the new approach with an existing poststack method. The new method for prestack diffraction separation demonstrated advantages over the poststack approach. The prestack data enhancement facility of the proposed method allows a better diffraction separation and imaging. Moreover, the workflow for prestack diffraction separation provides a velocity model for time migration.

In this chapter, I focus on the diffraction threshold function and propose a new function based on the projected Fresnel zone (PFZ) to improve diffraction separation and the subsequent imaging. The Fresnel zone is not only important in seismic resolution studies or correct determination of migration aperture but also, as I show in the following, in diffraction separation. Furthermore, the resulting weight function can be incorporated in both pre- and poststack diffraction separation workflows. To evaluate the performance of the new function, it is applied to a gradient as well as a complex data set.

5.1 Diffraction weighting

According to the 2D CRS theory, the radii of curvature of the NIP- and N-wave coincide for diffractions. Thus, the ratio of R_{NIP} and R_N can be used to identify diffractions. Dell and Gajewski (2011) formulated a CRS-based exponential function to identify diffractions in the data (see Equation 3.3). This function allows a smooth and fast decay in transition from reflections to diffractions for a band-limited seismic data. However, since the radii of curvature may slightly differ for a diffracted event, a threshold is required to stabilize the separation process. The choice of threshold heavily depends on the subsurface complexity. The lower the threshold, the more residual reflections will remain in the data.

The existing function by Dell and Gajewski (2011) provides a good discrimination between reflections and diffractions especially in shallow parts of the data. However, the separation potential of the existing function decreases for higher times (Schwarz, 2015). Moreover, it may fail in the case of the subsurface structures with small radii of curvature. Such diffraction-like structures will pass the filtering process and interfere with real diffractions especially in deeper parts. In addition, the existing function is vulnerable to the presence of strong noise, which lead to a poor diffraction separation (see, e.g. Voss, 2013; Guntern, 2013; Wissmath., 2016; Bakhtiari Rad et al., 2016).

In a recent attempt to improve the CRS-based diffraction weight functions, Schwarz (2015) proposed an angle-based diffraction weight based on the difference in the emergence angle estimation of the time- and velocity-shifted versions of the i-CRS operator. The new weight by Schwarz (2015) allows sharper distinction between diffractions and reflections especially in higher times, however, since there is no emergence angle difference in the diffraction apices, it may lead to insufficient separation. On the other hand, the proposed angle-based solution may fail in the separation of the diffractions with short or missing tails, since tails of diffractions play a key role in the diffraction identification. To solve these issues, Schwarz (2015) suggested to combine the angle-based weight with the existing threshold function by Dell and Gajewski (2011). In another attempt, Wissmath. (2016) suggested to use CO CRS attributes to improve diffraction separation in common-offsets. In the following, I present a new diffraction weight to enhance diffraction separation and the subsequent imaging. I compare performance of the proposed weight with the existing function by Dell and Gajewski (2011).

5.2 The PFZ-based diffraction identification

The concept of the Fresnel zone was initially introduced in seismic data processing as a measure for lateral resolution. The Fresnel zone is a frequency dependent volume on the reflector within most of the wave energy is interfering constructively (Yilmaz, 2001). The energy is added constructively in the first Fresnel zone. The energy is added destructively for the second Fresnel zone and added constructively again for the third Fresnel zone and so on. The determination of the Fresnel zones can be difficult and cannot be calculated exactly. There are a number of different approximations to determine the Fresnel zone which most of them require the knowledge of the subsurface model (Yilmaz, 2001).

Hubral et al. (1993) introduced the concept of the projected (first) Fresnel zone as a time domain counterpart to the first interface Fresnel zone in the depth domain (see Figure 5.1). This implies that the major contribution stemming from a particular reflector segment in the depth domain can be found inside the associated projected (first) Fresnel zone. Thus, the projected (first) Fresnel zone represents an optimum size of aperture for stacking procedure. Hubral et al. (1993) also demonstrated that the projected (first) Fresnel zone can be estimated from traveltime measurements based on the paraxial ray theory. Schleicher et al. (1997) generalized the approach by Hubral et al. to any arbitrary acquisition geometry.

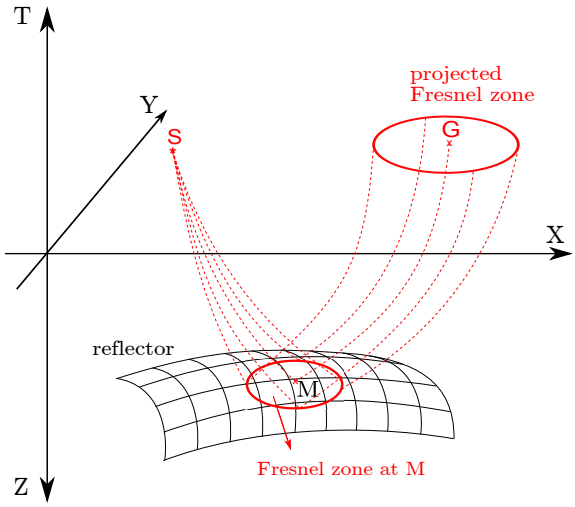

Figure 5.1: The projected (first) Fresnel zone for common-shot configuration (modified after Schleicher et al., 1997). It is constructed by projecting the actual Fresnel zone at M along paraxial rays into the offset-midpoint plane.

In theory, the first Fresnel zone can be directly determined from the difference of the reflection and diffraction traveltime as follows:

$$|t_D(x) - t_R(x)| \leq \frac{T}{2}. \tag{5.1}$$

where x denotes the shot and receiver coordinates for an arbitrary acquisition geometry and, T denotes the prevailing period of source signal. For a 2D ZO case, x simply reduces to the midpoint displacement $(x_m - x_0)$. The true diffraction and reflection traveltimes, t_D and t_R, depend on the subsurface model which is hard to obtain. However, the CRS attributes provide a good approximation for the reflection as well as diffraction traveltimes (in terms of Equations 2.22 and 3.2). Therefore, for the analytic description of the traveltimes, the borders of the projected (first) Fresnel zone are simply given by $|t_D(x_m - x_0, h) - t_R(x_m - x_0, h)| = T/2$. Mann (2002) solved the equation and obtained the following analytical solution for the ZO configuration:

$$R_{PFZ} = \frac{2}{\cos\alpha}\sqrt{\frac{v_0\, T}{2\,|K_N - K_{NIP}|}}, \tag{5.2}$$

where R_{PFZ} denotes the width of the PFZ. Equation 5.2 is derived using a parabolic traveltime approximation since the Equation 5.1 cannot be solved analytically using hyperbolic approximation. However, Mann (2002) numerically showed that both parabolic and hyperbolic approximations give very similar values in case of typical frequency content of seismic data.

Although in theory a Fresnel zone is not defined (respectively infinite) for point diffractors, in practice, diffractors have a spatial extent. In consequence, a Fresnel zone can be assigned to the resulting events. Since its width, and therefore the width of the PFZ is much larger that the PFZ for a reflection, the difference can be used as a consistent attribute to identify diffractions in the data (see, e.g. Bakhtiari Rad et al., 2016). Since, the existing function still performs consistently in apices (Schwarz, 2015), I suggest to combine the existing function by Dell and Gajewski (2011) with the width of the PFZ to enhance separation of diffraction apices as well as tails via:

$$W = \hat{R}_{PFZ} \cdot W_D \quad . \tag{5.3}$$

Here $\hat{R}_{PFZ}$ denotes the normalized width of the PFZ and W_D is the existing weight (Equation 3.3). Both are evaluated for every ZO sample.

As I will demonstrate with examples in the following, this function can be directly applied as a weight in contrast to using a threshold as was necessary for (Equation 3.3).

5.3 Application to a gradient model

Figure 5.2(a) illustrates the constant velocity gradient model. The model comprises several diffractors of different type including edges and a point. Synthetic seismograms were modeled with the Seismic Un*x routine susynlv for a velocity at the surface of 2000 m/s with a vertical gradient of 0.5 s^{-1}. Noise with S/N ratio of 10 was added to the data. The acquisition parameters are given in Table 5.1.

Acquisition geometry	
Number of CMP bins	451
Maximum fold	80
CMP interval	25 m
Minimum offset	0 m
Maximum offset	7932 m
Number of receivers	201
Recording parameters	
Recording time	5 s
Sampling interval	4 ms
Frequency content	
Dominant frequency	30 Hz

Table 5.1: Parameters used for the generation of the 2D gradient model.

The CRS stacking method is then applied to the data. Figure 5.2(b) displays the corresponding ZO stacked section of the data set. Different diffracted events as well as

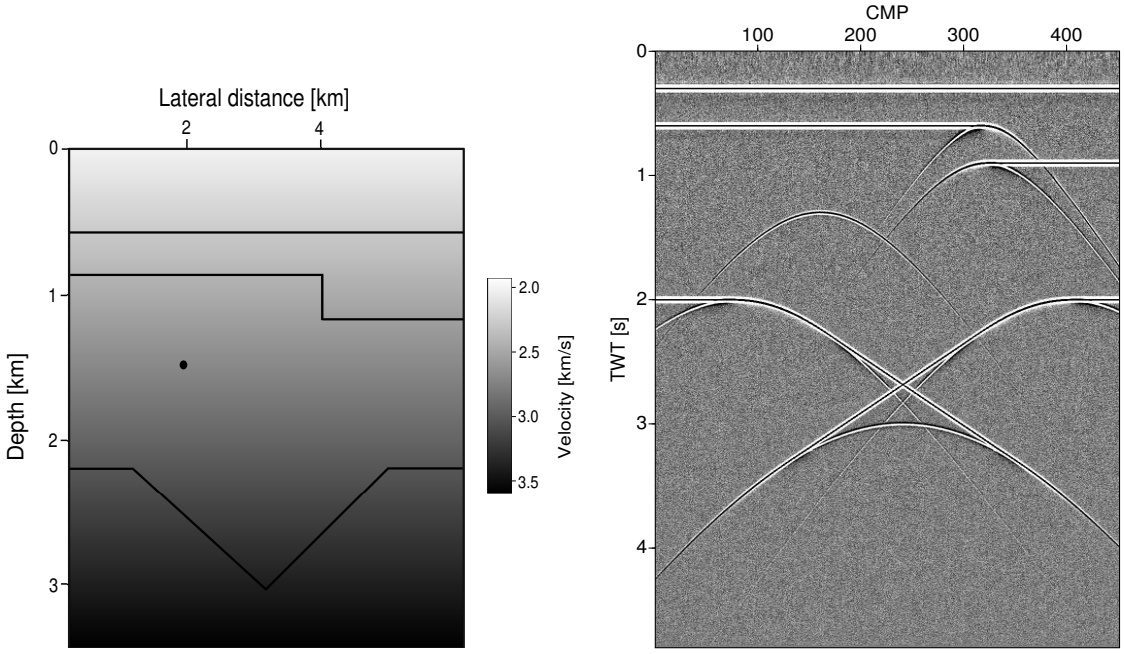

(a) (b)

Figure 5.2: Gradient model: (a) the velocity model and (b) the ZO stacked section.

reflections are present in the section. Conflicting dips are also present, e.g., in CMP about 250 and 2.7 s TWT. Figure 5.3(a) shows the width of the PFZ. One can see that the diffractions have very high width compared to the reflections. Figure 5.3(b) and 5.3(c) display the existing function by Dell and Gajewski (2011) and the new weight section, respectively. In the both sections, diffractions show in red color with values close to one, whereas blue colors indicate reflections and noise. The new weight is by far less contaminated with noise. Moreover, it is also less sensitive to the value of the selected separation threshold, which allows for a better separation.

The new weight can be incorporated in both the pre- and poststack diffraction separation workflows. Figure 5.4(a) and Figure 5.4(b) display diffraction-only data as a result of poststack diffraction separation using the existing and the new weight, respectively. In contrast, Figure 5.5(a) and Figure 5.5(b) display diffraction-only data as a result of prestack diffraction separation using the existing and the new weight, respectively. The new weight is advantageous over the existing weight in the both pre- and poststack diffraction separation workflows. The diffraction tails as well as the apices are better separated by the new weight. Moreover, less residual reflections are present.

The improved diffraction separation using the new weight therefore allows to enhance the quality of subsequent diffraction imaging. Figure 5.6(a) and Figure 5.6(b) show the time-migrated section of the diffraction-only data separated by the existing and new weight, respectively. The migration velocity model is the same in the both experiment. It implies that the diffractions separated by means of the new weight are considerably better focused and less reflection residuals are present.

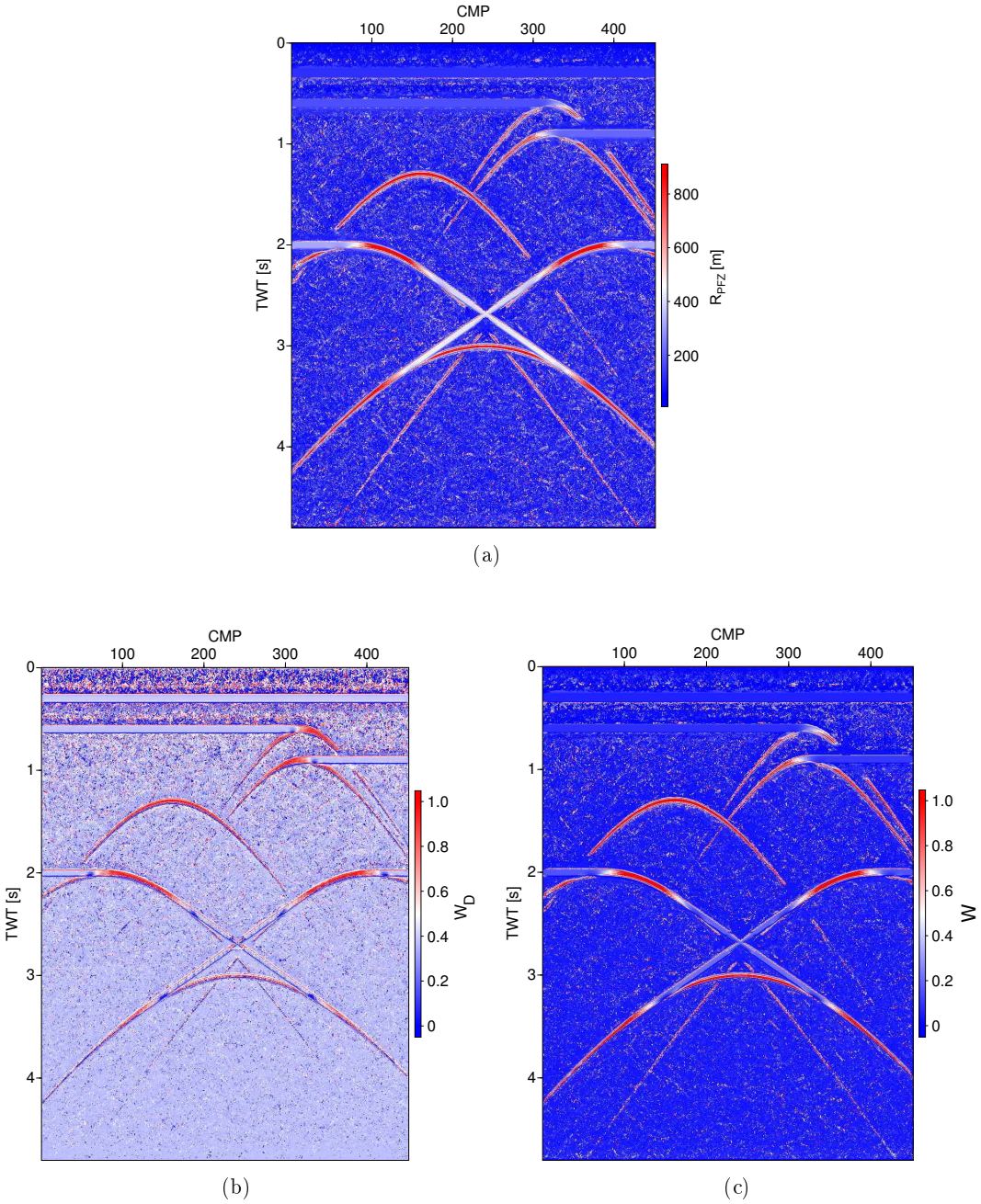

Figure 5.3: Gradient example: (a) the width of the projected first Fresnel zone, (b) the existing weight function by Dell and Gajewski (2011) and (c) the new weight section.

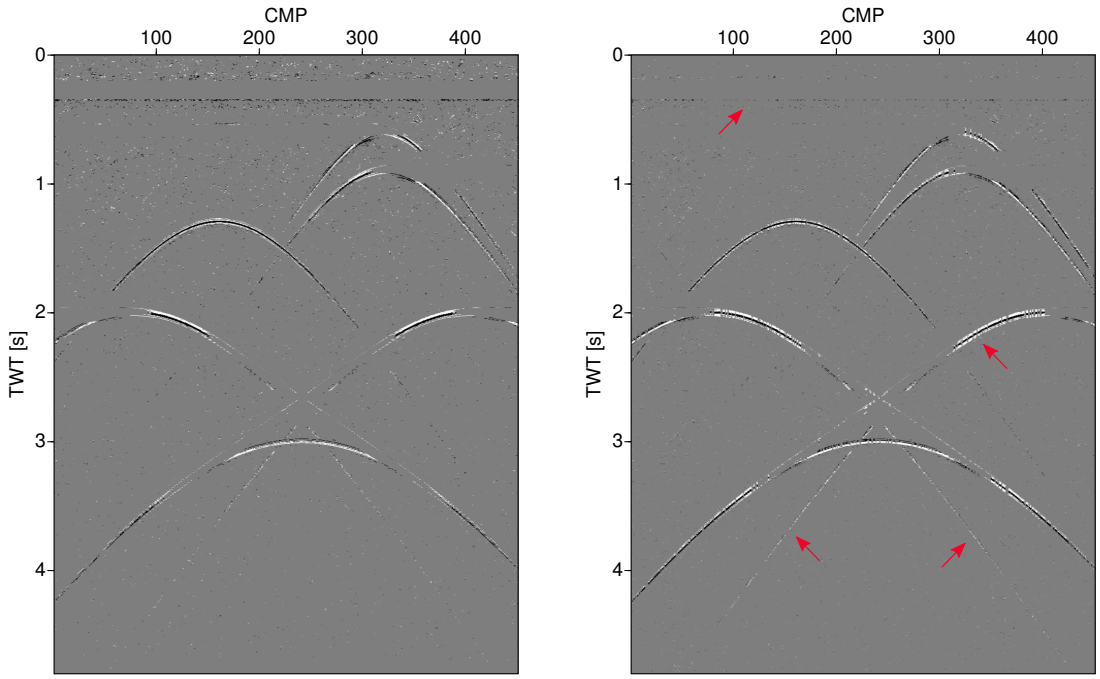

(a) (b)

Figure 5.4: Gradient model: poststack diffraction separation using (a) the existing weight and (b) the new weight. Red arrows indicate events that were better separated by the new weight. Note the same clip in both sections.

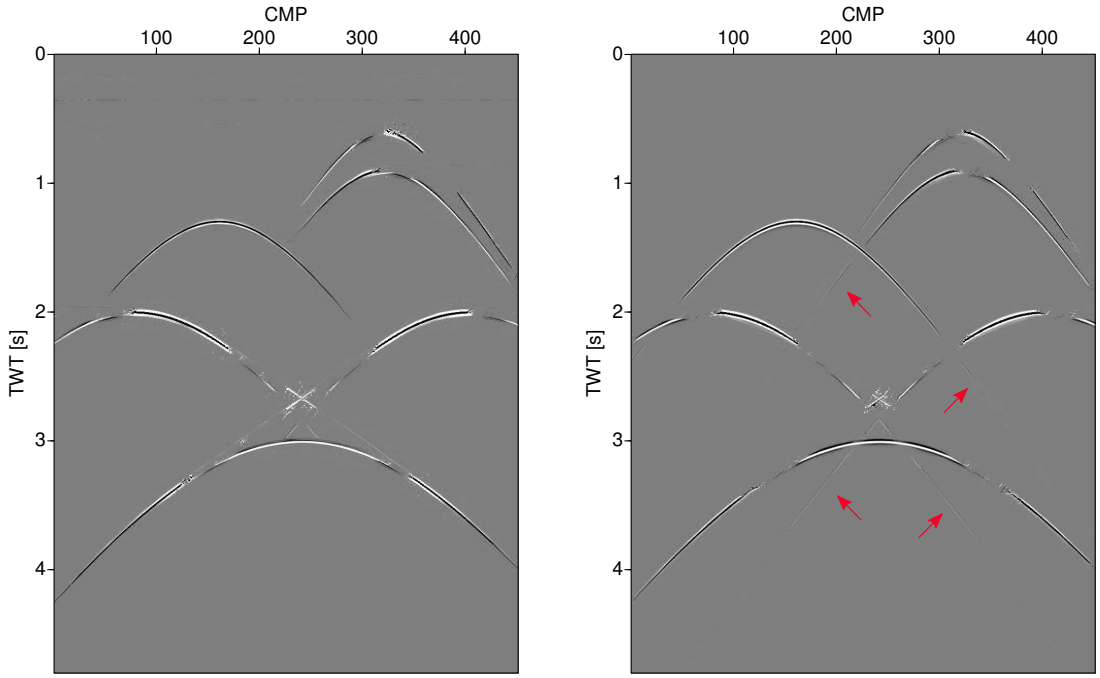

(a) (b)

Figure 5.5: Gradient model: prestack diffraction separation using (a) the existing weight and (b) the new weight. Red arrows indicate events that were better separated by the new weight. Note the same clip in both sections.

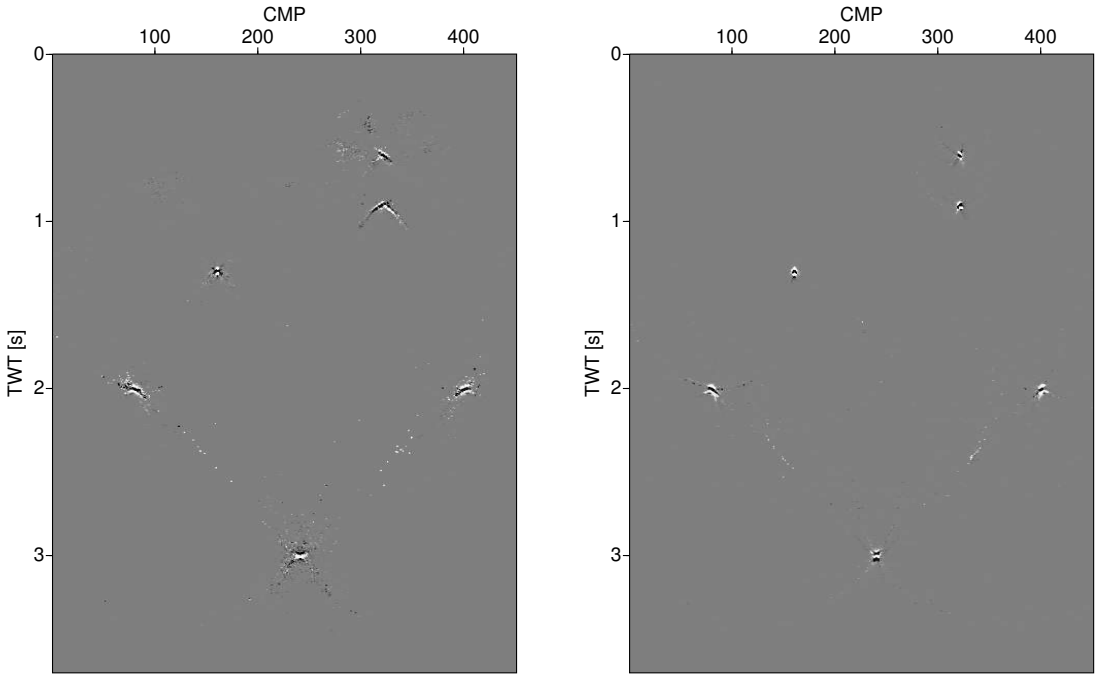

(a) (b)

Figure 5.6: Gradient model: time-migrated section of the diffraction-only data separated by means of (a) the existing weight and (b) the new weight. Note the same clip in both sections.

5.4 Application to the BP 2004 Velocity Benchmark

In the next example, I choose the 2004 BP velocity benchmark model to test the new method in a complex setting. Figure 5.7 displays the velocity model of the data. It consists of a complex salt body regime and can be divided into different distinct parts, each focusing on different challenges for velocity estimation methods. The data was generated with a 15 km streamer with 12.5 m group interval and a 50 m shot interval. Offset range is 0 to 15 km (see, Billette and Brandsberg-Dahl, 2005). The modeling and acquisition parameters are given in Table 5.2.

Acquisition geometry	
Number of shots	1340
Number of receiver	1200
Shot interval	50 m
Receiver interval	12.5 m
Streamer length	15 km
Minimum offset	0 m
Maximum offset	15000 m
CMP range for processing	500-7500
Recording parameters	
Recording time	12 s
Sampling interval	6 ms
Frequency content	
Dominant frequency	27 Hz

Table 5.2: Acquisition and parameters of the 2004 BP velocity benchmark data (after Billette and Brandsberg-Dahl, 2005).

Over 7000 CMPs are selected for processing. Figure 5.8 displays the ZO CRS stacked section of the data. Various patterns of diffractions and triplications due to the salt and complex structures are present in the stacked section. Figure 5.9 display the corresponding PFZ section. The diffractions in this section are marked by red color since they have a very high width of projected Fresnel zone. The bluish parts, in contrast, indicate the reflections and noise which have low values of the width of the projected Fresnel zone.

Figure 5.10 and Figure 5.11 display the existing and the new weight section, respectively. The diffractions in the new weight section are better distinguishable compared to the existing weight. From the figures it is suggested that, the new weight is less sensitive to the separation threshold since the difference between the width of the PFZ for reflections and diffractions is significantly higher. Moreover, the new weight is by far less noisy, implying that the diffraction separation is less affected by the background noise. As a result, most of the reflections and noise are highly attenuated by the new weight.

To better evaluate the performance of the new weight, I compare the result of pre- and poststack diffraction separation using both functions. Figure 5.12 and 5.13 display the

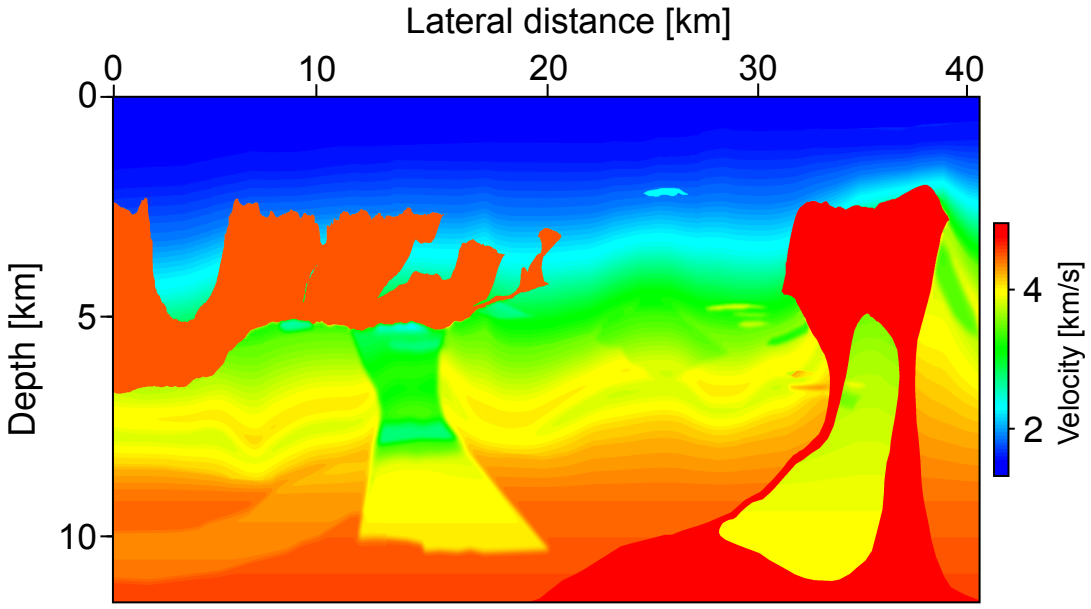

Figure 5.7: The 2004 BP velocity benchmark model.

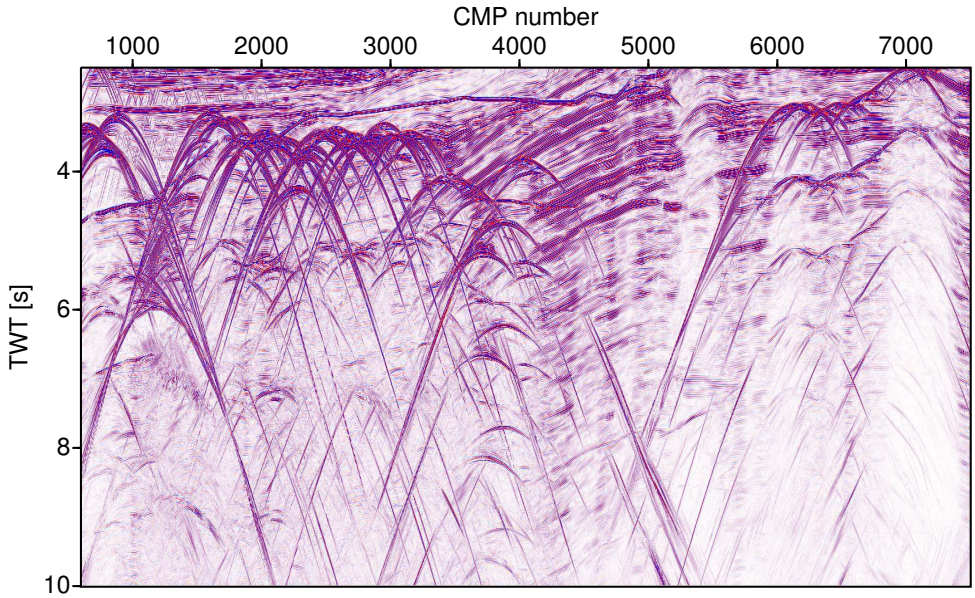

Figure 5.8: BP model: The ZO CRS stacked section.

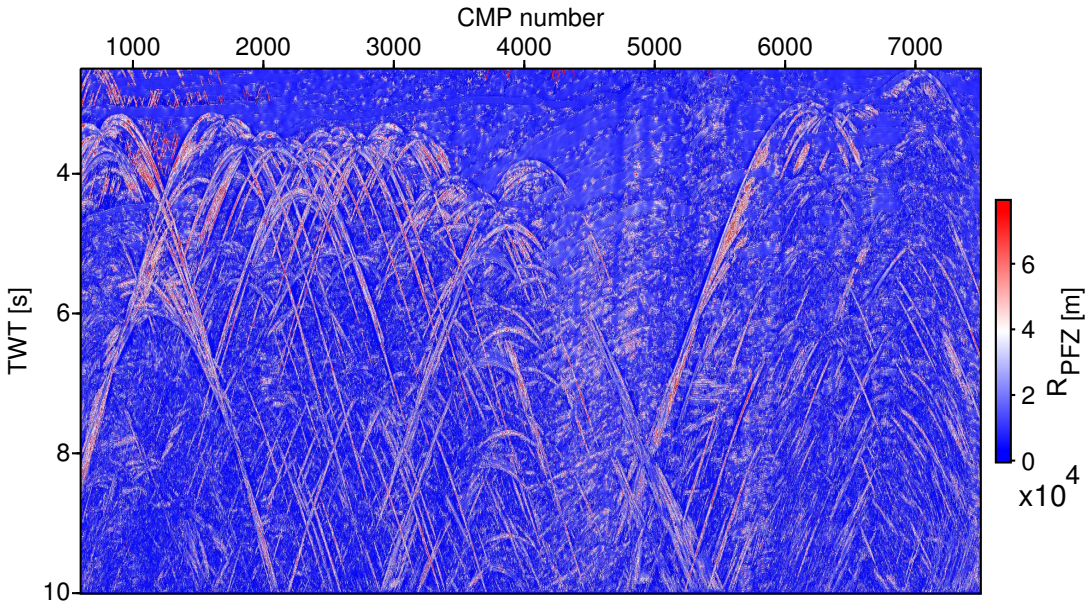

Figure 5.9: BP model: The width of the PFZ section.

poststack diffraction separation using the existing and the new weight, respectively. Figure 5.14 and 5.15 in contrast display the prestack diffraction separation using the existing and the new weight, respectively. The new weight is advantageous over the existing weight in both of the pre- and poststack diffraction separation workflows: The diffraction tails as well as the apices are better separated than for the weight by Dell and Gajewski (2011).

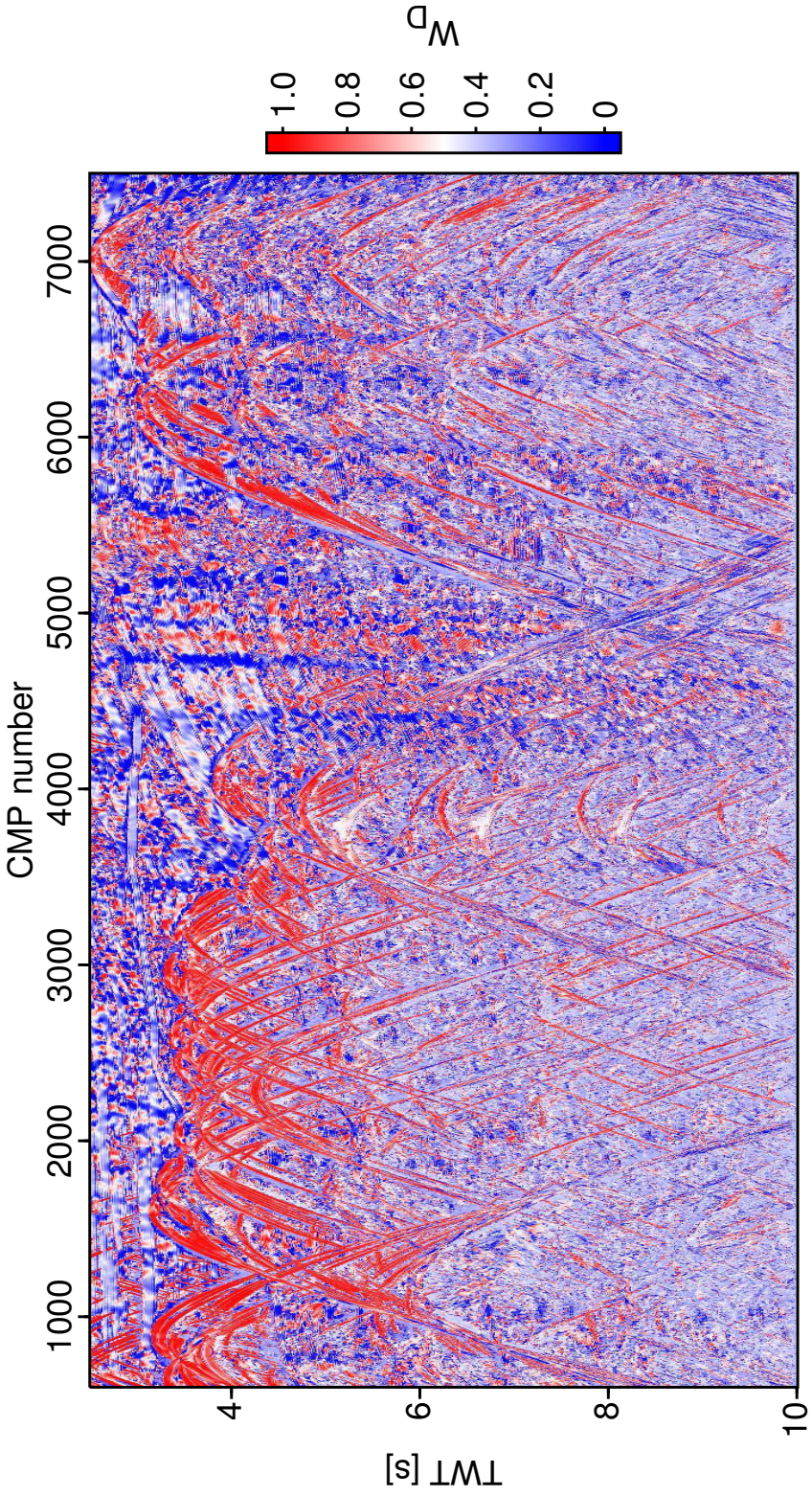

Figure 5.10: BP model: The existing weight by Dell and Gajewski (2011).

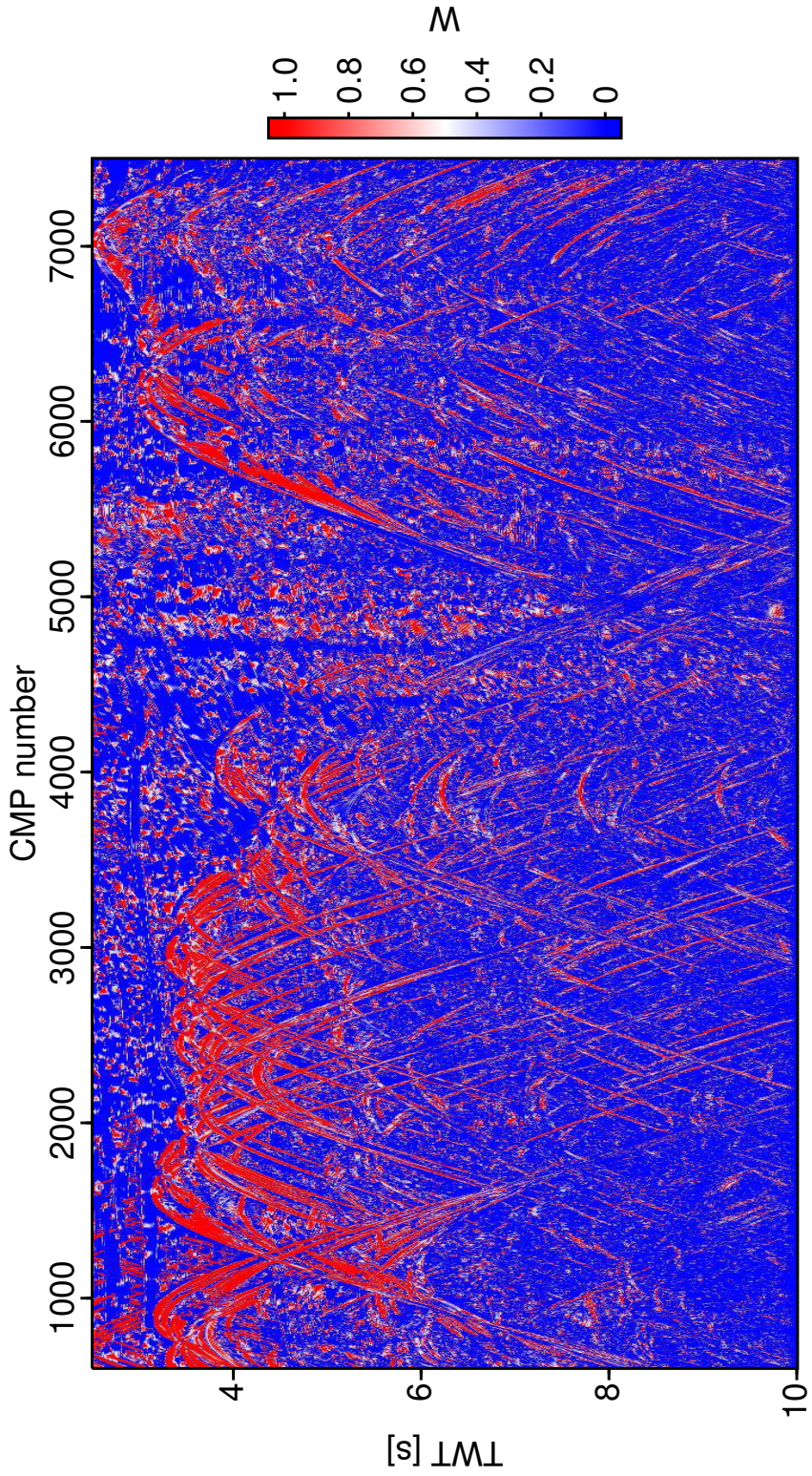

Figure 5.11: BP model: The new weight section.

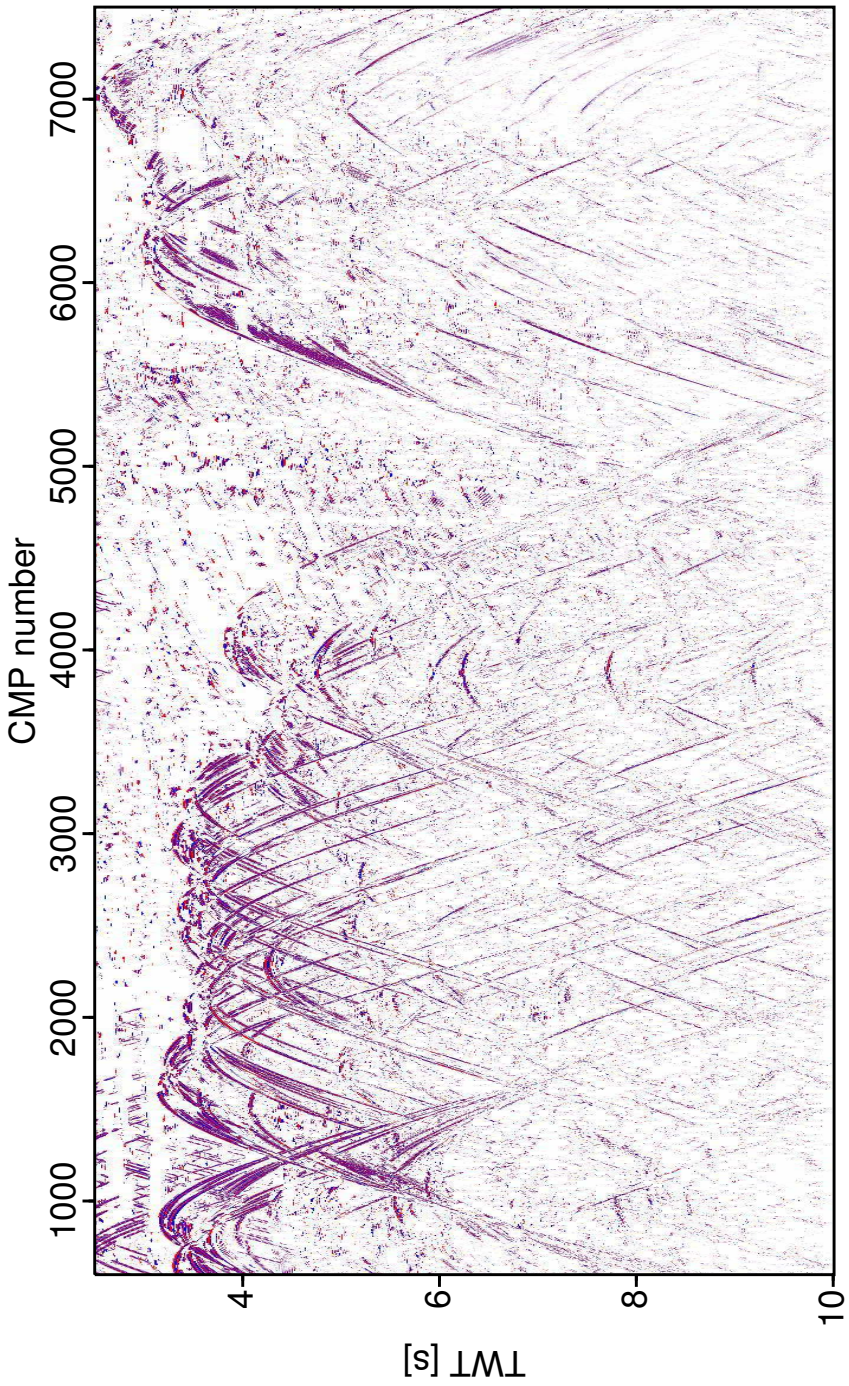

Figure 5.12: BP model: Poststack diffraction separation using the existing weight.

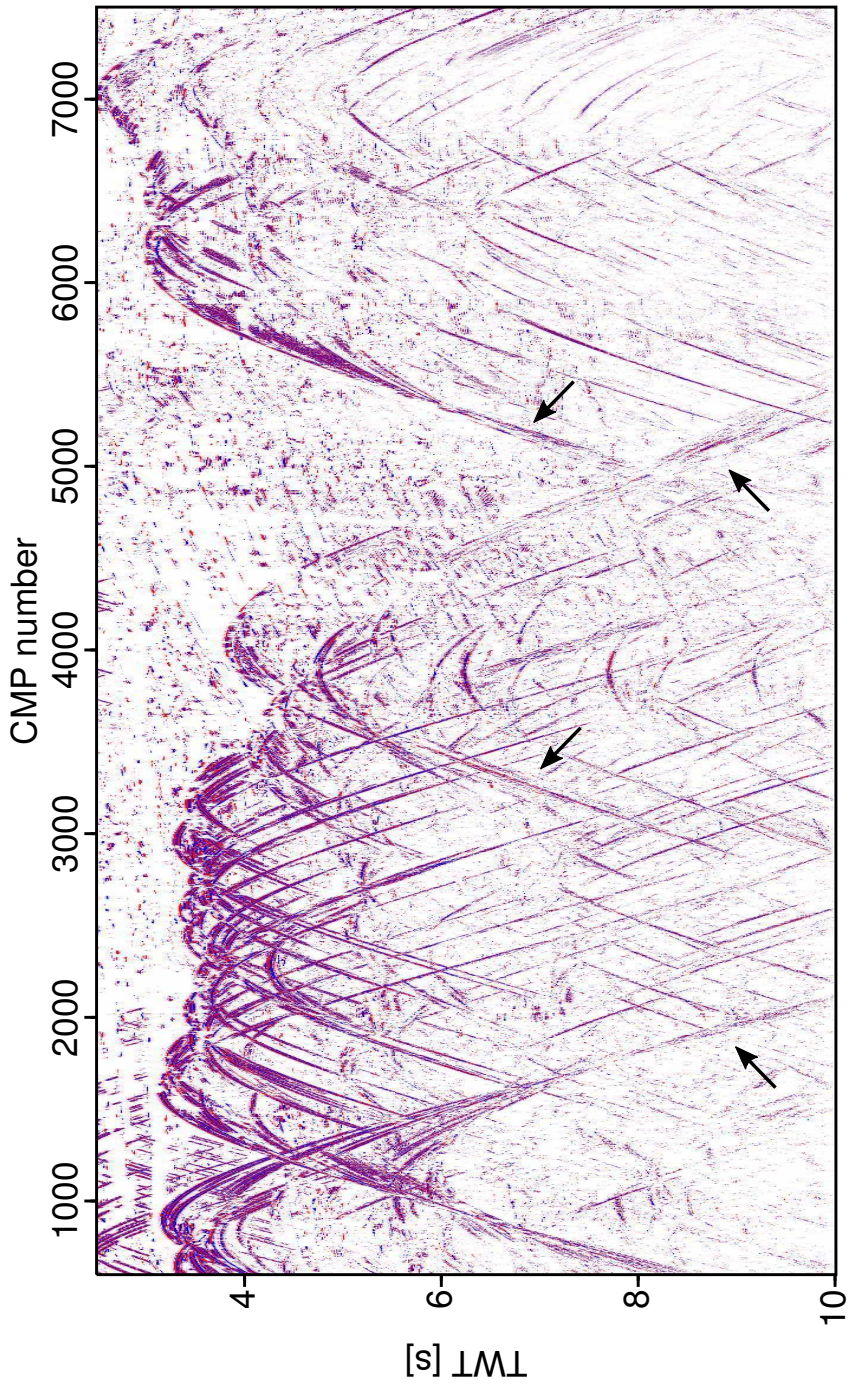

Figure 5.13: BP model: Poststack diffraction separation using the new weight.

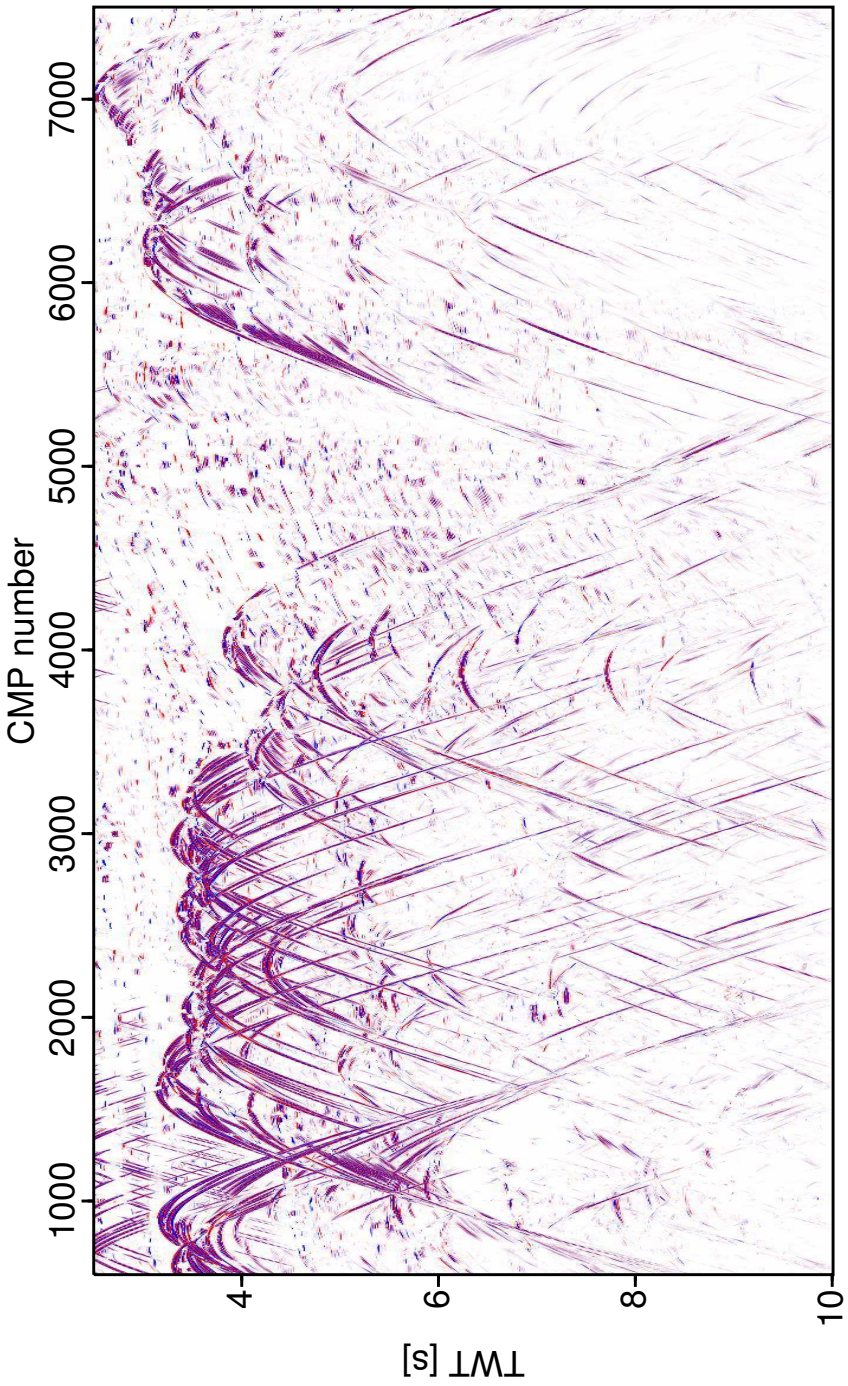

Figure 5.14: BP model: Prestack diffraction separation using the existing weight.

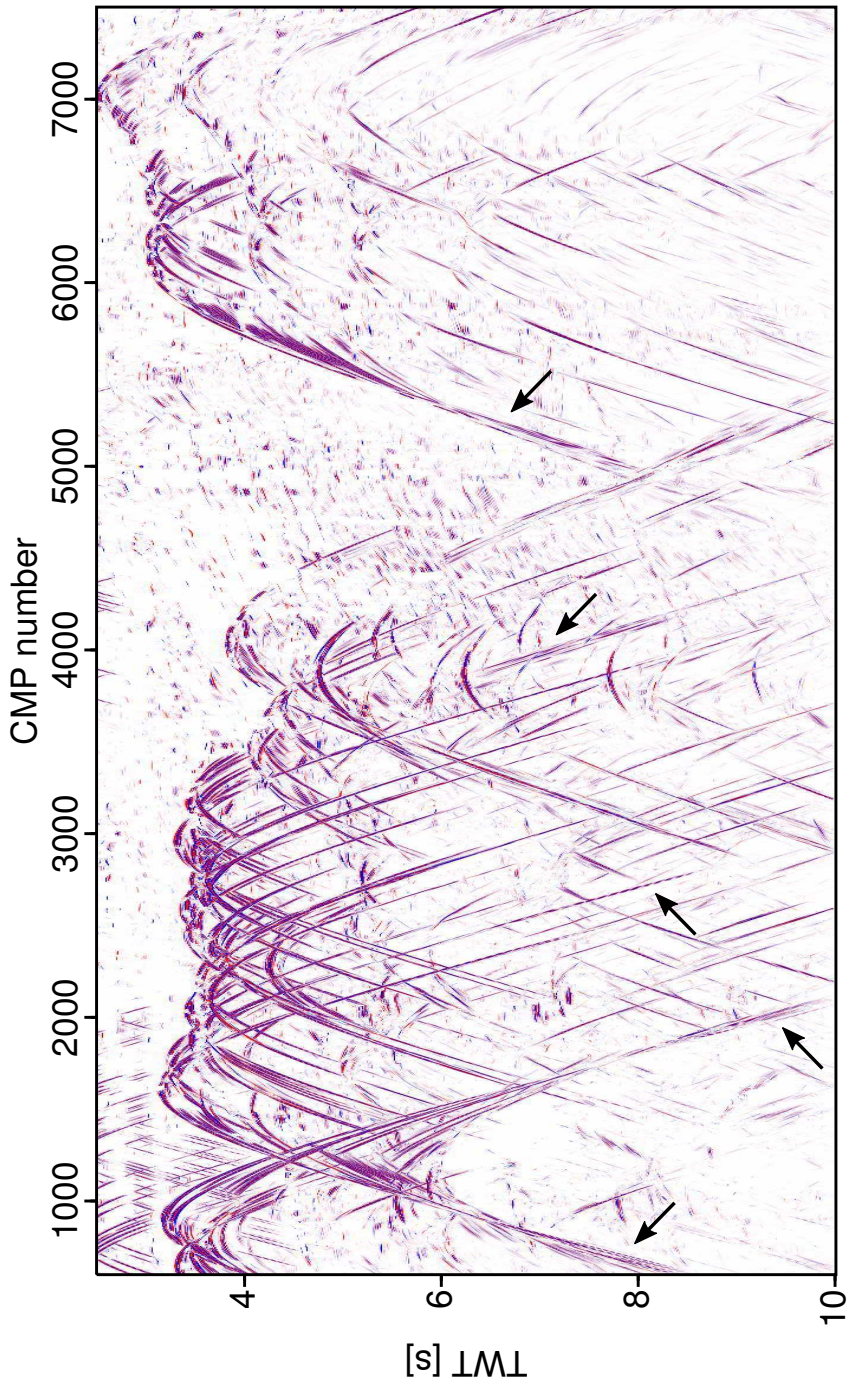

Figure 5.15: BP model: Prestack diffraction separation using the new weight.

Chapter 6

Summary and Outlook

In this thesis, I have presented a new workflow to enhance common-reflection-surface (CRS) based diffraction imaging. Since a key step to improve diffraction imaging is to enhance diffraction separation (from reflections), in the first and major stage, I have focused on diffraction separation method by Dell and Gajewski (2011). Accordingly, I have presented a new approach to separate diffractions in the full prestack data volume which is of great importance in diffraction imaging since it provides enhanced resolution, especially in sparsely illuminated regions. I have presented an extrapolation-based approach by modifying the kernel of the partial CRS stack technique (Baykulov and Gajewski, 2009) to establish a direct connection between zero-offset (ZO) to finite-offset (FO) diffraction processing. Since diffractions in the ZO domain are far easier to characterize and distinguish, the proposed workflow benefits from the the stability of zero-offset processing combined with the improved illumination of finite-offset processing to improve diffraction separation and subsequent imaging.

However, prestack diffraction processing is a challenge due to the fact that diffractions in the full prestack data volume are heavily masked by reflections and noise because of their weak amplitudes. To overcome this issue, the workflow takes advantage of the data enhancement facility of the partial CRS stack which comprises a prestack data summation within a small surface around each finite-offset sample, leading to a significant increase in the signal-to-noise ratio. In addition to data enhancement, the other two important features of the partial CRS stack including data interpolation and offset regularization can also be carried out simultaneously in one step. The final output of the proposed workflow is a prestack diffraction-only data volume.

The prestack diffraction-only data can be further stacked to obtain an improved ZO diffraction section. I used the 2D i-CRS diffraction operator for ZO to FO diffraction extrapolation and stacking in the prestack domain. The 2D i-CRS as a double-square-root (DSR) traveltime expression has been proven to be considerably more accurate than the hyperbolic CRS for very high curvatures. Therefore, the 2D i-CRS is most suitable to approximate diffraction traveltimes. Moreover, it allows a higher offset-to-target ratio.

However, to avoid the far-offset operator deviations, special care to choose a proper aperture size for stacking should be taken.

A comparison of the new ZO diffraction-only stacked section with the results of the existing poststack approach by Dell and Gajewski (2011) demonstrates superiority of the proposed prestack method. The diffraction separation potential of the poststack method turned out to decrease in presence of strong noise. In contrast, prestack diffraction separation, as it was shown in several data examples in this thesis, can considerably enhance diffraction separation.

A diffraction-only gather represents mostly diffracted events, which means that diffraction picks are predominant in the respective velocity spectrum. It implies that diffraction data is available for time migration velocity model building since stacking velocities after prestack diffraction separation are dip-independent. As a result, there is no need for further updates of stacking velocities to remove the effect of the dip. I also have observed that prestack diffraction separation leads to less noisy velocity spectra, higher coherency values, and better focused picks compared to the conventional stacking velocity spectra.

I have then incorporated diffraction imaging in the proposed workflow and implemented a diffraction-based fully automated migration velocity analysis (MVA) to build a time migration velocity model. As a general rule, if there is no sufficient number of diffractions in the data, the resulting velocity model will be poor. However, field data usually contain large amount of diffractions distributed along the seismic line.

Conflicting dip situations where different seismic events cross each other, are very challenging for any imaging techniques including the CRS-based diffraction imaging. In this case, the CRS stack may not provide the best fit to diffractions, leading to a poor diffraction separation. Conflicting dips are not handled in the proposed workflow to keep computational costs low. I did not refine the initial CRS attributes because of same reason. However, in order to exploit the full potential of the pre- and poststack diffraction separation methods, attribute refinement techniques as well as conflicting dips processing should be included in spite of the high computational costs (see Walda and Gajewski, 2015).

Diffraction separation in the time domain for media with moderate lateral velocity variations is robust with respect to the quality of the velocity model. In contrast, diffraction separation in the depth domain is most suitable for complex media. Although depth velocity model building using diffractions is not investigated in this thesis, but it can be implemented in the same manner (see, e.g., Bauer et al., 2015). In the case of diffraction-based depth imaging, the diffraction traveltimes are calculated by ray tracing or other advanced techniques instead of using an analytical diffraction operator. However, a very well determined velocity model is required. A new diffraction-based approach to build a depth velocity model is the application of the NIP-wave tomography (Duveneck, 2004) to the ZO diffraction-only data. In this scenario, the depth velocity model is consistent with data if the NIP-waves (or diffractions) are back-propagated to the depth points. For a detailed description of this recently introduced method, I refer to Schwarz (2015);

Bauer et al. (2015).

Another issue in 2D diffraction separation is problem of out-of-plane scatterers which makes the 3D diffraction processing inevitable. On the other hand, a diffraction is inherently a 3D phenomenon. To tackle these issued, I have extended the proposed workflow for prestack diffraction separation and imaging to 3D. An extended 3D diffraction threshold function by Dell and Gajewski (2011) was also used. Again, like in the 2D case, I took advantage of the partial CRS stack to extrapolate diffraction traveltimes from ZO to FO. As expected, data enhancement and regularization features of the partial 3D CRS demonstrated good potential for prestack diffraction enhancement. I used the classical 3D hyperbolic CRS operator since 3D DSR CRS-type operator was not available at the time of writing this thesis. The developed method exhibited a very fast and robust applicability to build a 3D time migration velocity model, which is a cumbersome task using conventional methods. Subsequently, the applying of diffraction-based time-imaging to a 3D simple as well as a complex synthetic data showed a promising outlook for further studies. As expected, prestack diffraction separation leads to improved diffraction-based migration velocity analysis in terms of better focused picked, higher coherence and less noise velocity spectra.

The proposed workflow for 3D diffraction imaging is purely based on the assumption of point diffractions. Therefore, separation of edge diffractions using 3D CRS attributes was not considered in the context of this thesis. On the other hand, conflicting dips are not resolved in 3D to speed up the process of prestack diffraction separation. However, if conflicting dips are handled and non-point diffractions are taken into consideration, the full potential of the workflow can be exploited.

In the second step, in the aim to further enhance diffraction separation, I have focused on the 2D diffraction weight function. I have reviewed the potential of the existing diffraction threshold function by Dell and Gajewski (2011) in order to improve its performance. The existing weight has been proven to be vulnerable to the presence of noise. Moreover, the separation potential decreases for higher times. To manage this issue, I have proposed to combine the existing weight by Dell and Gajewski with the width of the projected (first) Fresnel zone (PFZ). Although in theory a Fresnel zone is not defined (respectively infinite) for point diffractors, however in practice, diffractors have a spatial extent. In consequence, the width of the projected Fresnel zone for a diffraction is much larger that the one for a reflection, the difference can thus be used as a consistent attribute to better identify diffractions in the data and enhance the separation. Application of the new weight to a gradient synthetic as well as a complex data sets demonstrated better pre- and poststack diffraction separation.

Seismic diffractions have a significant potential for seismic imaging. In this thesis only the kinematic features were considered. A shift to the dynamic features (e.g., amplitude and phase) will open the way for diffraction imaging in correct amplitudes and quantitative analysis of the results.

Used software

During the research work, different types of operating systems have been used, which are Linux (Debian and CentOS) free version licenses.

The diffraction separation method is based on the 2D ZO CRS stack code by Jürgen Mann (2002) and its 3D extension is based on the 3D ZO CRS stack code written by Alex Müller (2007) and modified by Parsa Bakhtiari Rad.

For synthetic data generation, Seismic Un*x (Colorado School of Mine) and Norsar 3D (NORSAR Innovation AS) were used.

For visualization, Seismic Un*x (Colorado School of Mine) and Matlab were used.

Four types of hardware machines have been used:

1. Desktop machine core i5 based.
2. Thunder (little endian) cluster 32cores based.
3. Laptop core i5 based.

The thesis is written on laptop and desktop based OS in LATEX.

Acknowledgments

- I am grateful to Professor Dr. Dirk Gajewski for accepting me as PhD student, supervision of this work and for giving me a lot of freedom in choosing my research topics. He gave me the opportunity to participate in many geophysical conferences around the globe.
- I am also grateful to PD Dr. Claudia Vanelle for the co-supervision of my thesis. Special thank for the proofreading of this thesis and many other works.
- I like to thank Dr. Ali Dehghani for always being helpful.
- I like to say thank you to Dr. Ekkehart Tessmer for managing of my computer requirements.
- I am as well grateful to Dr. Sergius Dell, Dr. Mikhail Baykulov and Dr. Benjamin Schwarz for interesting discussions, good advice and support.
- Very special thanks to Jan Walda, Marie Voss, Martina Bobsin and Manizheh Vefagh for proofreading, corrections and many suggestions to this thesis.
- I gratefully acknowledge the Wave Inversion Technology (WIT) consortium for providing the required codes/softwares for the work presented in this thesis.
- I like to thank TGS for providing the Eastern Mediterranean data set. Also the Sandia National Library (SNL) for SEG/EAGE salt model and, SMAART JV for Sigsbee-2A synthetic data sets.
- Obviously, I like to thank my family for supporting me throughout my Ph.D. and always having an open ear for me. I like to thank my dear lovely wife, SHADAN. You always encouraged me to push myself a bit further and could get myself out of black holes every time I was desperate by just smiling at me.

Bibliography

Ahmed, K. A., Schwarz, B., and Gajewski, D. (2015). Application of the 3D common-reflection-surface stack workflow in a crystalline rock environment. *Geophysical Prospecting*, 63:990–998.

Al-Chalabi, M. (1973). Series approximation in velocity and traveltime computations. *Geophysical Prospecting*, 21:783–795.

Bakhtiari Rad, P. and Gajewski, D. (2015). 3D CRS-based prestack diffraction separation and enhancement. *77th EAGE annual meeting, Extended Abstracts*.

Bakhtiari Rad, P., Gajewski, D., and Vanelle, C. (2015a). 3D time migration velocity model building using CRS-based pre-stack diffraction separation. *85th SEG annual meeting, Expanded Abstracts*, pages 4091–4095.

Bakhtiari Rad, P., Gajewski, D., and Vanelle, C. (2016). Diffraction separation based on the projected first Fresnel zone. *78th EAGE annual meeting, Extended Abstracts*.

Bakhtiari Rad, P., Schwarz, B., Vanelle, C., and Gajewski, D. (2014). Common reflection surface (CRS) based pre-stack diffraction separation. *84th SEG annual meeting, Expanded Abstracts*, pages 4208–4212.

Bakhtiari Rad, P., Vanelle, C., and Gajewski, D. (2015b). 3D CRS-based prestack diffraction separation and imaging. *77th EAGE annual meeting, Extended Abstracts*.

Bauer, A., Schwarz, B., and Gajewski, D. (2015). Prestack diffraction enhancement using a traveltime decomposition approach. *85th SEG annual meeting, Expanded Abstracts*.

Baykulov, M. and Gajewski, D. (2009). Prestack seismic data enhancement with partial common-reflection-surface (CRS) stack. *Geophysics*, 74(3):V49–V58.

Bergler, S. (2004). *On the determination and use of kinematic wavefield attributes for 3D seismic imaging*. PhD thesis, University of Karlsruhe.

Berkovitch, A., Belfer, I., Hassin, Y., and Landa, E. (2009). Diffraction imaging by multifocusing. *Geophysics*, 74(6):WCA75–WCA81.

Berryhill, A. W. (1977). Diffraction response for nonzero separation of source and receiver. *Geophysics*, 42:1158–1176.

Billette, F. and Brandsberg-Dahl, S. (2005). The 2004 BP Velocity Benchmark. *67th EAGE annual meeting, Extended Abstracts*.

Biondi, B. (2004). *3-D Seismic Imaging (Investigations in Geophysics No. 14)*. Soc. Expl. Geophys.

Bobsin, M. (2014). *Time migration applying i-CRS operator*. Master thesis, University of Hamburg.

Bortfeld, R. (1989). Geometrical ray theory: Rays and traveltimes in seismic systems (second-order approximation of the traveltimes). *Geophysics*, 54:342–340.

Ĉervený, V. (1987). Ray methods for three-dimensional seismic modelling. *Petroleum Industry Course, Norwegian Institute for Technology*.

Ĉervený, V. (2001). *Seismic Ray Theory*. Cambridge University Press.

Claerbout, J. F. (1985). *Imaging the Earth's Interior*. Blackwell.

Dell, S. (2012). *Seismic processing and imaging with diffractions*. PhD thesis, University of Hamburg.

Dell, S. and Gajewski, D. (2011). Common-reflection-surface-based workflow for diffraction imaging. *Geophysics*, 76(5):S187–S195.

Deregowski, S. and Rocca, F. (1981). Geometrical optics and wave theory of constant offset sections in layered media. *Geophysical Prospecting*, 29:374–406.

Dümmong, S. (2010). *Seismic data processing with an expanded Common Reflection Surface workflow*. PhD thesis, University of Hamburg.

Duveneck, E. (2004). *Tomographic determination of seismic velocity models with kinematic wavefield attributes*. PhD thesis, University of Karlsruhe.

Fomel, S., Landa, E., and Taner, M. T. (2007). Poststack velocity analysis by separation and imaging of seismic diffractions. *Geophysics*, 72(6):U89–U94.

Geiger, H. D. (2001). *Relative-amplitude-preserving prestack time migration by the equivalent offset method*. PhD thesis, University of Calgary.

Gelchinsky, B., Berkovitch, A., and Keydar, S. (1999). Multifocusing homemorphic imaging part 1. basic concept and formulas. *J. Appl. Geoph*, 42:229–242.

Grasmueck, M., Coll, M., Eberli, G. P., and Pomar, K. (2013). Diffraction imaging of sub-vertical fractures and karst with full-resolution 3D ground-penerating radar. *Geophysical Prospecting*, 61:907–918.

Guntern, C. (2013). *Bearbeitung reflexionsseismischer Daten unter besonderer Berücksichtigung von Diffraktionen*. Bachelorarbeit, Universität Hamburg.

Harlan, W. S., Claerbout, J. F., and Rocca, F. (1984). Signal/noise separation and velocity estimation. *Geophysics*, 49:1869–1880.

Hertweck, T., Jäger, C., Goertz, A., and Schleicher, J. (2003). Aperture effects in 2.5-D Kirchhoff migration: A geometrical explanation. *Geophysics*, 68(5):1673–1684.

Hubral, P. (1975). Locating a diffractor below plane layers of constant interval velocity and varying dip. *Geophysical Prospecting*, 23:313–322.

Hubral, P. (1983). Computing true amplitude reflections in a laterally inhomogeneous earth. *Geophysics*, 48:1051–1062.

Hubral, P. and Krey, T. (1980). *Interval velocities from seismic reflection traveltime measurements*. Soc. Expl. Geophys.

Hubral, P., Schleicher, J., and Tygel, M. (1992). Three-dimensional paraxial ray properties -I. Basic relations. *Journal of Seismic Exploration*, 1:265–279.

Hubral, P., Schleicher, J., Tygel, M., and Hanitzsch, C. (1993). Determination of Fresnel zones from traveltime measurements. *Geophysics*, 58(5):703–712.

Jäger, R. (2004). *Minimum aperture Kirchhoff migration with CRS stack attributes*. PhD thesis, University of Karlsruhe.

Jäger, R., Mann, J., Höcht, G., and Hubral, P. (2001). Common-reflection-surface stack: Image and attributes. *Geophysics*, 66:97–109.

Kanasewich, E. R. and Phadke, S. M. (1988). Imaging discontinuities on seismic sections. *Geophysics*, 53:334–345.

Keller, J. B. (1962). Geometrical theory of diffraction. *Journal of the Optical Society of America*, 52:116–130.

Khaidukov, V., Landa, E., and Moser, T. J. (2004). Diffraction imaging by focusing-defocusing: An outlook on seismic superresolution. *Geophysics*, 69:1478–1490.

Klem-Musatov, K. (1995). *Theory of edge waves and their use in seismology*. SEG.

Klem-Musatov, K., Aizenberg, A., Pajchel, J., and Helle, H. (2008). *Edge and tip diffractions: Theory and applications in seismic prospecting*. Number 14. SEG Geophysical Monograph Series.

Klokov, A., Baina, R., and Landa, E. (2011). Point and edge diffraction in three dimensions. *73rd EAGE annual meeting, Extended Abstracts*.

Klokov, A. and Fomel, S. (2012). Separation and imaging of seismic diffractions using migrated dip-angle gathers. *Geophysics*, 77(6):S131–S143.

Kozlov, E., Barasky, N., Koroloev, E., Antonenko, A., and Koshchuk, E. (2004). Imaging scattering objects masked by specular reflections. *74th SEG annual meeting, Expanded Abstracts*, pages 1131–1135.

Krey, T. (1952). The significance of diffraction in the investigation of faults. *Geophysics*, 17:843–858.

Landa, E. (2013). Role of wave field diffraction component in seismic imaging. *Seismic Technology*, 10(1):1–48.

Landa, E., Fomel, S., and Reshef, M. (2008). Separation, imaging and velocity analysis of seismic diffraction using migrated dip-angle gathers. *78th SEG annual meeting, Expanded Abstracts*, pages 2176–2180.

Landa, E., Shtivelman, V., and Gelchinsky, B. (1987). A method for detection of diffracted waves on common-offset sections. *Geophysical Prospecting*, 35:359–373.

Mann, J. (2002). *Extensions and applications of the common-reflection-surface stack method*. PhD thesis, University of Karlsruhe.

Mayne, W. H. (1962). Common reflection point horizontal data stacking techniques. *Geophysics*, 27:927–938.

Moser, T. J. (2011). Edge and tip diffractions imaging in three dimensions. *73rd EAGE annual meeting, Extended Abstracts*.

Moser, T. J. and Howard, C. B. (2008). Diffraction imaging in depth. *Geophysical Prospecting*, 56:627–641.

Müller, N.-A. (2003). *The 3D Common-Reflection-Surface stack - theory and application*. Diplomarbeit, Universität Karlsruhe.

Müller, N.-A. (2009). Treatment of conflicting dips in the 3D common-reflection-surface stack. *Geophysical Prospecting*, 57(6):981–995.

Müller, T. (1999). *The Common Reflection Surface Stack Method: Seismic Imaging without Knowledge of the Velocity Model*. PhD thesis, University of Karlsruhe.

Müller, T., Jäger, R., and Höcht, G. (1998). Common reflection surface stacking method-imaging with an unknown velocity model. *68th SEG annual meeting, Expanded Abstracts*, pages 1764–1767.

Necati, G., Magesan, M., and Connor, J. (2005). Diffracted noise attenuation in shallow water 3D marine surveys. *75th SEG annual meeting, Expanded Abstracts*.

Nelder, J. A. and Mead, R. (1965). A simplex method for function minimization. *Computer Journal*, 7:308–313.

Netzeband, G., Gohl, K., Hübscher, C., Ben-Avraham, Z., Dehghani, A., Gajewski, D., and Liersch, P. (2006). The Levantine Basin - crustal structure and origin Messinian evaporites in the Levantine Basin. *Tectonophysics*, 418:178–188.

Press, W., Teukolsky, S., Vetterling, W., and Flannery, B. (2002). *Numerical Recipes in C++, Second Edition*. Cambridge University Press.

Reshef, M. and Landa, E. (2009). Post-stack velocity analysis in the dip-angle domain using diffractions. *Geophysical Prospecting*, 57:811–821.

Robein, E. (2003). *Velocities, Time imaging, Depth imaging in Reflection seismics: Principles and Methods*. EAGE Publication, Houten.

Sava, P. C., Biondi, B., and Etgen, J. (2005). Wave-equation migration velocity by focusing diffractions and reflections. *Geophysics*, 70(3):U19–U27.

Schleicher, J., Hubral, P., Tygel, M., and Jaya, M. S. (1997). Minimum apertures and Fresnel zones in migration and demigration. *Geophysics*, 62(1):183–194.

Schleicher, J., Tygel, M., and Hubral, P. (1993). Parabolic and hyperbolic paraxial two-point traveltimes in 3D media. *Geophysical Prospecting*, 41:495–513.

Schwarz, B. (2015). *Moveout and geometry*. PhD thesis, University of Hamburg.

Schwarz, B., Vanelle, C., Kashtan, B., and Gajewski, D. (2012). i-CRS: Application of a new multi-parameter stacking approach to complex media. *SEG annual meeting, Expanded Abstracts*, pages 1–5.

Shah, P. M. (1973). Use of wavefront curvature to relate seismic data with subsurface parameters. *Geophysics*, 38(5):812–825.

Soleimani, M., Piruz, I., Mann, J., and Hubral, P. (2009). Solving the problem of conflicting dips in common reflection surface (CRS) stack. *1st International Petroleum Conference and Exhibition*, EAGE, Extended Abstracts.

Söllner, W. and Yang, W. (2002). Diffraction response simulation: A 3D velocity inversion tool. *72nd SEG annual meeting, Expanded Abstracts*, pages 2293–2296.

Spinner, M. (2007). *CRS-based minimum-aperture Kirchhoff migration in the time domain*. PhD thesis, University of Karlsruhe.

Sturzu, I., Popovici, A., Pelissier, M., Wolak, J., and Moser, T. J. (2014). Diffraction imaging of the Eagle Ford shale. *First Break*, 32:49–59.

Sun, J. (1994). Geometrical ray theory: Edge-diffracted rays and their traveltimes (second order approximation of the traveltimes). *Geophysics*, 59(1):148–155.

Taner, M. and Koehler, F. (1969). Velocity-spectra digital computer derivation and applications of velocity functions. *Geophysics*, 34:859–881.

Tygel, M., Müller, T., Hubral, P., and Schleicher, J. (1997). Eigenwave based multiparameter traveltime expansions. *67th SEG annual meeting, Expanded Abstracts*, pages 1770–1773.

Ursin, B. (1982). Quadratic wavefront and traveltime approximations in inhomogeneous layered media with curved interfaces. *Geophysics*, 47:1012–1021.

Vanelle, C. and Gajewski, D. (2002). Second-order interpolation of traveltimes. *Geophysical Prospecting*, 50:73–83.

Vanelle, C., Kashtan, B., Dell, S., and Gajewski, D. (2010). A new stacking operator for curved subsurface structures. *72nd SEG annual meeting, Expanded Abstracts*, pages 3609–3613.

Voss, M. (2013). *Bearbeitung reflexionsseismischer Daten unter besonderer Berücksichtigung von Diffraktionen.* Bachelorarbeit, Universität Hamburg.

Walda, J. and Gajewski, D. (2015). Common-reflection-surface stack improvement by differential evolution and conflicting dip processing. *85th SEG annual meeting, Expanded Abstracts*, pages 3842–3847.

Wissmath., S. (2016). *Finite-Offset CRS: Attribute Prediction and Application.* Master thesis, University of Hamburg.

Yilmaz, O. (2001). *Seismic Data Processing, Vol. I and II.* SEG, Tulsa.

Zhang, Y., Bergler, S., and Hubral, P. (2008). Common-reflection-surface (CRS) stack for common offset. *Geophysical Prospecting*, 49(6):709–718.

Erklärung

Eidesstattliche Versicherung
Declaration on oath,

Hiermit erkläre ich an eides statt, dass ich die vorliegende Dissertationsschrift selbst verfasst und keine anderen als die angegebenen Quellen und Hilfsmittel benutzt habe.
I hereby declare, on oath, that I have written the present dissertation by my own and have not used other than the acknowledged resources and aids.

Hamburg, den 4.Juli.2016

Parsa Bakhtiari Rad